

Ph.D. thesis in Fluid Mechanics and Applied Mathematics – XXI ciclo

Two Approaches to the Study of Detached Flows



Gabriele Ottino

Tutor

prof. Luca Zannetti
Politecnico di Torino

Cotutela

prof. Angelo Iollo
Université de Bordeaux 1 - INRIA

Summary

In the present work flow separation phenomena are investigated by means of two different approaches.

In the first part, 2D unsteady incompressible inviscid flows are studied. An analytical-numerical model, based on the conjunction of a conformal mapping and a point vortex method, is built to define the potential flow field in a doubly connected domain where bodies are characterized by a variation in time of their circulation. In particular, the study of the unsteady flow past a 2-blade Darrieus VAWT is addressed. Until now the study of vortex motions has only been described in doubly-connected flow fields where the circulations have a constant null value. The flow field here analysed has a deep unsteadiness, which determines the circulations varying in time: a technique is therefore developed to uniquely define the circulations around the bodies. Three conditions then need to be imposed: in addition to the two Kutta conditions at the trailing edges, another one has to be imposed in order to satisfy the Kelvin theorem. With a classical configuration, this machine, experiencing angles of attack of opposite values, gives rise to complex vortex shedding phenomena that reduce its performances and stress its structure. In order to control the flow separation from the blades, an innovative solution is qualitatively investigated which consists of taking blade profiles provided with vortex trapping cavities. Interesting results are obtained, even if in the limit of inviscid flow.

In the second part compressible viscous flows are taken into account. A fully Navier-Stokes equations solver is implemented introducing the penalization technique. The idea is to replace the bodies by fluid, such that the penalized Navier-Stokes equations remain valid in the bodies, while respecting the boundary conditions on their contours. Starting from this purpose, the bodies are considered as porous media with a little porosity with respect to that of the external flow, which tends to infinity. This technique allows simple Cartesian meshes to be used, even for very complex geometries like those of industrial interest. The resulting code is tested on different flow fields, both steady and unsteady, both subsonic and supersonic, obtaining always a good agreement with other theoretical and numerical results described in literature.

Acknowledgments

I would like to thank the 'Université Franco-Italienne' for the grant supporting my Ph.D. work in 'co-tutelle' between the Politecnico di Torino (Italy) and the Institut de Mathématiques de Bordeaux - Université de Bordeaux 1 (France).

Table of contents

Acknowledgments	ii
1 Introduction	1
1.1 I part	3
1.2 II part	10
I Unsteady incompressible and inviscid flow model	15
2 Study of a VAWT	16
2.1 Flow field simulation: modeling tools	20
2.1.1 Classical approaches	20
2.1.2 The analytical-numerical approach	22
3 Model-building	28
3.1 Conformal mapping	28
3.1.1 From μ -plane to ν -plane	28
3.1.2 From ν -plane to z -plane	29
3.2 Definition of the complex potential	32
3.2.1 Turbine at rest	32
3.2.2 The motion of the blades	36
3.2.3 Kutta condition	38
3.2.4 The meaning of the constant \mathbf{K}	40
3.2.5 Instantaneous absolute and relative flow fields	43
3.3 Evolution in time of the flow field	44

3.4	Numerical example	48
4	A suggestion for a better design of a VAWT	51
4.1	Conformal Mapping	53
4.2	The complex potential and its evolution in time	55
4.3	Numerical example	56
II	Setting-up of a penalized fully Navier-Stokes equations solver	59
5	Fully Navier-Stokes equations solver	60
5.1	Governing equations	63
5.2	Discretization technique	64
5.2.1	Convective fluxes	65
5.2.2	Diffusive fluxes	67
5.2.3	Boundary conditions	69
5.2.4	Time integration schemes	70
5.3	Validation	73
6	The Penalization Method	79
6.1	Time integration schemes	80
6.1.1	Semi-implicit model	80
6.1.2	Fully implicit model	81
6.2	Validation	82
6.2.1	Unsteady subsonic case: flow past a confined square cylinder	82
6.2.2	Steady supersonic case: bow shock	86
6.2.3	Unsteady supersonic flow: transmission and reflection of a shock	91
6.3	Application to moving boundaries	93
7	Conclusions	96
	Bibliography	99

List of figures

2.1	Savonius turbine scheme.	18
2.2	Examples of Darrieus turbines: the curve-blade-type (a) and the straight-blade-type (b).	18
2.3	General working cycle of a Darrieus turbine: the lift L always generates a positive torque.	19
2.4	Situation analysed during a working cycle: W is the wind speed, V_T the tangential velocity due to the rotation around the vertical shaft, V_R the effective velocity experienced by the blades.	21
3.1	Annular region in the μ -plane.	29
3.2	Apollonius circles with foci in $\pm\eta_0$	29
3.3	Symmetrical circles with respect to the real axis; ν -plane.	30
3.4	Physical z -plane: two-blade Darrieus turbine with angular velocity Ω experiencing the wind speed q_∞	30
3.5	Computational domain in the transformed χ -plane.	33
3.6	Streamline flow field inside the fundamental area (a) and inside a larger area (b) in the χ -plane: effect of second order poles.	34
3.7	Streamline flow field inside the fundamental area (a) and inside a larger area (b) in the χ -plane: effect of first order singularities.	35
3.8	Imposition of the impermeability condition.	37
3.9	Kutta condition: computation of the relative velocity on the blade contours.	39
3.10	Streamline distribution of the absolute (a) and relative(b) flow fields around the upper blade.	43

3.11	Streamline distribution of the absolute (a) and relative(b) flow fields around the lower blade.	43
3.12	Wake visualisation past the two-blade Darrieus turbine at time instant $t = 28.5$; in the flow field 12400 vortex singularities are present.	49
3.13	Time history of the bound circulations around the upper (blue) and lower (black) blades.	49
4.1	Advantage illustration of the vortex trapping cavity solution.	52
4.2	Mapping sequence: from μ -plane to the physical z -plane.	54
4.3	Generation of the trapped vortex structures: visualization of the streamline flow field behavior up to $t=0.4$	56
4.4	Development in time of the flow field past a two-blade turbine with vortex trapping cavities; snapshots at: ($t = 0.4, N = 1186$) (a), ($t = 1.818, N = 5392$) (b), ($t = 3.37, N = 9904$) (c), ($t = 4.89, N = 14311$) (d), ($t = 6.14, N = 17914$) (e), ($t = 7.71, N = 22424$) (f)	58
5.1	Riemann problem at the interface between the n -th and $(n + 1)$ -th cells	66
5.2	Determination of the slope for the linear distribution of the conservative variables into the n -th cell	66
5.3	Gradient computation on the displaced cells	68
5.4	Gradient computation on the wall cells; a half-volume cell is considered.	69
5.5	Stencil for the computation of the Jacobian matrix terms.	73
5.6	Euler test case: reflecting shock	74
5.7	Mach number flow field: in (a) the first order scheme results, in (b) those of the second order scheme; three streamlines are shown for each snapshot.	75
5.8	Rate of convergence for the first and second order schemes	76
5.9	The temperature (a) and velocity (b) self-similar profiles.	77
5.10	Numerical solutions for T and u over the G_3 grid.	77
5.11	Temperature (a) and velocity (b) rate of convergence to the solution obtained by means of the G_4 grid.	78
6.1	Computational domain: confined square cylinder; low Reynolds number unsteady subsonic flow; Poiseuille velocity profile at the inlet	82

6.2	Horizontal (a) and vertical (b) velocity flow fields: the coherent structures into the von Kármán wake are visible.	84
6.3	Pressure (a) and temperature (b) flow fields.	84
6.4	Velocity module (a) and temperature (b) profile along the vertical line at $x = 0$	85
6.5	Strouhal-Reynolds number for $L/H = 0.125$	85
6.6	Comparison with the results of the code <i>AERO</i> : in (a) convergence on the order of the method; in (b) comparison with the oscillation amplitude of the flow field over the G_2 grid.	86
6.7	Horizontal velocity (a), temperature (b), pressure (c) and density (d) fields around a cylinder moving at $M = 2$	87
6.8	Mach number field (a) and isocontours (b) for a cylinder moving at $M = 2$	88
6.9	Horizontal velocity (a) and temperature (b) distribution along the line at $y = 1$	89
6.10	Pressure (a) and Mach number (b) distribution along the line at $y = 1$	90
6.11	Streamlines in the recirculation region past the cylinder.	90
6.12	Horizontal (a) and vertical (b) velocities, temperature (c) and Mach number (d) fields at $t = 0.4$	92
6.13	Velocity module distribution along the lines $y = 1$ (a) and $x = 0.5$ (b).	92
6.14	Domain geometrical features.	93
6.15	Snapshots for Mach (left and central columns) and pressure (right column) fields at different time instants: at $t = 0.352$ (a),(b),(c), at $t = 0.682$ (d),(e),(f), at $t = 1.03$ (g),(h),(i), at $t = 1.239$ (j),(k),(l), at $t = 1.81$ (m),(n),(o).	95

List of tables

6.1 Numerical comparison between the present results and those of [5] and [6] . 90

Chapter 1

Introduction

The study of flow separation from the surface of a solid body and the determination of different changes in the flow field that develop as a result of the separation are the main subjects investigated in the present work. The problem of boundary-layer separation has attracted considerable attention over several decades, because of both fundamental flow physics and technological applications (Prandtl [54]; Lachmann [34]; Chang [8]). Flow separation occurs on airfoils, behind blunt bases, in high-speed intakes and in a variety of other engineering systems, including turbomachinery and automobiles. Some of the essential ideas related to boundary-layer separation, and the need to prevent it from occurring, have been addressed by Prandtl [54]. Flow separation generally leads to increased energy losses, instability, and so on, and control of the same is desirable to improve the aerodynamic performances.

As shown in Prandtl [54], everywhere in the boundary layer the dimensionless velocity component v normal to the body surface is of order $Re^{-1/2}$, so in the limit as $Re \rightarrow \infty$ the boundary layer becomes a surface of tangential discontinuity which coincides with the body surface. Such flows are unseparated. They can be realized, for example, near a plate placed parallel to the flow direction or at the surface of a thin airfoil at a small angle of attack. In general, for the realization of unseparated flow, rather severe restrictions are required, which in the majority of cases are not fulfilled in practice; this leads to the formation of flow of another kind, with its separation from the surface.

The physical nature of the flow separation phenomena was first described by Prandtl

[54] on the basis of his boundary layer theory. The appearance of flow separation is always due to the action of an adverse pressure gradient. Under this influence, fluid elements moving inside the boundary layer and having a smaller amount of kinetic energy than elements at its outer edge are more strongly decelerated. The velocity profile in the boundary layer is gradually changed, so that at some cross section $x = x_s$ the dimensionless skin friction $\tau = (\partial u / \partial y)_{y=0}$ becomes zero for the first time, and for $x > x_s$ there appears a region of slow reverse flow. This region expands rapidly, moving fluid elements from the boundary layer to finite distances from the body surface. This leads to detachment and to roll-up processes.

The separated shear layer develops then under zero pressure gradient conditions initially and the velocity along the dividing streamline increases. The shear layer entrains fluid both from the reversed flow zone as well as from the outer inviscid flow (external to the shear layer); this is followed by the reattachment of the shear layer onto a downstream wall (when the phenomena occur along the surface of the body) or by the recompression associated with the confluence of top and bottom shear layers (when the phenomena occur at the trailing edge of the body). The region where reattachment/recompression take place depends primarily on the shear layer characteristics and the boundary conditions the flow encounters there, and it is characterized by an increase of pressure. The mass entrained by the shear layer from the reversed flow is returned at reattachment which forms a recirculating bubble; this new arisen structure brings about significant adverse aerodynamic effects, especially the increase of the pressure drag. The pressure field in a separated flow is significantly influenced by the shear layer reattachment process and therefore it is a key element in the dynamics of separated flows (see Roshko [59]). In extreme circumstances where the flow is not able to reattach to the rear part of the body surface, and a large separation area occurs, there will be a sudden loss of lift and a strong increase of drag.

In the present work flow separation is analysed and investigated from two different points of view that will be introduced in the following sections. The purpose is to describe separated flows by means of two different tools: in the first part the attention is focused on the unsteady separation of incompressible inviscid flows; an analytical-numerical model, based on the conjugation of the conformal mapping theory and a classical numerical vortex method, is built in order to describe the arising vortex shedding phenomena; as reference

case, the impulsively started flow past a two blade Darrieus turbine is analysed. It presents two sources of unsteadiness due both to the internal structures of the flow and to the motion of the bodies. In this framework an innovative solution is proposed to control flow separation in order to avoid the negative effects of the vortex shedding phenomena on the performances and on the structure of the machine: derived from the VortexCell2050 European project [75], the vortex trapping technology is applied to the design of the blade profiles. In the second part of this work, we focus on the developing of a numerical grid-based technique able to describe separation of all kind of flows, from the steady subsonic to the unsteady supersonic ones. The penalization idea is applied to build a fully Navier-Stokes solver code: in addition to coding a semi-implicit scheme able to reproduce the results present in literature about the treatment of supersonic steady and unsteady flows, the applicability of the same is verified also to the subsonic unsteady ones; in order to speed-up the computational time, a fully implicit scheme is then developed and tested on the same reference cases, resulting in the advantage of taking greater CFL numbers.

1.1 I part

In the first part of the work the dynamics of separation phenomena of 2D unsteady incompressible flow field is addressed in domains confined by multiple bodies developing an analytical-numerical model. This kind of problem is investigated in some applications of practical interest, such as, among many others, the aerodynamics of multiple airfoils, the unsteady motion past multi-bladed vertical axis wind turbines and the sea motion past islands. Here we focus in particular on the impulsively started flow field past a two-bladed Darrieus turbine, which consists of a couple of curved or straight blades rotating around a vertical shaft. It can be considered as a physically coherent example characterized by interesting features: separation phenomena are relevant, the blades experiencing large oscillations of the incidence during each cycle and the fluid motion being heavy unsteady; the unsteadiness which will be dealt with is generated both by the structures arising into the flow field because of the detachment and by the motion of the bodies. The study is performed in the plane normal to the shaft, assuming the flow field to be 2D, and that the blades are rotating with the angular velocity Ω , with the uniform flow q_∞ as undisturbed boundary condition.

Neglecting the diffusion effects, the flow is assumed to be inviscid and governed by the Euler equations. In studies like these, a classical approach is represented by the panel method (see, for instance, Kuethe & Chow [33]): the flow around the body is modelled as the summation of a uniform flow and a series of vortex panels arranged to form a closed polygon with a shape that approximates, as nearly as possible, the actual curved shape of the body itself; that is, the geometry is solved with a set of potential singularities directly on the body profile in the physical plane. In the present work, according to Deglaire [13], another technique is implemented, which is based on the conjugation of two methods:

- *conformal mapping*: this analytical tool is a transformation from the complex plane into the complex plane, which preserves the local angles; it involves the study of complex variable analytical functions (see Tricomi [71]). The idea behind this technique is to relate the flow field around one shape which is already known (in the so called *computational plane*) to the flow field around the real body geometry (in the *physical plane*). Most often a circle is used as the first shape: in the case of single-element airfoils, Riemann's mapping theorem insures that any body can be mapped onto a unit circle. So the problem is to find an analytic function that relates every point on the circle to a corresponding point on the physical body geometry. Starting from the well known Joukowsky mapping, which transforms a circle into an airfoil with a cusped trailing edge, a lot of different mappings have been developed in order to obtain more and more complex shapes, the most common being the Kármán-Trefftz one, which enables to obtain airfoils with a finite trailing edge, and the Theodorsen-Garrick one (see Theodorsen & Garrick [69]), which uses an iterative method to pass from the quasi-circle obtained from the real geometry to the exact circle, allowing to apply the conformal mapping to a wide range of airfoil shapes.

Here multi-connected domains are dealt with; in literature mapping chains can be found which maps this kind of domains onto simpler computational domains bounded by circles. For example, Ives [28] describes a mapping which maps the first airfoil into an exact circle, then applies an analogous transformation to the second airfoil while keeping the image of the first one a circle, and so on with the other bodies; Halsey [24] defines a transformation which carries out the map on all the bodies at

the same time. Both of them can be applied to body of almost any shape; they make use of the single-element conformal mappings previously described, but they introduce iterative procedures which make the transformation more heavy in term of computational time.

The purpose here being to use a technique which enables the description of the vortex-shedding phenomena from bodies of general shape, there is no need to consider a specific real geometry. This is why the followed procedure is opposite to the usual one: starting from the simpler computational domain, an analytical function will be built which enables to obtain profiles with as symmetrical as possible geometries into the physical plane, resulting in speeding up the computational time. Once this function has been defined, the procedure is the well known one: the flow field is solved in the simpler domain, and then, by means of the inverse of the analytical function, its image in the physical plane is computed.

- *point vortex method*: this numerical tool is used to solve the flow field in the computational domain. Vortex methods are numerical approaches with two fundamental features: first, the Euler equations are formulated in terms of vorticity, and so the spatial discretization is carried out over the vorticity field instead of the velocity one; second, making use of the Helmholtz's theorem (see Lighthill [38]) which states the correspondence between the vorticity elements and the material fluid elements, the computational vortex elements are Lagrangian and so convect with the fluid velocity. Describing the flow in terms of vorticity is desirable due to the intuitive power of visualizing the vorticity field, especially in complex and unsteady flows. One of the major advantages, as illustrated in a lot of works in literature, is that the vorticity field is compact, so smaller sized domains can be used in comparison with classical grid-based approaches, and also boundary conditions at infinity can be automatically satisfied. On the contrary, satisfying the free-space boundary condition of external flows can be a delicate matter in grid-based methods with truncated flow domains. Furthermore, the Lagrangian vortex particles convect without numerical dissipation, which is, again, in contrast with grid-based schemes which inevitably suffer from this kind of problem. Finally, the essentially grid-free nature of a vortex method is itself an advantage, as grid-generation is often one of the most expensive

processes in computational fluid dynamics, especially when the bodies in the domain are moving.

The pioneering work on vortex methods was done by Rosenhead [58] to describe the evolution of vortex sheets. But the modern vortex methods were born in the 1970s; in later decades, the development of the method was very rich, mainly in relation to the treatment of boundary conditions for solid surfaces and the efficient reduction of the computational costs, so as to make them suitable for the high-resolution simulation of unsteady, high-Reynolds number flows. Comprehensive reviews of the development of vortex methods and their applications can be found in Leonard [36] and Sarpkaya [64].

In the present work the discrete approximation used for the continuous evolution of smooth trailing-edge vortex sheets is that described in the literature in several publications, such as Clements [11], Sarpkaya [63], Kiya & Arie [32], Zannetti & Iollo [81], and references therein. The wake issued by the sharp edges of the bodies is simulated by adding point vortices which satisfy the Kutta condition at prescribed time intervals. The vorticity being concentrated on singular vortex particles, the rotational flow is reduced to a potential flow affected by vortex singularities. This leads to the possibility of describing the flow field by means of the complex potential theory, where the point vortices have a logarithmic development. What has to be noted is that the vortex method here implemented is not the best we can find in literature, but it is a method which enables a good description of the dynamics of the flow field. If we focus on the efficiency of the adopted method, its computational cost is $O(N^2)$, where N is the number of vortex particles in the flow field; methods can be found which are more efficient, with a computational cost which is $O(N\log(N))$ (see, for example, Ferlauto [14] and references therein).

The complex velocity and potential are built in two different steps: firstly, the flow past the turbine at rest is described in a computational domain with a double periodicity, making use of elliptic functions (see Tricomi [70]) to represent the flow singularities. Then, to describe the blades motion an annular region is considered as reference domain, and two power series are defined in order to impose the impermeability condition (see Milne-Thomson [44]) on the blade contours without introducing

any singularities.

Let's consider now the adopted modelization of the flow field. As formulated in Zanetti [80], the rotational flow is reduced to a potential flow affected by vortex singularities, whose trajectories have then to be computed. The theory of such a kind of flow is already very well established, with the main reference ascribable to Lin [39], where the Hamiltonian theory of vortex motion in multiply connected domains has been set in a general way. Johnson & McDonald [29] have provided a practical example of such a flow model by studying the interaction of vortices with islands in sea motion. They considered the Hamiltonian motion of a vortex in the doubly connected domain bounded by two circular cylinders, assumed as simple models for islands in the sea. Crowdy & Marshall [12] generalized the study to any finite number of circular islands. Further examples of vortex motion, in doubly connected domains, have been presented in Johnson & McDonald [30], who considered the motion of vortices near barrier gaps.

For an inviscid flow with given far-field boundary conditions, the circulations past solid bodies are free parameters which define multiple-flow solutions. In general, physical considerations can help in assuming their values. For instance, in the above-cited works, the circulations around islands are assumed null and, according to Kelvin's theorem, kept constant in time. Nevertheless, such an assumption shares the same arbitrariness as any other assumed initial circulation.

In the inviscid framework, like that here studied, vortex-shedding phenomena can reasonably be described when the considered bodies present sharp edges which force the flow to separate. When using a vortex method, as that introduced and described above, the wake issued by the edges is simulated by adding point vortices which satisfy the Kutta condition at prescribed time intervals. In such a way, the evolution in time of the circulation past each body is defined by the amount of shed vorticity.

In this work what has been investigated for the first time is the motion of vortices in doubly connected domains for the general case of non-null circulations around the bodies. What has been here noted is that, in doubly-connected domains, the imposition of the Kutta condition at the trailing edge of the bodies is not sufficient to uniquely define the flow field, as for the simply-connected domain. So it is shown how Kelvin's theorem can be used to define the time dependence of the complex potential of the motion: considering

the fact that the analytical elliptic function representing the complex velocity is unique only once an additive variable $k(t)$ is defined, the aim was to correlate its computation to the Kelvin's theorem itself. The study has been carried out in collaboration with Gallizio [19]: the flow past a two-element airfoils is there described; in comparison with the two-blade Darrieus turbine here considered, he focused on the modelization of the transient flow after an impulsive start; the profiles being at rest, after a certain time interval a stationary solution is reached, the circulation becoming constant around the bodies and the vortex- shedding phenomena vanishing.

Once the analytical-numerical model was set up, the present work focused on the control of the flow past the Darrieus turbine. In fact, the problem connected to this type of machine is the complicated unsteady flow phenomena occurring during its working cycle, with the consequent rising up of dynamic stall; the uncontrolled flow detachment and vortex-shedding result in high drag and low efficiency, with reduced performances and heavy stress for the structure.

Several interesting and informative review papers related to separation control have appeared in the last decades. Among the others, Gad-el-Hak [16], Gad-el-Hak & Bushnell [17], Stanewsky [68] and Ashill [3]. Traditionally, separation control techniques have been classified as active or passive, depending on whether control involves energy expenditure or not. Separation control strategy often refers to a fluid dynamic plan, which results in a desired alteration or modification of a separated flow. Keeping in mind the major contributions present in literature, it is possible to classify the separation control strategies into the following area:

- methods involving the energization of the boundary-layer upstream of the separation point (e.g. vortex generators, wall suction, tangential blowing, etc.); examples are present in Lachmann [34] and Chang [8]; the boundary-layer is modified in order to be able to meet adverse pressure gradients without separating;
- methods involving the manipulation of the bubble flow; Prandtl [54] demonstrated the use of suction downstream of separation in controlling a diffuser flow at low speeds; the use of base bleed for base-drag reduction is also known (see Bearman [4]): this technique involves injection of low momentum air into the base region to

raise the base pressure. In all these cases of blowing or suction in the bubble the mass balance in the recirculating flow region is affected;

- methods which may affect the shear layer reattachment directly, by means of a steady tangential blowing inside the bubble (see Viswanath [74]), or by means of a passive technique involving porous surfaces (see Rajan [56]).

Because of the energy expenditure required, active control methods are not so useful for a use in vertical axis wind turbines, their principal purpose being to extract as much energy as possible from the environmental conditions. Moreover, the feasibility is the other aspect to be considered in choosing an opportune control technique, which should not be too intrusive, resulting in a not so complex structure. For both these reasons, the strategies listed above are not so good in the case of a Darrieus turbine. Alternatively, recent developments offer a tool to design blades with innovative vortex trapping cavities that act as a passive control device capable of avoiding the vortex shedding. A European research project on this subject is in progress (see [75]). Such devices are mainly investigated to control the stall of aircraft wings. In general, vortex trapping is a technology for preventing vortex shedding and reducing the drag in the flow past bluff bodies. The concept is old (see, for instance, Ringleb [57]). Some experience on studying airfoils with cavities has already been gained, see for instance Iollo & Zannetti [27], Chernyshenko [9], Zannetti [78] and [77], Galletti [18].

Here such ideas are extended to unconventional lift VAWTs (see Zannetti [79]). Since the incidence oscillates between opposite values, the traditional design consists of symmetrical blade sections which operate poorly at high angles of attack. The performance of the turbine can be improved by exploiting the capability of properly designed cavities to stabilize the flow by trapping a vortex. On the resulting blade geometry, the flow past the profile is forced to separate on the edges, vortices are trapped by the cavities and reattachment occurs on the smooth end of the cavities. At stall condition, the erratic unsteadiness of the separation points is avoided, and the flow structure with trapped vortices is preserved. Moreover, since at incidence the trapped vortices are not symmetrical, the airfoil acts as an adaptive airfoil that changes its camber in favour of the incoming flow. This work is an extension of that of Gallizio [19], where the same technology is applied to a single-blade Darrieus turbine: the main difficulty consists in going from a simply connected domain

to a doubly connected domain; however this problem has already been solved previously, so the focus can be only on the resulting flow field past a turbine with blades employing this unconventional shape. Compared to the analytical-numerical method built above, the main change is related to the conformal mapping function. At the moment the main aim being only to illustrate the trapping vortex mechanism, a less in depth study is devoted to the optimization of the shape profile, in particular to that of the cavities; so, even if Ives [28] offers a tool to transform a doubly connected physical domain of general shape into a simpler computational domain, the inverse procedure is used to speed up the computation, following the same spirit as above. A numerical example is performed in order to visualize the resulting flow field, showing that this control technique should be promising for future applications.

1.2 II part

In the second part of this work the aim is to implement a numerical grid-based technique which enables a description of separation phenomena without making use of a body-fitted mesh. Nowadays in problems of practical engineering the need to study the flow field past complex geometries is growing, and, at the same time, computational efficiency and simplification are always desired requirements. These are requests that involve both steady and unsteady flows, with both low and high Mach numbers, which are of usual interest for example in the automotive industry to obtain solutions leading to a reduction in the fuel consumption, in aeronautical design to study the aerodynamics around wings and fuselage in order to optimize their shape, and in the spatial field to model the physics of the environment encountered by reentry vehicles. The presently most employed technique is based on unstructured grids: they enable the treatment of bodies of any shape fitting their contours with the desired precision. But, on the other hand, they also have some drawbacks: the set up of the computation is not immediate, requiring a pre-processing phase to generate an appropriate mesh; the implementation of solving codes is not so simple and linear, requiring a list of the connectivities which specify the way a given set of vertices make up individual elements, a peculiarity that is completely absent for Cartesian meshes; for moving bodies, the grid has to be re-built at each time step, in order to follow the contours during their motion, with the consequent necessity to project the solution

onto the new grid, that results in an increased computational time.

For all these reasons, alternative approaches, based on simple structured Cartesian meshes, have been investigated in the last years. In particular we refer to the so-called *immersed boundary methods*. This term was first used in reference to the method developed by Peskin [50] to simulate cardiac mechanics and associated blood flow. The peculiarity of this method was that the entire simulation was carried out on a Cartesian grid which did not conform to the geometry of the heart, and a novel procedure was formulated for imposing the effect of the immersed boundary on the flow. Since Peskin introduced this method, numerous modifications and refinements have been proposed and a number of variants of this approach now exist. The general idea is to generate the most simple grid with no regard to the body shape, so the Cartesian one is chosen. Because the grid does not conform to the solid boundary, incorporating the boundary conditions would require modifying the equations in the vicinity of the body contours. Then using classical techniques like finite-difference, finite-volume and finite-element approaches, the resulting equations are solved.

The differences between immersed boundary approaches are relative to the way the boundary conditions are imposed on the body contours. In general, the imposition of the boundary conditions implies a modification of the governing equations that takes the form of a source term, or forcing function. According to Mittal & Iaccarino [45], this can be done in two different ways: by means of a *continuous forcing approach*, that is, including the forcing term into the continuous governing equations which will be discretized later; by means of a *discrete forcing approach*, that is, including the forcing term into the discretized governing equations. The first technique has the advantage that it is formulated independently from the spatial discretization adopted; on the other hand, with the second one we can directly control the numerical aspects of the solver, that is, accuracy, stability, etc. But the first technique is simple to implement only when in the domain there are bodies with elastic contours (see, for example, Peskin [51]); for rigid bodies the constitutive laws used for elastic boundaries do not have a good behavior in the rigid limit. The models alternatively developed (for example, Goldstein [22]) have stability and accuracy problems when more precision at the body contours is required, that is, for high Reynolds number flows. In the present work only bodies with rigid contours are taken into account, so the

continuous forcing approach is not desirable.

Let us now consider the discrete forcing approaches: according to Mittal [45], they can be subdivided into two categories, the boundary conditions being imposed in an *indirect* or *direct* way. Using the indirect technique means extracting the forcing term directly from the numerical solution for which an a priori estimate can be determined (see Mohd-Yosuf [46]). Such an approach is desirable because of the absence of user-defined parameters and the elimination of the associated stability constraints; but on the other hand the forcing is represented by a smooth distributed function which affects also the exterior fluid in the proximity of the body contours. In this work we want to implement a code able to treat both low and high Reynolds number flows; in this second case a good precision is required near the body contours, so the indirect approach lastly described cannot be a good choice.

We now describe the discrete forcing techniques which provide a direct imposition of the boundary conditions. The idea is to keep the body contours as sharp interfaces without spreading, going in the direction of increasing the accuracy near the boundaries. Two are the most used approaches:

- *ghost-cell technique*: it works well in conjunction with the finite-difference method; it is based on the definition of ghost-cells as the cells in the bodies that have at least a neighbour in the fluid; for each ghost-cell an interpolation scheme that implicitly incorporates the boundary condition on the body contour is then devised. One simple scheme that could be used is based on bilinear interpolation, however a long list of options is present in the literature: see, for example, Majumdar [41], Iaccarino & Verzicco [26], Tseng & Ferziger [72], Ghias [20];
- *cut-cell technique*: it works well in conjunction with the finite-volume method, because the idea is to preserve the conservation of mass, momentum and energy in the cells cut by the body contours. The cut cells whose center lies outside the body are separated into two parts: the solid one is discarded, while the fluid one is joined to the neighbouring fluid cell generating a trapezoidal cell. The computation of the gradients at the interfaces is then performed by means of appropriate interpolation schemes. Examples are, among the others, Ye [76] and Mittal [45].

For our use these techniques could represent a good alternative; however they have

two inconveniences: first, the use of interpolation methodologies enables the treatment of very complex geometries, which results in complex algorithms; secondly, their increased complexity when there is the need to study moving bodies. This is why we preferred to implement the code using the Brinkman penalization technique. The basic idea, introduced for the first time by Arquis & Caltagirone [2], is to consider the solid bodies in the domains as porous media, with the porosity tending to zero. This corresponds to a Brinkman-type model, where the fluid domain has a large permeability compared to that of the porous media. Initially the method was applied to incompressible flows (see Angot [1]): the boundary conditions are imposed by adding penalization terms to the momentum equations; the immersed boundaries in fact exert localized forces to the fluid implying the modification of these equations; in this way the velocity is forced to satisfy the no-slip condition on the body contours. The bodies are identified by means of the Heaviside function, which takes a value of 1 in the solid and of 0 in the fluid; in this way, outside the obstacles the original Navier-Stokes equations are solved, while in the bodies the complete penalized equations are taken into account. The treatment of geometries of any shape is then rather automatic, further shrewdnesses being not necessary when the body contours become more complex. A great advantage of this approach is that the error is always rigorously known, being determined by the adopted penalization parameter.

In the literature several works are present where the penalization technique is applied to the study of incompressible flows; among others, Angot [1] and Kevlahan & Vasilyev [31]. On the other hand, the application to compressible flows has not been investigated as much. One of the first works is that of Boiron [6], which is the continuation of Chiavassa [10]: apart from penalizing the momentum equations, the energy equation is also modified in order to impose, with the same spirit as for the no-slip condition, the boundary condition on the temperature. Another recent work to be considered is that of Liu [40], where the aero-acoustic problems are treated: in addition to penalizing momentum and energy equations, a modified continuity equation is considered in the bodies which takes into account the porous nature of the media; in this way bodies act as high impedance media, avoiding the wave transmissions into themselves.

In the present work the penalized technique proposed by Boiron [6] and Chiavassa [10] is used to verify its applicability not only to supersonic, but also to subsonic flows. It is

applied to a Navier-Stokes first- and second- order solver codes implemented by means of a finite-volume approach, and tested for the Euler and viscous parts separately. As a result, the momentum and energy equations are modified by the addition of source terms, which enable the exact boundary conditions to be imposed on the body contours. An explicit treatment is not feasible due to the untractable time step restrictions imposed by the penalisation parameter; then a semi-implicit approach is first implemented, where the convective and diffusive terms are treated explicitly, and the penalized ones are treated implicitly, as in Boiron [6]. However this method results in not so good computational time efficiency, which remains limited by the stability restrictions on the convective and diffusive terms. So an implicit scheme is proposed, which results in CFL numbers at least ten times larger. Both the methods, the semi-implicit and the fully implicit, are tested by means of comparison with results obtained by classical unstructured body-fitted grid approaches for the subsonic unsteady flow case (the von Kármán street past a confined square cylinder is considered) and by those shown in Boiron [6] (the detached shock in front of a circular cylinder and the interaction between a circular cylinder and a moving shock). Good agreement was obtained.

Finally, to give an example of the power of the implemented technique a situation is analysed where a circular cylinder is moving in a stagnant fluid in the proximity of a rectangular cylinder at rest. This case is useful to show how fast and easy to set up a moving boundary problem can be, if treated by means of the penalization approach here investigated.

Part I

Unsteady incompressible and inviscid flow model

Chapter 2

Study of a VAWT

In the present work, as sample of 2D incompressible flow presenting unsteady separation phenomena, the flow field around a Vertical Axis Wind Turbine (VAWT) is studied. Before starting to describe the model developed to analyse this kind of flow, to introduce the study of this particular architecture a brief review is made of the currently employed wind turbines. The most used wind turbines are nowadays the Horizontal Axis ones (HAWT), that have blades which rotate vertically around a horizontal axis. They are propeller turbines, needing to be oriented perpendicularly to the direction of the wind to be efficient, and they are generally placed on the top of very tall poles to take advantage of higher wind speeds. The blades are designed to use the lift they create to propel themselves around faster than the speed of the wind. Typically their tip-wind speed ratios are in the range of 7-15. This is advantageous for energy production, but the main drawback is that high rotational speeds can create high levels of noise. Also, to keep these turbines safe while running at such high speeds, propeller turbines require the use of special controls, such as furling or alternate breaking systems. Another problem is connected to the position of generators and gearboxes, which tend to be inaccessible at the top of the structure's tower.

VAWTs have a feature that is particularly attractive: they accept wind from any horizontal direction. This technology has been blowing around for decades, but despite many advantages it has so far attracted little interest. Nowadays however this is about to change. VAWTs are a type of wind turbines where the main rotor shaft runs vertically.

Compared to the HAWTs, they are not as efficient, but they do offer benefits in low wind situations, they tend to be safer and are easier to build. Among the advantages of this arrangement, a couple of ones are that generators and gearboxes can be placed close to the ground (resulting in a simpler structure) and that a VAWT doesn't need to point into the wind (working equally well no matter which direction the wind is coming from). On the other hand, the major drawbacks are the pulsatory torque that can be produced during each revolution and the huge moments on the blades.

According to [42], unchanging for all wind turbines are a number of crucial factors that together determine the energy-generating potential in kWh/m^2 of rotor swept area; their physical relationship can be expressed by means of the following formula:

$$P = C_P \eta_{me} \eta_{el} \frac{1}{2} \rho v^3 A$$

where P [Watt] is the wind turbine generated power; C_P the power coefficient, that is the aerodynamic efficiency of conversion of wind power into mechanical power; η_{me} the conversion efficiency of the mechanical power at the rotor axis into the mechanical power at the generator axis; η_{el} the conversion efficiency of mechanical power into the energy ready to be spent outside, as the electric one; ρ the air density [kg/m^3]; v [m/s] the wind speed evaluated three rotor diameters upwind from the rotor plane; A the rotor swept area [m^2]. One of the key performance differences in wind turbine designs is caused by the driving mechanism of the rotor. A wind turbine rotor can either be turned around by the aerodynamic drag or by the aerodynamic lift of rotor blades. With drag-driven wind turbines, the rotor blades are pushed around by the wind and move in the same direction. Such turbines typically combine a small C_P with a high materials requirement, so they are rather expensive to build in comparison with their comparatively limited power output. The Savonius turbine is one of the best known drag-type wind turbines (Figure (2.1)). It consists of two or three scoops. Because of the curvature, the scoops experience less drag while moving against rather than with the wind. The differential drag causes the turbine to spin. In the classical configuration it is characterised by a high starting torque and by an aerodynamic efficiency that cannot compete with high-speed propeller and Darrieus-type (which will be introduced later) wind turbines. And, even if promising studies are now being carried out about new configurations, for example on the employment of twisted

blades as in [23], we are still far from a large use of this machine in the energy supplier field.

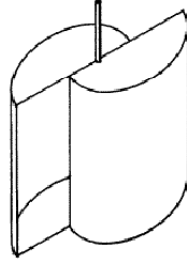


Figure 2.1. Savonius turbine scheme.

The other type of VAWT is the lift-driven turbine, in particular the Darrieus-type one. It consists of a number of airfoils vertically mounted on a rotating shaft: in (Figure 2.2) a curve-blade- and a straight-blade-type are shown. The airfoils are usually symmetrical and properly mounted so as to keep a zero rigging angle (the angle they have relative to the structure on which they are plugged in). The first configuration was discovered and patented by Darrieus(1931). As reported by [65], during the early seventies first tests on this configuration was performed at the National Research Council, Canada, which showed that the device worked efficiently at high tip speed ratios, but had poor starting torque.

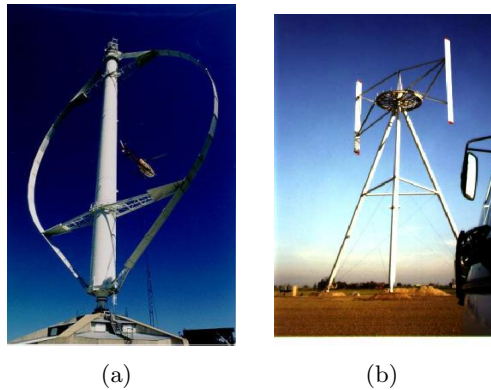


Figure 2.2. Examples of Darrieus turbines: the curve-blade-type (a) and the straight-blade-type (b).

To understand how the machine works, we consider (Figure 2.3): a blade section is shown in the plane normal to the shaft at different azimuthal positions ϕ for a given wind speed V_∞ and angular velocity Ω . Normally the Darrieus turbine works at high tip speed

ratios; under these conditions, the lift L exerted on the blade is always directed in a way that produces a positive torque to the shaft, thus helping it to rotate in the direction it is already running; obviously, at the same time a drag force D acts on the blades opposing to their motion. During each revolution, the angle of attack α gets values of opposite sign, but the generated force is still oblique in the direction of rotation because the profiles are symmetrical and the rigging angle is zero.

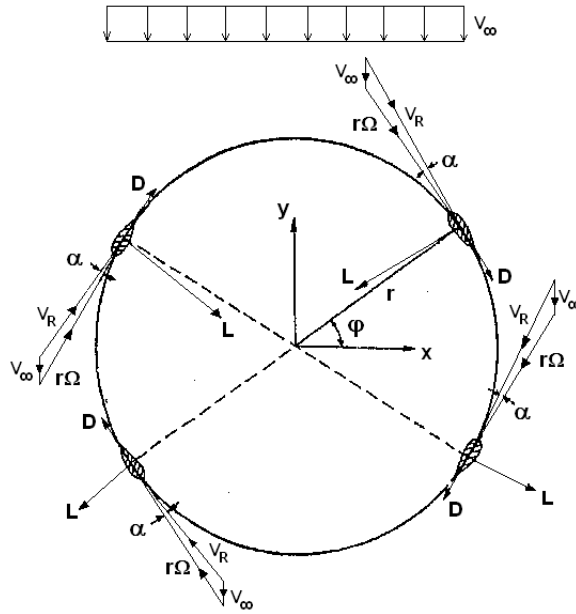


Figure 2.3. General working cycle of a Darrieus turbine: the lift L always generates a positive torque.

Darrieus-type turbines are nowadays a promising technology in the field of the VAWTs. In comparison with the other types, they present several advantages (see [67]): low sound emissions, consequence of its operation at lower speed ratios; insensitivity to yaw wind direction; an optimum power generation when the oncoming flow is skewed (see [43]).

In the present work, the flow field past a classical 2-blade Darrieus turbine is defined and investigated. Its most interesting feature is the complete unsteadiness, due to both the vortical structures which detach from the blades and the motion of the profiles with respect to the wind. The unsteady aerodynamic behavior due to the variation of the incidence with the angle of rotation generates the phenomenon of dynamic stall, which has a significant impact in both loads and power. The consequences are uncontrolled

vortex shedding phenomena, which result in a higher drag and a lower efficiency.

The first issue here addressed is to define a so-complex flow field, characterized by moving bodies in a doubly-connected domain, by means of an opportune analytical-numerical model; then, an innovative idea is proposed in order to reduce and control these phenomena by means of the vortex trapping cavities inserted on the blade contours, applying a technology which is being developed for the airplanes that have to fly at high angles of attack.

2.1 Flow field simulation: modeling tools

The subject of the study is the modeling of the flow field past a classical 2-blade Darrieus turbine. The simulation is performed in the two-dimensional space domain corresponding to the middle section normal to the shaft of a turbine with infinite aspect ratio. This restriction simplifies the solution considerably, however sufficiently far from the extreme points it is an inherently approximation, the resulting blade profiles rotating in the same plane as the approaching wind. In the 2-D plane the turbine results in two profiles which can be superimposed by a π rotation; they are assumed as spinning at the angular velocity Ω and also as experiencing a uniform flow from infinity which represents the wind speed (see Figure 2.4). These two velocities being unrelated, the computations must be performed at a specific ratio between them.

2.1.1 Classical approaches

Classical numerical approaches to the study of such complicated dynamic stall and vortex shedding phenomena are performed by means of the CFD tools, that is, by opportune turbulence and large eddy models, as in [67]. Using these techniques there are some problems to be faced: the geometry of the rotor and its rotating motion don't enable spatial/time grid simplifications; the large amount of the shed vorticity implies that the model could be sensitive to numerical dissipation; the development of the flow field being characterized by the interaction of the blades with the shed vorticity previously generated, a very fine grid over the entire rotor domain is necessary in order to avoid numerical dissipation.

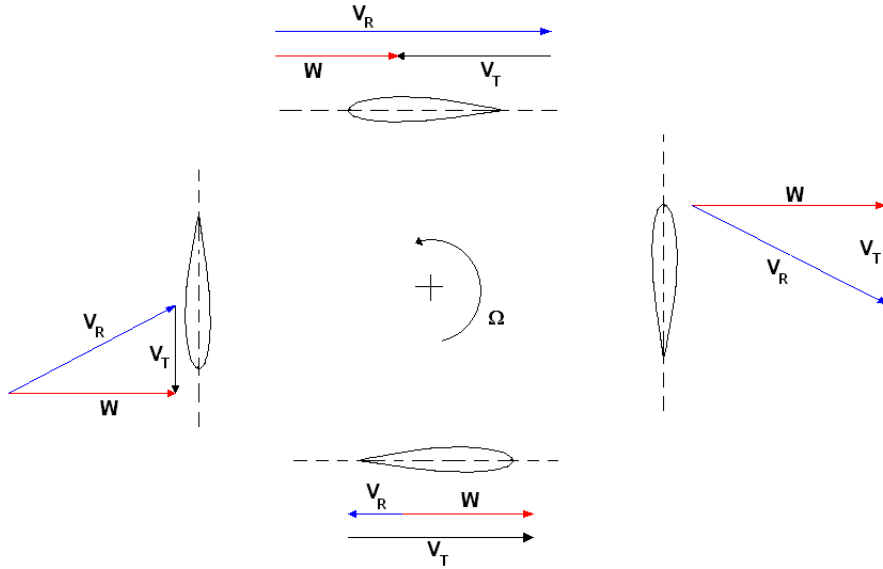


Figure 2.4. Situation analysed during a working cycle: W is the wind speed, V_T the tangential velocity due to the rotation around the vertical shaft, V_R the effective velocity experienced by the blades.

The investigation is performed neglecting the diffusion effects, so the flow can be assumed as inviscid and governed by the Euler equations. Another classical approach that can be used is then represented by the vortex panel method. We now briefly describe its main features: considering a general airfoil, it consists in dividing it into N piecewise straight line panels of index $i, i = 1, \dots, N$, on each of which a vortex sheet of strength $\gamma(s_i)ds_i$, ds_i being the length of the i -th panel, is placed in order to give rise a circulation and then lift. In general the strength of a panel can vary along its length in an arbitrary way; the most common is to assume a linear distribution, imposing that the strength is continuous across each m -th panel joints, $m = 1, \dots, N + 1$, except at the trailing edge. The more panels, the more accurate the solution. Each panel is defined not only by its two end points of index m , but also by the control point of index i , located at the panel center, where the impermeability boundary condition $\frac{\partial \phi_i}{\partial n_i} = 0$ is applied, n_i being the normal to the i -th panel and ϕ_i the potential on the i -th panel. According to the complex potential theory, the potential ϕ at a point $\bar{r}_i = (x_i, y_i)$, due to the freestream (u_∞, v_∞) velocity and to the vortex strength distribution $\gamma(s_j)$ on each panel may be written by the following expression, where the integral is taken along each panel whose extreme points have indexes j and $j + 1$, $j = 1, \dots, N + 1$:

$$\phi(x_i, y_i) = u_\infty x_i + v_\infty y_i - \sum_{j=1}^{N+1} \frac{1}{2\pi} \int_0^{l_j} \gamma(s_j) \theta_{j,i} ds_j$$

$\theta_{j,i}$ being the angle between the horizontal direction and the direction of the line connecting the points \bar{r}_j and \bar{r}_i , and l_j the length of the j -th panel. Imposing the impermeability condition on each panel, we obtain a system of N equations with $N + 1$ unknowns, the vorticities at the trailing edge point being different. The last equation is determined by imposing the Kutta condition, that is, imposing that the flow must smoothly leave the trailing edge in the same direction at the upper and lower edge, which is guaranteed if $\gamma_1 = -\gamma_{N+1}$. Solving this linear system, the circulation is obtained for every panel, so the flow field can be completely determined.

In Deglaire [13] the flow around a simple circular geometry is solved in order to evaluate the time efficiency performance of the vortex panel method. It has been obtained that it is slower in comparison with a method which combines a conformal mapping and a vortex method based on a fast imaging procedure. Here we follow the same idea: that is, instead of using a vortex panel method, a conformal mapping procedure is adopted in order to solve the flow field in a simpler domain than the physical one: but, about the vortex method, we were only interested in a method which enabled an accurate description of the dynamics of the flow field, not in its efficiency. So a classical point vortex method is used, which requires a number of computations of $O(N^2)$, N being the number of point vortices in the flow field, while more efficient methods require only $O(N \log(N))$ or $O(N)$ operations (see, for example, [14] and references therein).

2.1.2 The analytical-numerical approach

It is founded on the conjugation of two different tools, an analytical one, that is, the conformal mapping, and a numerical one, that is the point vortex method. The usual strategy to solve the flow field can be subdivided into these steps: the physical domain is transformed into a simpler computational domain; here, the vorticity being discretised by means of vortex singularities, the flow field is solved integrating in time the resulting complex velocities of each vortex point; their computed positions are finally transformed into the real ones in the physical plane.

Analytical tool

The definition of an oportune conformal mapping is the first task to be accomplished. We start with a brief description of what has already been done in the literature, keeping in mind that, when we talk about a plane, a complex plane is considered. We are dealing with a doubly connected domain, that is, according to [71], with a domain where closed curves can be defined which, to be reduced to a single point, have to cross the boundary once. In [28] and [24] two different approaches to conformally map multi-connected domains are presented, the former being better adapted to the doubly-connected case, the second to the pluri-connected one. So here we are interested in considering the approach of [28]; it is built for the transformation of a two-element airfoil, but it can be applied also in our case of two profiles rotated of π one in respect to the other. Starting from the mapping of one airfoil into a unit circle, it maps the second airfoil into another circle centered in the origin, in order to obtain an annular region. The complete transformation can be broken down into the following steps, keeping in mind that what is applied to one airfoil is also applied to the other:

- by means of a classical Kármán-Trefftz mapping, the trailing edge discontinuity of the first airfoil in the physical z -plane is removed, obtaining a regular near-circle in the z_2 -plane;
- the centroid of the new-defined geometry is translated to coincide with the origin of the reference system in the z_3 -plane;
- the near-circle is now determined by a series of points: a continuous representation of its contour is obtained by means of a cubic spline interpolation;
- the step which concludes the transformation of the first airfoil is represented by the Theodorsen-Garrick mapping; it is defined by the following function:

$$z_3 = z_4 \exp\left[\sum_{j=0}^N (A_j + iB_j) z_4^{(-j)}\right]$$

where $z_3 = r(\theta)e^{i\theta}$ is the polar coordinate representation of the near-circle and $z_4 = e^{i\theta}$ is the representation of the desired image of the first airfoil, that is, of a

unit circle. The coefficients A_j and B_j are computed by means of the Fast Fourier technique conjugated with an iterative process; this is the first iterative procedure employed in this method;

- we pass to the second airfoil; firstly, a Kármán-Trefftz mapping is applied in order to remove the discontinuity, while keeping the image of the first airfoil a circle with a new radius R ; the new z_5 -plane is then defined;
- by means of a bilinear transformation the new near-circle is moved inside the old one; the coefficients defining this mapping function are determined in a way such that the centers of both the circle and the quasi-circle coincide with the origin of the new defined z_6 -plane; the second iterative procedure is employed in this step;
- to conclude the entire transformation a Garrick-type mapping is defined with which one can obtain, in the computational domain z_7 , a perfect annular region, bounded internally by the image circle of the second airfoil and externally by the unit circle corresponding to the previously mapped airfoil; the coefficients by which this transformation is determined are computed by means of the Fast Fourier technique.

As can be observed, in the conformal mapping proposed by Ives a lot of iterative procedures are present. Even if in the single direct transformation from the physical to the computational plane it doesn't represent large time losses, when it has to be performed in another iterative process like that of a discrete vortex method this is not so efficient. Moreover, in the present analysis we don't have to analyse a specific physical configuration of the Darrieus blade, so what will be done in the next chapter is to create a new conformal mapping which enables the transformation of an annular region in the computational domain into a two Kármán-Trefftz-like airfoils in the physical plane representing as well as possible the geometry of a VAWT.

Numerical tool

Before describing in detail how the model was built we also have to introduce the concept of *vortex method*, in particular of the discrete-type like the one we employ, and the problems connected to it. As said above, the flow here analysed is governed by the 2D incompressible Euler equations:

$$\frac{\partial \vec{u}}{\partial t} + (\vec{u} \cdot \nabla) \vec{u} = -\frac{\nabla P}{\rho} \quad (2.1)$$

where \vec{u} is the fluid velocity, P is the pressure, and ρ the fluid density. We take the curl of this equation; the static pressure term disappears; the term $(\vec{\omega} \cdot \nabla) \vec{u}$, which describes the rate of deformation of vortex lines is zero, being in a two-dimensional framework, and the vorticity, having only one component ω , which is in the direction normal to the plane, is a scalar quantity. Then, from the Euler equations, the following vorticity transport equation is obtained:

$$\frac{D\omega}{Dt} = \frac{\partial \omega}{\partial t} + (\vec{u} \cdot \nabla) \omega = 0 \quad (2.2)$$

Vorticity is then a scalar quantity carried along particle paths, which suggests a computational method based on tracking particles and thereby evolving the vorticity field associated with those particles. To find the velocity field given the vorticity, we also need to remember the relationships between the streamfunction ψ and the velocity components, that is, $u = \frac{\partial \psi}{\partial y}$ and $v = -\frac{\partial \psi}{\partial x}$, and the streamfunction and the vorticity, that is, the Poisson equation $\omega = -\nabla^2 \psi$. Following [52], by means of the Green's function definition for the 2D Laplacian and by means of the complex coordinate $z = x + iy$, it can be deduced that the velocity $v_{vort}^*(z_0)$ induced in a generic point z_0 by a distributed vorticity $\omega(z)$ can be defined with this expression:

$$v_{vort}^*(z_0) = \frac{1}{2\pi i} \int \int_S \frac{\omega(z)}{z_0 - z} dz \quad (2.3)$$

with the integral being taken on the vorticity region S and the $*$ denoting the complex conjugate value. Now, depending on the way of discretizing the vorticity $\omega(z)$, three classical methods can be deduced to solve the flow field which we only mention for now:

- *contour dynamics method*: $\omega(z)$ is confined in a finite number N_R of regions A_j of uniform vorticity ω_j , that is: $\omega(z) = \sum_{j=1}^{N_R} \omega_j H(A_j)$, where H represents the Heaviside function, which takes a value of 0 outside the region A_j and of 1 inside. The equation (2.3) then takes the following form:

$$v_{vort}^*(z_0) = \sum_{j=1}^{N_R} \frac{\omega_j}{2\pi i} \oint_{\partial A_j} \ln(z_0 - z) dz \quad (2.4)$$

the integration being taken along the contour ∂A_j of each region A_j ;

- *vortex sheet method*: $\omega(z)$ is confined into a finite number N_C of contours C_j with vortex distribution $\gamma_j(s)$, s being the coordinate along C_j , that is, $\omega(z) = \sum_{j=1}^{N_C} \gamma_j(s) \delta(z - z_j(s))$, with δ representing the Dirac delta function; the equation (2.3) results modified in this way:

$$v_{vort}^*(z_0) = \sum_{j=1}^{N_C} \frac{\omega_j}{2\pi i} \int_{C_j} \frac{\gamma_j(s)}{z_0 - z_j(s)} \left| \frac{dz}{ds} \right| ds \quad (2.5)$$

- *point vortex method*: $\omega(z)$ is confined into a finite number N_V of points z_j , that is, $\omega(z) = \sum_{j=1}^{N_V} \gamma_j \delta(z - z_j)$, where γ_j is the circulation associated to each point vortex; the equation (2.3) becomes:

$$v_{vort}^*(z_0) = \sum_{j=1}^{N_V} \frac{1}{2\pi i} \frac{\gamma_j}{z_0 - z_j} \quad (2.6)$$

The last method is the approach we will follow forward. Due to the unsteadiness of the flow field, vorticity is shed from the blades into the wakes. The discrete vortex method adopted (see, for instance, [11]) describes the wakes by concentrating the vorticity in point vortices. According to such a model, at fixed time steps, a point vortex is added to each blade in a fixed location close to the trailing edge, with a circulation γ_j defined by the Kutta condition. As the vortices move, the Kutta condition is violated, but it is restored as soon as another two vortices are released, and so on.

This discrete approximation of the continuous evolution of smooth trailing-edge vortex sheets has been discussed in the literature (see, for instance, [11], [63], [32], and references therein). A heuristic choice of parameters, as release timing and location, is required. This choice has a negligible effect on a possible asymptotic steady solution, but it affects the accuracy of the description of an unsteady flow field. The vortex method here used

is the same as in [81], where the choice of the parameters was based on the thumb rules suggested in literature and on numerical experiments. A sort of validation is obtained by checking the ability of the method to predict the correct Strouhal numbers of flat plates at incidence and to provide the self-similar structure of rolled-up vortex-sheets (see [55]).

The results are obtained in the limit of an inviscid model and do not take into account the possible local occurrence of secondary separations. Nevertheless, they are meaningful for two main reasons: firstly, inviscid vortex methods, as the one here adopted, are able to describe the vortex shedding phenomena past bluff bodies with the correct Strouhal number: in fact, the Kutta condition models the main viscous effect causing flow separation, then inertia rather than vorticity governs the global instability of these phenomena. Secondly, the instability that is triggered by secondary separations due to local adverse pressure gradients has a characteristic relaxation time: if this time is greater than the turbine period the instability could not be triggered.

In this framework, we have to face a peculiar problem. We are dealing with an inviscid flow with given far-field boundary conditions; in a case like this, the circulations past solid bodies are free parameters. So, *how* to determine them? In general, physical considerations can help in assuming their values. For example, in [29] and [12] the flow field generated by vortex motion is studied around two or more islands assuming that at the initial time the circulation around them is null; and the evolution in time of the resultant flow field is described imposing the respect of the Kelvin theorem, that is, maintaining the circulation equal to the initial zero value. However assuming a different initial value can lead to another correct possible solution, demonstrating the absolute arbitrariness of this choice. In the present case, we are dealing with moving bodies around which the circulation is non-null and varies in time because of the unsteadiness of the flow field; in a simply-connected domain the imposition of the Kutta condition would be sufficient to completely define the flow field and then also the circulation around the body, because it results equal to the opposite value of the shed vorticity. But in a doubly-connected domain we will show that this is not true; imposing the Kutta condition on the trailing edge of both the blades doesn't uniquely define the flow field; in addition to these two conditions a third one has to be imposed, which allows the Kelvin theorem to be satisfied.

Chapter 3

Model-building

3.1 Conformal mapping

As previously explained, since, in the present work, the principal aim is to address the definition of the unsteady two-dimensional rotational flow field past a generic two blade vertical axis wind turbine, the mapping sequence suggested by Ives is reversed to avoid the numerical part of the transformation, simplifying and speeding up the computation. A new mapping chain is defined which maps the computational domain into the physical one.

The first difficulty in developing a conformal mapping method for a doubly connected domain is the choice of a suitable mapping domain. In the case of a single blade, the Riemann mapping Theorem assures that any body can be mapped onto a unit circle. According to the same theorem, any doubly connected domain can be conformally mapped onto the annular region between two concentric circles with fixed radius ratio. So a mapping chain is built which transforms, in closed form, two given circles defining an annular region in the μ -plane into two airfoils in the physical z -plane, passing through two symmetric circles in the ν -plane. We describe the two steps of this transformation.

3.1.1 From μ -plane to ν -plane

We consider the annulus formed by the circles centred on the origin of the μ -plane and with the radii $L < 1$ and $\frac{1}{L}$, respectively (Figure (3.1)). To obtain a couple of circles

symmetrical with respect to the real axis, the function (3.1) is used:

$$\nu(\mu) = i\eta_0 \frac{1 + \mu}{1 - \mu}, \quad \eta_0 \in \Re \quad (3.1)$$

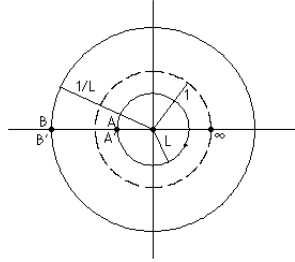


Figure 3.1. Annular region in the μ -plane.

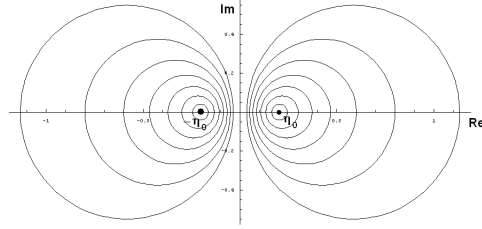


Figure 3.2. Apollonius circles with foci in $\pm\eta_0$.

Being a bilinear transformation, it maps circles onto circles. The choice of the coefficients in the fractional part is made so as to obtain the Apollonius circles having the foci in $\pm\eta_0$, as visualized in Figure (3.2).

The multiplication for $-i$ rotates the structure of the angle $\frac{\pi}{2}$ counterclockwise; the result is in Figure (3.3): two symmetrical circles having the foci at $\nu_0 = \pm i\eta_0$, centers at $\nu_c = \pm\nu_0 \frac{1+L^2}{1-L^2}$ and same radius $\rho_c = \eta_0 \frac{2L}{1-L^2}$. The ring is mapped onto the domain of the ν -plane bounded by the two c_u and c_d circles in a way that the region inside the unit circle of the μ -plane is mapped onto the positive imaginary half- ν -plane and the outside region onto the negative half-plane. The unit circle centered on the origin of the μ -plane results in the real axis of the ν -plane, with $\mu = +1$ and $\mu = -1$ having their images in $\nu = \infty$ and $\nu = 0$, respectively.

3.1.2 From ν -plane to z -plane

To map two generic circles onto two generic profiles a combination of two inverse Kármán-Trefftz transformations can be used, resulting in an expression of the form of (3.2), where z_{T_1}, z_{T_2} and z_{N_1}, z_{N_2} are the trailing edge points and internal points of the profiles, respectively, μ_{T_1}, μ_{T_2} and μ_{N_1}, μ_{N_2} being their images, and τ_1, τ_2 are computed from the trailing edge angles $\varepsilon_1, \varepsilon_2$ of the profiles:

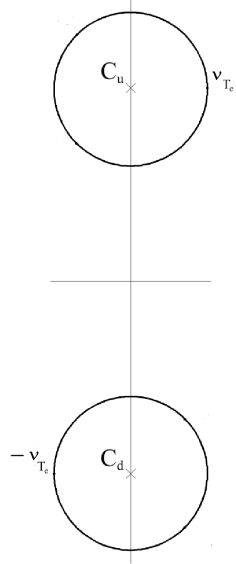


Figure 3.3. Symmetrical circles with respect to the real axis; ν -plane.

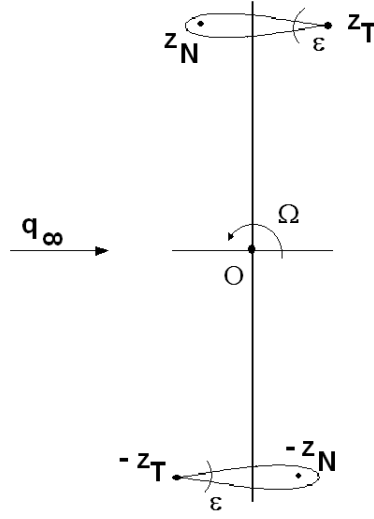


Figure 3.4. Physical z -plane: two-blade Darrieus turbine with angular velocity Ω experiencing the wind speed q_∞ .

$$\frac{z - z_{T_1}}{z - z_{N_1}} \cdot \frac{z - z_{T_2}}{z - z_{N_2}} = \left(\frac{\nu - \nu_{T_1}}{\nu - \nu_{N_1}} \right)^{\tau_1} \cdot \left(\frac{\nu - \nu_{T_2}}{\nu - \nu_{N_2}} \right)^{\tau_2} \quad \tau_{1,2} = 2 - \frac{\varepsilon_{1,2}}{\pi}. \quad (3.2)$$

The aim is to obtain two blades that can be superimposed through a rotation of π , so the used mapping function is:

$$\frac{z^2 - z_T^2}{z^2 - z_N^2} = \left(\frac{\nu^2 - \nu_T^2}{\nu^2 - \nu_N^2} \right)^\tau, \quad \tau = 2 - \frac{\varepsilon}{\pi}. \quad (3.3)$$

Besides η_0 , introduced in the transformation from the μ -plane to the ν -plane, the blade geometry and turbine aspect ratio are defined by the parameters ν_T and ν_N , with $\pm\nu_T$ being relevant to the trailing edges and $\pm\nu_N$ being inside the circles. What has to be still computed is the value of z_T and z_N . Three conditions could be imposed:

$$z(0) = \nu(0) \tag{3.4}$$

$$\lim_{\nu \rightarrow \infty} \left(\frac{dz}{d\nu} \right) = 1 \tag{3.5}$$

$$\lim_{\nu \rightarrow 0} \left(\frac{dz}{d\nu} \right) = 1. \tag{3.6}$$

The unknowns being two, one of the above expressions is redundant; in particular the choice is between (3.5) and (3.6); imposing (3.6) means that the flow at infinity is rotated; Equation (3.5) implies that a rotation is applied to the flow near the origin. For the sake of simplicity, conditions (3.4) and (3.5) are chosen. Starting from Equation (3.4) it follows:

$$\left(\frac{z_T}{z_N} \right)^2 = \left(\frac{\nu_T}{\nu_N} \right)^{2\tau}. \tag{3.7}$$

While from Equation (3.5):

$$\begin{aligned} \frac{dz}{d\nu} &= \tau \cdot \frac{\frac{1}{1-(\nu_T/\nu)^2} - \frac{1}{1-(\nu_N/\nu)^2}}{\frac{1}{1-(z_T/z)^2} - \frac{1}{1-(z_N/z)^2}} \cdot \frac{z}{\nu} \\ &= \tau \cdot \frac{1 + \left(\frac{\nu_T}{\nu}\right)^2 + O\left(\frac{\nu_T}{\nu}\right)^3 - 1 - \left(\frac{\nu_N}{\nu}\right)^2 - O\left(\frac{\nu_N}{\nu}\right)^3}{1 + \left(\frac{z_T}{z}\right)^2 + O\left(\frac{z_T}{z}\right)^3 - 1 - \left(\frac{z_N}{z}\right)^2 - O\left(\frac{z_N}{z}\right)^3} \cdot \frac{z}{\nu} \\ &\simeq \tau \cdot \frac{\nu_T^2 - \nu_N^2}{z_T^2 - z_N^2} \cdot \left(\frac{z}{\nu}\right)^3 \end{aligned}$$

$$\lim_{\nu \rightarrow \infty} \left(\frac{dz}{d\nu} \right) = \tau \cdot \frac{\nu_T^2 - \nu_N^2}{z_T^2 - z_N^2} \cdot \lim_{\nu \rightarrow \infty} \left[\left(\frac{z}{\nu}\right)^3 \right] \simeq \tau \cdot \frac{\nu_T^2 - \nu_N^2}{z_T^2 - z_N^2} \cdot \left(\frac{dz}{d\nu}\right)^3 = \frac{dz}{d\nu}.$$

Then:

$$z_T^2 = \tau \cdot \nu_T^2 \cdot \frac{1 - (\nu_N/\nu_T)^2}{1 - (\nu_N/\nu_T)^{2\tau}} \tag{3.8}$$

The resulting geometry is depicted in Figure (3.4), in all being defined by 5 parameters: L , η_0 , ν_T , ν_N and ε , three real and two complex.

3.2 Definition of the complex potential

The description of the flow field in the computational domain passes through the definition of the complex potential. The basic aspect to be handled and to be taken into account is that the blades are considered to spin around the origin of the physical plane. According to the Milne-Thomson approach [44], the complex potential w of the absolute motion is expressed in a frame of reference which moves with the body, that is, the z -plane is considered as rotating around its origin with the turbine angular velocity Ω . According to the absolute nature of the flow motion, the streamfunction is not constant on the blade contours, but has values that have to be defined by the condition of impermeability. So, the complex potential can be expressed as the sum of two terms, $w = w_1 + w_2$, where w_1 is such that the streamfunction on the blade surfaces will have a constant value, while w_2 is such that the streamfunction will assume the values which satisfies the impermeability condition.

In other words, w_1 is the complex potential of a flow field where the turbine is considered at rest: to reproduce the physics of phenomena, the computational domain is transformed further on into a region, a rectangle, where the flow field will be described in a simpler way by means of elliptic functions. On the other hand, w_2 represents only the motion of the blades, and it will be defined directly in the μ -plane by means of appropriate Laurent series.

3.2.1 Turbine at rest

In order to define the flow field, it is convenient to map the region bounded by the airfoils, that is, the region between the μ -plane concentric circles, inside a rectangle of the complex χ -plane, as shown in Figure (3.5).

By the logarithmic transformation:

$$\chi = \log(\mu) \tag{3.9}$$

the annulus is mapped onto the rectangle with edges at the points $\chi = \pm \log L \pm i\pi$, the images of the two circles coinciding to the sides $\Re(\chi) = \pm \log L$.

The resulting mapping chain from the χ -plane to the z -plane is such that the left-hand

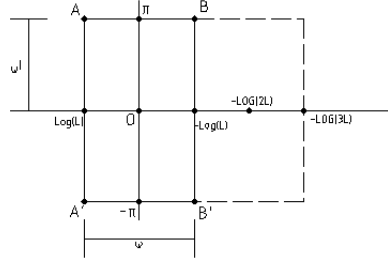


Figure 3.5. Computational domain in the transformed χ -plane.

side of the above-defined rectangle is mapped onto the blade in the positive-imaginary half- z -plane, the right-hand side onto the blade in the negative-imaginary one, and the origin onto the point at infinity of the z -plane. The upper and lower sides of the rectangle are periodic boundaries that correspond to a single line which connects the two blades of the turbine.

Following the same reasoning as Lagally [35] and Ferrari [15]), the complex velocity $\frac{dw}{d\chi}$ in the χ -plane, with w denoting the complex potential, has to be expressed by a doubly periodic function. Considering the turbine as standing at rest, the impermeability condition of the solid boundaries, that is, the constant value of the streamfunction on the blades, can, in fact, be enforced by infinite reflections with respect to the sides of the rectangle and, as a consequence, the complex velocity has to be periodic in both the directions, the real one and the imaginary one, with semi-periods $\omega = -2 \log L$ and $\omega' = i\pi$. This function must have a second order pole to represent the wind velocity, and first order singularities to represent the vortex points.

Among the elliptic functions, the \wp , ζ and σ Weierstrass functions are chosen. To describe and verify their use and their effect on the resulting flow field in the transformed χ -plane, we have a look to their features singularly. According to Tricomi [70] and to the above-stated double periodicity, the fundamental area which to build the complex velocity $\frac{dw}{d\chi}$ and potential w into is represented in Figure 3.5. The singularities and the poles have to be placed in a way such that the side at $\Re(\chi) = -\log(L)$ is a streamline, that is, $\Re\left[\frac{dw}{d\chi}\right] = 0$. The extension of this feature to the side at $\Re(\chi) = \log(L)$ will be automatic, for the properties of elliptic functions.

To represent an asymptotic flow which assumes the complex value a in the χ -plane, a second order pole, by means of the \wp function, must be put on the origin, the flow arriving

from and coming back to the infinity in the physical plane. At the same time, another second order pole associated to a flow having the value $-a^*$, the $*$ denoting the conjugate term, has to be placed at the point $\chi = -2 \log L = \omega$. The complex velocity and potential expressions follow:

$$\frac{dw}{d\chi} = a\wp(\chi) - a^*\wp(\chi + \omega) + ik$$

$$w(\chi) = -a\zeta(\chi) + a^*\zeta(\chi + \omega) + ik\chi.$$

The role of the constant k will be discussed later. In Figure (3.6) the streamlines of the flow field inside the fundamental area and inside a more extended region is represented, with $a = 1 + i$ and $\omega = -2 \log(0.5)$.

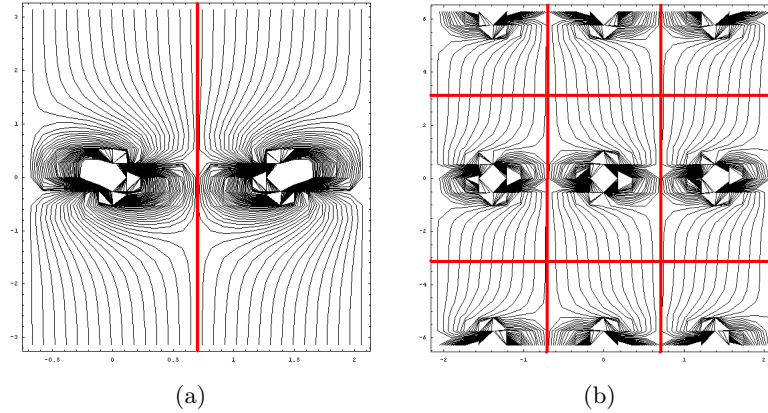


Figure 3.6. Streamline flow field inside the fundamental area (a) and inside a larger area (b) in the χ -plane: effect of second order poles.

A similar reasoning can be made for the representation of vortex singularities, the only difference being that they are of the first order type, so they are described by means of the ζ Weierstrass function. Considering a vortex singularity with intensity Γ and placed in a general point whose image in the χ -plane has the coordinate χ_j , the expressions of the corresponding complex velocity and potential are:

$$\frac{dw}{d\chi} = \frac{\Gamma}{2\pi i} \zeta(\chi - \chi_j) - \frac{\Gamma}{2\pi i} \zeta(\chi + \chi_j^* - \omega) + ik$$

$$w(\chi) = \frac{\Gamma}{2\pi i} \log \frac{\sigma(\chi - \chi_j)}{\sigma(\chi + \chi_j^* - \omega)} + ik\chi.$$

In Figure (3.7) the flow field corresponding to two vortices of intensity $\Gamma_1 = 1$ and $\Gamma_2 = -2$ placed respectively at $\chi_1 = \frac{\omega}{3} + \frac{2}{3}\pi i$ and $\chi_2 = -\frac{\omega}{4} - \frac{2}{3}\pi i$, with $\omega = -2 \log(0.5)$ is represented in the fundamental area and in a more extended area.

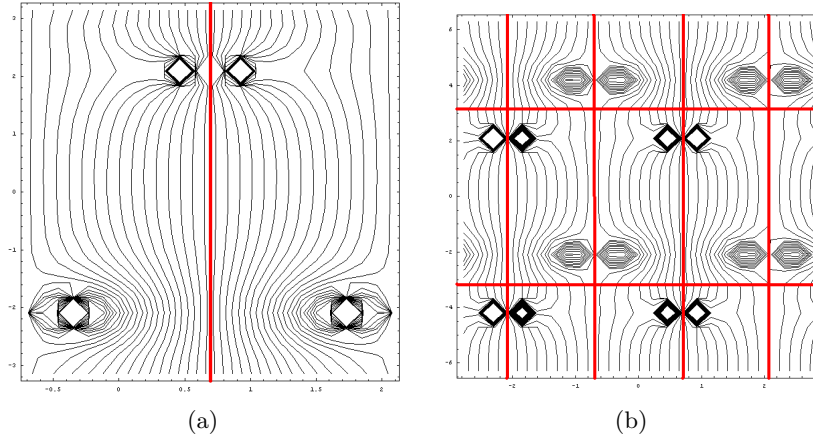


Figure 3.7. Streamline flow field inside the fundamental area (a) and inside a larger area (b) in the χ -plane: effect of first order singularities.

According to what has just been said, and coming back to the definition of the flow field when the turbine is at rest, the complex velocity $\frac{dw_1}{d\chi}$ is then expressed in this way:

$$\begin{aligned} \frac{dw_1}{d\chi} = & -Q_\infty^* \wp(\chi) + Q_\infty \wp(\chi + \omega) + \frac{1}{2\pi i} \sum_{j_u=1}^N \Gamma_{j_u} [\zeta(\chi - \chi_{j_u}) - \zeta(\chi + \chi_{j_u}^* - \omega)] \\ & + \frac{1}{2\pi i} \sum_{j_d=1}^N \Gamma_{j_d} [\zeta(\chi - \chi_{j_d}) - \zeta(\chi + \chi_{j_d}^* - \omega)] \\ & + ik. \end{aligned} \quad (3.10)$$

By integration, the complex potential follows:

$$\begin{aligned} w_1(\chi) = & Q_\infty^* \zeta(\chi) - Q_\infty \zeta(\chi + \omega) + \frac{1}{2\pi i} \sum_{j_u=1}^N \Gamma_{j_u} \log \frac{\sigma(\chi - \chi_{j_u})}{\sigma(\chi + \chi_{j_u}^* - \omega)} \\ & + \frac{1}{2\pi i} \sum_{j_d=1}^N \Gamma_{j_d} \log \frac{\sigma(\chi - \chi_{j_d})}{\sigma(\chi + \chi_{j_d}^* - \omega)} + ik\chi. \end{aligned} \quad (3.11)$$

The u and d subscripts refer to vortices shed by the upper and lower blades, respectively, N is the number of released vortex couples, $\chi_{j,u,d}$ are their locations.

We consider the parameter Q_∞ ; its value is defined by the complex velocity at infinity $q_\infty e^{-i\alpha}$ in the physical z -plane in this way:

$$\begin{aligned} \left(\frac{dw_1}{dz}\right)_{z \rightarrow \infty} &= q_\infty e^{-i\alpha} = \frac{(dw_1/d\chi)_{\chi \rightarrow 0}}{(dz/d\chi)_{\chi \rightarrow 0}} \\ \lim_{\chi \rightarrow 0} \left(\frac{dw_1}{d\chi}\right) &= \frac{Q_\infty^*}{\chi^2} \\ \lim_{\chi \rightarrow 0} \left(\frac{dz}{d\chi}\right) &= \left(\frac{dz}{d\nu}\right)_{\nu \rightarrow \infty} \cdot \left(\frac{d\nu}{d\mu}\right)_{\mu \rightarrow 1} \cdot \left(\frac{d\mu}{d\chi}\right)_{\chi \rightarrow 0} \end{aligned}$$

Then:

$$Q_\infty = 2i\eta_0 q_\infty e^{i\alpha}. \quad (3.12)$$

It should be noted that the wind velocity direction $\alpha = -\Omega t$ depends on time; so, the parameter Q_∞ defining the doublets in the transformed χ -plane also varies in time.

3.2.2 The motion of the blades

To describe the circular motion of the blades it is useful to consider the flow field in the μ -plane (see Figure (3.1)), where it is confined between two concentric circles. The complex potential w_2 should not add any singularity to the flow field and, as a consequence, its general expression can be written as a Laurent series which converges inside the annular region, that is:

$$w_2 = \sum_{n=1}^{\infty} (a_n + ib_n) (L\mu)^{n-1} + \sum_{n=1}^{\infty} (c_n + id_n) \left(\frac{\mu}{L}\right)^{-(n-1)}, \quad (3.13)$$

where the first series converges outside the interior circle, and the second series converges inside the exterior one.

The coefficients a_n , b_n , c_n , d_n are computed by the imposition of the impermeability condition, that is, imposing that the flow velocity normal to the blades be equal to the normal component of the rigid motion of the blades themselves in every point of their

contours. According to Milne-Thomson [44], we consider a generic point P on the contour of a body which rotates rigidly with the angular velocity Ω around the origin, as in Figure (3.8).

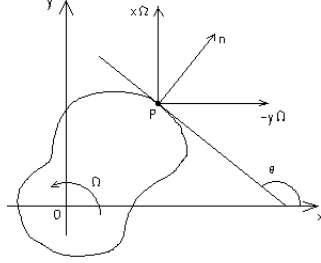


Figure 3.8. Imposition of the impermeability condition.

In the (xOy) reference system, the point P has the velocity $-y\Omega\vec{i} + x\Omega\vec{j}$; projecting it to the direction normal to the tangent to the body in P , the normal velocity V_n is obtained:

$$V_n = -\Omega y \sin \theta - \Omega x \cos \theta = -\Omega y \frac{dy}{ds} - \Omega x \frac{dx}{ds}$$

where \vec{s} is the curvilinear coordinate along the body contour, and θ is the angle between the horizontal direction and the direction of the tangent to the body in P .

On the other hand, the velocity of the flow normal to the body contour is defined by the derivative $\frac{\partial\psi}{\partial s}$. So, imposing the equality:

$$\frac{\partial\psi}{\partial s} = -\Omega y \frac{dy}{ds} - \Omega x \frac{dx}{ds},$$

and integrating:

$$\psi = -\Omega \frac{1}{2} y^2 - \Omega \frac{1}{2} x^2 + C,$$

where the arbitrary constant C can be set equal to 0 without loosing of generality.

Letting $z = z(\mu)$ be the $\mu \rightarrow z$ mapping, with $\mu = \rho e^{i\phi}$, the impermeability condition enables the definition of the streamfunction value on the contours of the circles in the μ -plane:

$$\psi_u = -\frac{1}{2}\Omega|z\left(\frac{e^{i\phi}}{L}\right)|^2 \quad , \quad \psi_d = -\frac{1}{2}\Omega|z\left(Le^{i\phi}\right)|^2, \quad (3.14)$$

where the subscripts u and d refer to the interior and exterior circles, respectively.

Now, knowing the streamfunction on the contours of the annular region, the problem is the determination of the flow field inside it, that is, the computation of the coefficients of the above series, suitably truncated. The following two relationships can be derived:

$$\psi_u = \sum_{n=1}^N (A_n \cos [(n-1)\phi] + B_n \sin [(n-1)\phi]) \quad (3.15)$$

$$\psi_d = \sum_{n=1}^N (C_n \cos [(n-1)\phi] + D_n \sin [(n-1)\phi]) \quad (3.16)$$

where:

$$A_n = b_n L^{2n-2} + d_n$$

$$B_n = a_n L^{2n-2} - c_n$$

$$C_n = b_n + d_n L^{2n-2}$$

$$D_n = a_n - c_n L^{2n-2}.$$

The coefficients A_n, B_n, C_n, D_n are computed by means of the *Fast Fourier Transform* (FFT). The derivation of a_n, b_n, c_n, d_n is then immediate:

$$\begin{aligned} a_n &= \frac{B_n - D_n/L^{2n-2}}{E_n} \\ b_n &= \frac{A_n - C_n/L^{2n-2}}{E_n} \\ C_n &= \frac{B_n/L^{2n-2} - D_n}{E_n} \\ D_n &= \frac{C_n - A_n/L^{2n-2}}{E_n}. \end{aligned} \quad (3.17)$$

3.2.3 Kutta condition

The strengths $\gamma_{j_{u,d}}$ of the shed vortices are determined by enforcing the Kutta condition. If the blades are at rest, this means that the complex velocity is imposed to be zero at the trailing edges on their contours. For moving bodies the relative flow field is considered;

since, in the present case, it is rotational, resulting from the subtraction of the angular velocity of the blades from the absolute flow velocity, the relative complex potential cannot be defined. The requirement being that the tangential relative velocity is non-singular at the trailing edges, the stream function ψ_{REL} of the relative motion is used. We consider a point P on the blade contours in the z -plane, as in Figure (3.9).

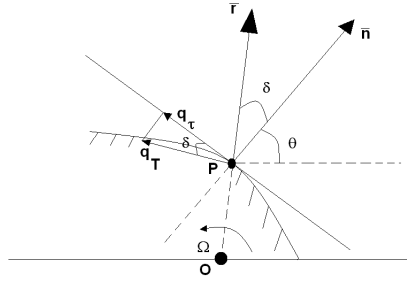


Figure 3.9. Kutta condition: computation of the relative velocity on the blade contours.

If V_τ represents the tangential velocity to the blades in the point P , then:

$$V_{\tau REL} = V_{\tau ABS} - q_\tau \quad (3.18)$$

where:

•

$$V_{\tau REL} = \frac{\partial \psi_{REL}}{\partial n},$$

\vec{n} being the outward normal to the body direction;

•

$$q_\tau = q_T \cos \delta = \Omega |z| \cos \delta,$$

δ being the angle between the radial \vec{r} and \vec{n} directions;

•

$$\begin{cases} V_{\tau ABS} = -\Im \left[\frac{dw_{ABS}}{dz} e^{i\theta} \right] = -\Im \left[\frac{dw_{ABS}}{d\chi} \frac{d\chi}{dz} e^{i\theta} \right] \\ \frac{dz}{d\chi} = \left| \frac{dz}{d\chi} \right| e^{i\tau}, \tau = \theta - \beta \end{cases}$$

θ being the angle between \vec{n} and the horizontal directions, and β the angle between the real axis and the direction normal to the left side of the rectangle in the χ -plane.

z_{T_u} and z_{T_d} being the coordinates of the trailing edges of the blades, the following expression is obtained:

$$\lim_{z \rightarrow z_{T_u}, z_{T_d}} \frac{\partial \psi_{REL}}{\partial n} = \lim_{z \rightarrow z_{T_u}, z_{T_d}} \left[\Im \left(\frac{dw_{ABS}}{d\chi} \right) \cdot \left| \frac{d\chi}{dz} \right| + \Omega |z| \cos \delta \right] \quad (3.19)$$

Since the derivative $\frac{d\chi}{dz} \rightarrow \infty$ at the trailing edges, and the second term in the right hand side expression tends to a finite value, the Kutta condition is expressed by the following equations:

$$\Im \left(\frac{dw}{d\chi} \right)_{\chi=\chi_{T_u}} = 0 \quad (3.20)$$

$$\Im \left(\frac{dw}{d\chi} \right)_{\chi=\chi_{T_d}} = 0 \quad (3.21)$$

where χ_{T_u} and χ_{T_d} are the images in the χ -plane of the trailing edges in the physical plane.

3.2.4 The meaning of the constant K

In a simply-connected domain the imposition of the Kutta condition is sufficient to completely define the flow field. But in a doubly-connected domain, like the one here studied, this is not true, that is, the imposition of the Kutta condition at the trailing edge of the two profiles doesn't enable a unique description of the flow field, as it can be noted by the presence of the real constant K in the expressions (3.10) and (3.11) of the complex velocity and potential, respectively. According to [70], two elliptic functions with the same poles can only differ by a constant. Thus the flow field around the blades is unique only once K is defined. But, how to define it? This term represents the mean by which the Kelvin theorem enters into the definition of the flow field: we could say that this is the direction into which the entire model here developed improves on the definition of the vortex motion in a doubly connected domain.

The Kelvin Theorem states that, in an inviscid and barotropic flow with conservative body forces, the circulation along a closed curve moving with the fluid remains constant in time, that is:

$$\frac{d}{dt} \left(\oint \vec{u} d\vec{l} \right) = 0$$

where the vector \vec{u} denotes the velocity field, and the integral is taken along a generic closed curve.

According to this, the value $K(t)$ is defined at each time step. Let us assume that, at the initial time, the turbine and the flow are at rest and, as a consequence, the total circulation and the circulation around each blade are null. During the motion, the sum of the bound and shed circulations should remain null for each blade. Let γ_u, γ_d denote the circulations past the upper and lower blades, respectively; then $\Gamma = (\gamma_u + \gamma_d)$, that is, Γ is the opposite of the total circulation past the two airfoils, and also $\gamma_u = -\sum \gamma_{j_u}$, $\gamma_d = -\sum \gamma_{j_d}$.

With reference to Figure (3.5), by definition:

$$\Re \oint \frac{dw}{d\chi} d\chi = \Gamma = -(w_A - w_{A'}) - (w_{B'} - w_B) = \sum_{j_u=1, j_d=1}^N (\gamma_{j_u} + \gamma_{j_d})$$

and:

$$\gamma_u = (w_A - w_{A'}), \quad \gamma_d = (w_{B'} - w_B).$$

It follows that the function $K(t)$ is established by enforcing either:

$$(w_A - w_{A'}) = - \sum_{j_u=1}^N \gamma_{j_u} \tag{3.22}$$

or

$$(w_{B'} - w_B) = - \sum_{j_d=1}^N \gamma_{j_d}. \tag{3.23}$$

For this purpose it is convenient to use the Equation (3.22) in order to manage in a simpler way the branch cuts which connect points $(\chi_{j_u, d})$ and $(\omega - \chi_{j_u, d}^*)$. Exploiting the quasi- periodicity properties of the ζ and σ Weierstrass functions [70]:

$$K = \frac{1}{2\pi} \cdot \left\{ \sum_{j_u=1}^N \right. \\
 + Q_\infty^* \left[\zeta \left(-\frac{\omega}{2} + i\pi \right) - \zeta \left(-\frac{\omega}{2} - i\pi \right) \right] - Q_\infty \left[\zeta \left(\frac{\omega}{2} + i\pi \right) - \zeta \left(\frac{\omega}{2} - i\pi \right) \right] \\
 + \frac{1}{2\pi i} \sum_{j_u=1}^N \gamma_{j_u} \log \left[\frac{\sigma \left(-\frac{\omega}{2} + i\pi - \chi_{j_u} \right)}{\sigma \left(-\frac{3}{2}\omega + i\pi + \chi_{j_u}^* \right)} \cdot \frac{\sigma \left(-\frac{3}{2}\omega - i\pi + \chi_{j_u}^* \right)}{\sigma \left(-\frac{\omega}{2} - i\pi - \chi_{j_u} \right)} \right] \\
 + \frac{1}{2\pi i} \sum_{j_d=1}^N \gamma_{j_d} \log \left[\frac{\sigma \left(-\frac{\omega}{2} + i\pi - \chi_{j_d} \right)}{\sigma \left(-\frac{3}{2}\omega + i\pi + \chi_{j_d}^* \right)} \cdot \frac{\sigma \left(-\frac{3}{2}\omega - i\pi + \chi_{j_d}^* \right)}{\sigma \left(-\frac{\omega}{2} - i\pi - \chi_{j_d} \right)} \right] \left. \right\} \\
 \left\{ \begin{array}{l} \zeta \left(-\frac{\omega}{2} + i\pi \right) - \zeta \left(-\frac{\omega}{2} - i\pi \right) = 2\zeta(i\pi) \\ \zeta \left(\frac{\omega}{2} + i\pi \right) - \zeta \left(\frac{\omega}{2} - i\pi \right) = 2\zeta(i\pi) \end{array} \right. \\
 \left\{ \begin{array}{l} \frac{\sigma \left(-\frac{\omega}{2} + i\pi - \chi_{j_u} \right)}{\sigma \left(-\frac{\omega}{2} - i\pi - \chi_{j_u} \right)} = -e^{2\eta' \left(-\frac{\omega}{2} - \chi_{j_u} \right)} \\ \frac{\sigma \left(-\frac{3}{2}\omega - i\pi + \chi_{j_u}^* \right)}{\sigma \left(-\frac{3}{2}\omega + i\pi + \chi_{j_u}^* \right)} = -e^{-2\eta' \left(-\frac{3}{2}\omega + \chi_{j_u}^* \right)}, \quad \eta' = \zeta(i\pi) \end{array} \right.$$

Then, finally, the expression (3.24) is obtained:

$$K = \frac{1}{2\pi} \cdot \left\{ \sum_{j_u=1}^N \gamma_{j_u} - 4i\eta' \Im(Q_\infty) + \right. \\
 \left. + \frac{2\eta'}{i\pi} \cdot \left[\sum_{j_u=1}^N \gamma_{j_u} \left(\frac{\omega}{2} - \Re(\chi_{j_u}) \right) \sum_{j_d=1}^N \gamma_{j_d} \left(\frac{\omega}{2} - \Re(\chi_{j_d}) \right) \right] \right\} \quad (3.24)$$

As it can be seen, Equation (3.24) defines the function $K(t)$ through the dependence, on time, of the vortex locations $\chi_{j_{u,d}}(t)$ during their motion, and also of the direction of the flow velocity at infinity with respect to the reference system rotating at the constant angular velocity Ω . In addition, in the determination of $K(t)$, the terms of the complex potential w_2 are not considered because, on the χ -plane, w_2 is periodic with the period $2\pi i = 2\omega'$.

3.2.5 Instantaneous absolute and relative flow fields

The complex potential $w = w_1 + w_2$ is now completely defined. Before describing how to compute its evolution in time, we represent the instantaneous absolute and relative flow fields after the first time steps, when the turbine is experiencing an impulsive start.

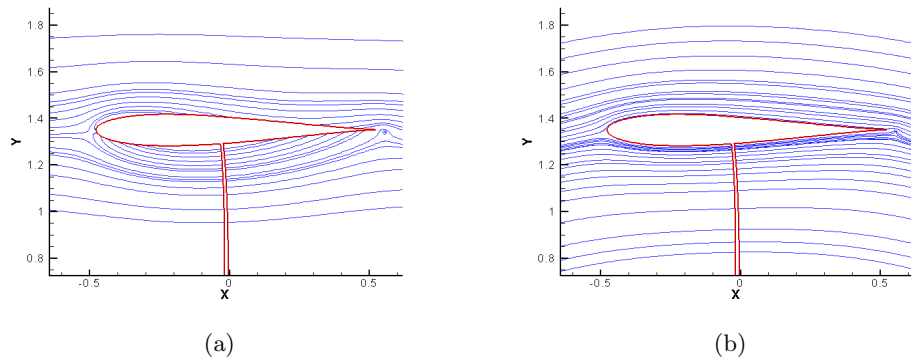


Figure 3.10. Streamline distribution of the absolute (a) and relative(b) flow fields around the upper blade.

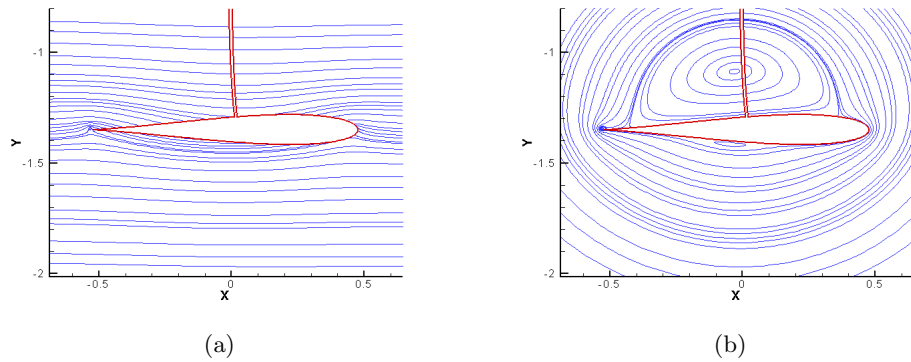


Figure 3.11. Streamline distribution of the absolute (a) and relative(b) flow fields around the lower blade.

In Figures (3.10) and (3.11) the streamlines are shown around the upper and lower blades, respectively. As expected, in the absolute flow field the streamlines don't take a constant value along the body contours entering into them. Concerning the relative flow field, it has to be noticed that in Figure (3.11) (b) a sort of bubble is present on the upper surface of the blade. This is because, in the center of this structure, the tangential

velocity due to the rigid circular motion of the blades and the wind speed are equal, so the relative velocity becomes zero. The position where this happens is a function of the wind/blade-speed ratio $q_\infty/\Omega R$. In all the above images a little vortical structure can also be observed near the trailing edge of the blades: the wake is being born and developing detaching from the profiles.

3.3 Evolution in time of the flow field

The basic idea of the method here implemented is to integrate in time the vortex locations on the transformed χ -plane and then to map them on the physical z -plane. The resulting algorithm at the generic time step is structured as follows:

1. definition of the complex potential w , N_v being the total number of singularities in the flow field:

$$\begin{aligned}
 w &= Q_\infty^* \zeta(\chi) - Q_\infty \zeta(\chi + \omega) + iK\chi + \\
 &+ \frac{1}{2i\pi} \sum_{j=1}^{N_v-2} \gamma_j \log \frac{\sigma(\chi - \chi_j)}{\sigma(\chi + \chi_j^* - \omega)} + \\
 &+ \frac{1}{2i\pi} \gamma_u \log \frac{\sigma(\chi - \chi_{v_u})}{\sigma(\chi + \chi_{v_u}^* - \omega)} + \frac{1}{2i\pi} \gamma_d \log \frac{\sigma(\chi - \chi_{v_d})}{\sigma(\chi + \chi_{v_d}^* - \omega)} + \\
 &+ \sum_{i=1}^N (a_n + ib_n) (Le^\chi)^{n-1} + \sum_{i=1}^N (c_n + id_n) (e^\chi/L)^{-(n-1)} \quad (3.25)
 \end{aligned}$$

The terms γ_u , γ_d , representing the intensities of the newly arisen vortices shed from the upper and lower blades, respectively, are put in evidence with their corresponding complex potential. χ_{v_u} and χ_{v_d} are the coordinates of the points where the vortices are released: assuming c as the reference length, with c being the chord of both the blades, the released locations in z -plane, that is, z_{v_u} , z_{v_d} are set downstream from the trailing edges at the distance $d = 0.01$, which is in the range of the values recommended in literature. The two Laurent series in the above expression (3.25), representing the part of the complex potential due to the motion of the blades, are equal to the previously defined term w_2 , expressed in the χ -plane; to make the reading of the expressions not so heavy, they will be replaced by $w_2(\chi)$.

2. to fully define w , the terms γ_u , γ_d and K have to be computed; imposing the Kutta condition on the coordinates χ_{T_u} and χ_{T_d} of the trailing edges of the blades, and keeping to the Kelvin Theorem along a closed curve surrounding the upper blade, the following system is obtained to be solved:

$$\begin{aligned}
 & \Im \left[\frac{1}{2i\pi} [\zeta(\chi_{T_u} - \chi_{v_u}) - \zeta(\chi_{T_u} + \chi_{v_u}^* - \omega)] \right] \gamma_u + \\
 & + \Im \left[\frac{1}{2i\pi} [\zeta(\chi_{T_u} - \chi_{v_d}) - \zeta(\chi_{T_u} + \chi_{v_d}^* - \omega)] \right] \gamma_d + K = \\
 & = \Im [Q_\infty^* \wp(\chi_{T_u}) - Q_\infty \wp(\chi_{T_u} + \omega)] - \\
 & \Im \left[\frac{1}{2i\pi} \sum_{j=1}^{N_v-2} \gamma_j [\zeta(\chi_{T_u} - \chi_j) - \zeta(\chi_{T_u} + \chi_j^* - \omega)] \right] - \\
 & \Im \left[\left(\frac{dw_2}{d\chi} \right)_{\chi_{T_u}} \right]
 \end{aligned} \tag{3.26}$$

$$\begin{aligned}
 & \Im \left[\frac{1}{2i\pi} [\zeta(\chi_{T_d} - \chi_{v_u}) - \zeta(\chi_{T_d} + \chi_{v_u}^* - \omega)] \right] \gamma_u + \\
 & + \Im \left[\frac{1}{2i\pi} [\zeta(\chi_{T_d} - \chi_{v_d}) - \zeta(\chi_{T_d} + \chi_{v_d}^* - \omega)] \right] \gamma_d + K = \\
 & = \Im [Q_\infty^* \wp(\chi_{T_d}) - Q_\infty \wp(\chi_{T_d} + \omega)] - \\
 & \Im \left[\frac{1}{2i\pi} \sum_{j=1}^{N_v-2} \gamma_j [\zeta(\chi_{T_d} - \chi_j) - \zeta(\chi_{T_d} + \chi_j^* - \omega)] \right] - \\
 & \Im \left[\left(\frac{dw_2}{d\chi} \right)_{\chi_{T_d}} \right]
 \end{aligned} \tag{3.27}$$

$$\begin{aligned}
 & \left[\frac{\eta'}{i\pi} (2\Re(\chi_{v_u}) - \omega) - 1 \right] \gamma_u + \frac{\eta'}{i\pi} (2\Re(\chi_{v_d}) - \omega) \gamma_d + 2K\pi = \\
 & -4i\eta' \Im(Q_\infty) - \frac{\eta'}{i\pi} \sum_{j=1}^{N_v-2} \gamma_j [2\Re(\chi_j) - \omega] + \sum_{j_P=1}^{N_P-1} \gamma_{j_P}, \quad \eta' = \zeta(i\pi) \tag{3.28}
 \end{aligned}$$

N_P is the number of vortices shed only by the upper blade; one of them has the unknown circulation. The vortex release interval is set at $\Delta t_r = \beta \Delta t$, β being 4 to

make not too heavy the computation. When the vortex release doesn't take place, only the variable K has to be defined by means of the following expression:

$$K = \frac{1}{2\pi} \left[-4i\eta' \Im(Q_\infty) - \frac{\eta'}{i\pi} \sum_{j=1}^{N_v-2} \gamma_j [2\Re(\chi_j) - \omega] + \sum_{jP=1}^{N_P} \gamma_{jP} \right] \quad (3.29)$$

What is now described relates to each single point vortex placed in the coordinate χ_s in the flow field. The relative velocity $\left(\frac{d\chi}{dt}\right)_{REL_{\chi_s}}$ having to be computed, the usual following relation is used:

$$\left(\frac{d\chi}{dt}\right)_{REL_{\chi_s}} = \left(\frac{d\chi}{dt}\right)_{ABS_{\chi_s}} - \left(\frac{d\chi}{dt}\right)_{RM_{\chi_s}} \quad (3.30)$$

where:

- $\left(\frac{d\chi}{dt}\right)_{ABS_{\chi_s}}$ = vortex velocity in the absolute fix reference system;
- $\left(\frac{d\chi}{dt}\right)_{RM_{\chi_s}}$ = velocity due only to the rigid motion of the relative system.

So the algorithm continues in this way:

3. the computation of the absolute velocity of the vortex at χ_s starts from the definition of the velocity $\chi_s'^*$ that a free vortex should possess through advection on the χ -plane, that is:

$$\begin{aligned} \chi_s'^* &= \lim_{\chi \rightarrow \chi_s} \left[\frac{dw}{d\chi} - \frac{\gamma_s}{2i\pi} \zeta(\chi - \chi_s) \right] = \\ &= -Q_\infty^* \wp(\chi_s) + Q_\infty \wp(\chi_s + \omega) + \\ &+ \frac{1}{2i\pi} \sum_{j=1, j \neq s}^{N_v} \gamma_j [\zeta(\chi_s - \chi_j) - \zeta(\chi_s + \chi_j^* - \omega)] - \\ &- \frac{1}{2i\pi} \gamma_s \zeta(\chi_s + \chi_s^* - \omega) + iK + \left(\frac{dw_2}{d\chi}\right)_{\chi_s} \end{aligned} \quad (3.31)$$

According to the Routh rule ([60], [62]), the velocity in the physical z -plane is obtained in this way:

$$\left(\frac{dz}{dt}\right)_{z_s}^* = \left(\chi_s'^* - \frac{\gamma_s}{4i\pi} \frac{(d^2z/d\chi^2)_{\chi_s}}{(dz/d\chi)_{\chi_s}}\right) / \left(\frac{dz}{d\chi}\right)_{\chi_s} \quad (3.32)$$

where:

$$\frac{dz}{d\chi} = \frac{dz}{dD} \cdot \frac{dD}{d\nu} \cdot \frac{d\nu}{d\mu} \cdot \frac{d\mu}{d\chi}, \quad D = \left(\frac{\nu^2 - \nu_T^2}{\nu^2 - \nu_T^2}\right)^\tau$$

and:

$$\begin{aligned} \frac{d^2z}{d\chi^2} &= \frac{d^2z}{dD^2} \cdot \left(\frac{dD}{d\nu} \cdot \frac{d\nu}{d\mu} \cdot \frac{d\mu}{d\chi}\right)^2 + \frac{dz}{dD} \cdot \frac{d^2D}{d\nu^2} \cdot \left(\frac{d\nu}{d\mu} \cdot \frac{d\mu}{d\chi}\right)^2 + \\ &+ \frac{dz}{dD} \cdot \frac{dD}{d\nu} \cdot \frac{d^2\nu}{d\mu^2} \cdot \left(\frac{d\mu}{d\chi}\right)^2 + \frac{dz}{dD} \cdot \frac{dD}{d\nu} \cdot \frac{d\nu}{d\mu} \cdot \frac{d^2\mu}{d\chi^2} \end{aligned}$$

Finally, to reduce to the same velocity in the transformed χ -plane, Equation (3.33) is applied:

$$\left(\frac{d\chi}{dt}\right)^* = \frac{\chi_s'^* - \frac{\gamma_s}{4i\pi} \frac{d^2z/d\chi^2}{dz/d\chi}}{|dz/d\chi|^2} \quad (3.33)$$

because:

$$\left(\frac{d\chi}{dt}\right)^* = \frac{(dz/dt)^*}{(dz/d\chi)^*}.$$

4. As concerns the term $\left(\frac{d\chi}{dt}\right)_{RM_{\chi_s}}$, the rigid motion consists of a rotation of the system around the origin with the angular velocity Ω ; the following expressions are immediately obtained:

$$\begin{cases} \left(\frac{dz}{dt}\right)_{RM_{z_s}} = i\Omega z_s & \text{in the } z\text{-plane} \\ \left(\frac{d\chi}{dt}\right)_{RM_{\chi_s}} = \left(\frac{dz}{dt}\right)_{RM_{z_s}} / \left(\frac{dz}{d\chi}\right)_{\chi_s} & \text{in the } \chi\text{-plane} \end{cases}$$

5. The relative velocity having been completely defined, the next step is its integration in time; the second-order *Adams-Bashforth* scheme is adopted, resulting in this expression:

$$\chi_s^{n+1} = \chi_s^n + \frac{\Delta t}{2} \cdot \left[3 \left(\frac{d\chi}{dt} \right)_{\chi_s}^n - \left(\frac{d\chi}{dt} \right)_{\chi_s}^{n-1} \right] \quad (3.34)$$

where n is the index of the time step and, assuming q_∞ as the reference velocity and c as the reference length, as already said, Δt is taken equal to 10^{-3} .

6. Finally, using the mapping function $z = z(\chi)$, the new relative position χ_s^{n+1} of the s -th vortex is transformed into its image in the z -plane, and then, rotating it of the angle Ωt , the absolute physical position of the same vortex is found at the time instant t .

The same procedure has to be followed for all the N_v vortices, and at the end the process restarts in the same way from the point (1) above.

3.4 Numerical example

To give an example of the evolution of a flow field past a two-blade Darrieus turbine a computation is performed for a turbine with the chord/radius ratio $c/R = 0.74$ and with the wind/blade-speed ratio $q_\infty/\Omega R = 0.88$. The geometry is obtained adopting the following values for the parameters defining the conformal mapping: $L = 9.9$, $\eta_0 = 4.9$, $\nu_T = 1 + 5i$, $\nu_N = -0.8 + 5i$, $\epsilon = 5^\circ$. The computation was deformed by means of a parallel implementation (MPI technique) because of the large amount of operations needed, which increases at the enormous rate of $O(N^2)$, with N being the number of point vortices in the flow field, every singularity influencing the development of all the others.

A snapshot of the wakes issued by the blades (at time instant $t = 28.5$) is shown in Figure (3.12): the blue points correspond to the vortex singularities with negative (clockwise) circulation, and the red ones to those with positive circulation.

The wind being directed from left to right, the wakes are pushed to the right far from the rotating blades. It can be noted the complexity of the resulting flow field, the wakes interacting between themselves after being shed by the trailing edges.

Figure (3.13) shows the time history of the bound circulations γ_u , γ_d around the upper and lower blades, respectively. After the impulsive start, a quasi-regular development

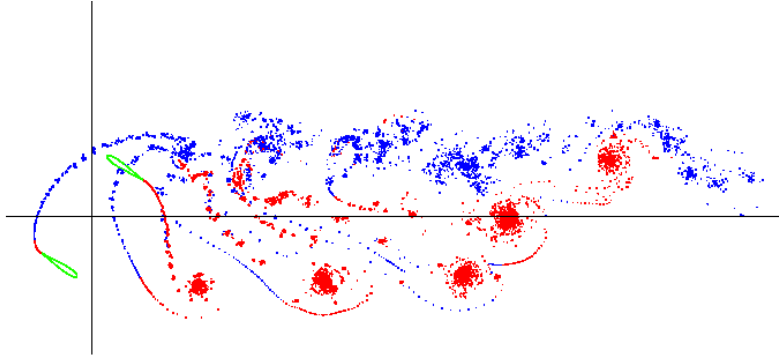


Figure 3.12. Wake visualisation past the two-blade Darrieus turbine at time instant $t = 28.5$; in the flow field 12400 vortex singularities are present.

can be observed, a disturbance occurring only when the blades pass through the wake previously shed.

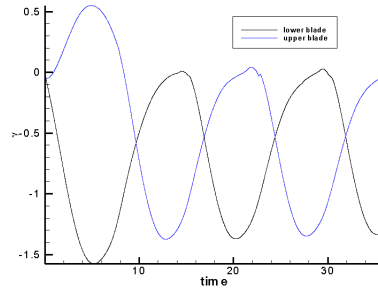


Figure 3.13. Time history of the bound circulations around the upper (blue) and lower (black) blades.

The numerical result here presented is only an example of the application of what is said above. We want to describe the dynamics of a complicated unsteady flow field, where the unsteadiness is due both to the structures generated into the flow and to the motion of the bodies. The considered domain is doubly-connected. By means of the built model, the separation of the flow is imposed at the trailing edge of the two blades, so the Kutta condition must be imposed at these points. But, unlike the simply-connected case, where the Kutta condition on the trailing edge of a profile completely defines the flow field around it, here the two resulting conditions we have seen to be not sufficient to determine the circulations around the blades, keeping in mind that they vary in time because of the

unsteadiness of the environment. In the model, the flow field in the computational domain is described by means of elliptic functions, about which a property states that the same distribution of singularities can be defined by an infinite number of elliptic functions unless an arbitrary constant is fixed. And it is by means of this constant that the third condition necessary to uniquely define the values of the circulations is obtained. In fact, imposing the Kelvin theorem, that is, that the circulation around each blade must be equal to the opposite value of the total summation of the shed vortex points intensities corresponding to the same blade, the value of this variable ($K(t)$ in the above discussion) is determined.

Chapter 4

A suggestion for a better design of a VAWT

In the previous chapter an analytical-numerical model was built to describe the unsteady, inviscid rotational flow field past a classical Darrieus wind turbine. The main problem was the definition of the vortex motion past the blades of the VAWT, that is, past bodies with non-null varying circulation in a doubly connected domain. The flow field is transformed, by conformal mapping, into a rectangular domain where the complex velocity is expressed by an elliptic function, which, according to the theory, is unique once an additive function $K(t)$ is defined. This function is established by the Kelvin Theorem, that is, by the physical requirement that the sum of the bound and shed circulations past each body remains constant. All that has been defined and obtained for a Darrieus turbine with classical blades will now be used for the study and analysis of a VAWT whose blades have vortex trapping cavities. The flow is always assumed as incompressible and inviscid, with the shed vorticity modelled by vortex singularities; conformal mapping and a vortex method remain the tools used to describe the evolution of the unsteady flow field.

But, before going on, why consider profiles with this unusual shape? The main problem with the Darrieus architecture is the complicated unsteady flow phenomena occurring during its working cycle. During each revolution, the blades of traditional Darrieus turbine undergo a highly unsteady relative fluid motion with large oscillation of the incidence. Dynamic stall can occur and the consequent uncontrolled flow detachment and vortex

shedding result in high drag and low efficiency.

Recent developments offer a tool to design blades with innovative vortex trapping cavities. Trapping vortices is a technology for preventing vortex-shedding in flows past bluff bodies. Vortices forming near bluff bodies tend to be shed downstream. If the vortex is kept near the body at all times, it is called *trapped*. In particular vortices can be trapped in vortex cells that are special cavities in the airfoil. A trapped vortex can be used to let the flow overcome the regions of unfavorable pressure gradient, controlling its separation. In practice, the captured vortices result in being highly unstable to small perturbations, and if they are slightly displaced from their equilibrium position they will not come back. In the literature several works are dedicated to the active stabilization of such flows, for example [81] and [27]. All these efforts are made to obtain the stabilization of the trapped vortices, with the principal aim of controlling the stall of thick aircraft wings; in fact, the concept is old ([57]): trapped vortices, energizing the external flow field, control its separation from the profile at high angles of attack (see Figure (4.1)) reducing the drag and avoiding the rising of a deleterious vortex shedding phenomena.

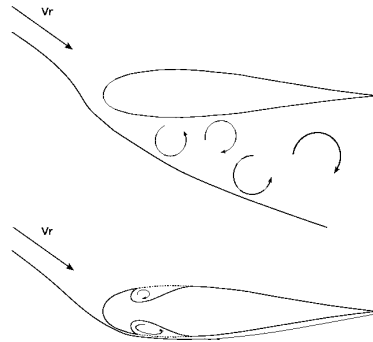


Figure 4.1. Advantage illustration of the vortex trapping cavity solution.

In the present work the idea is extended to unconventional lift VAWTs: one of the major drawback of a Darrieus-type wind turbine being the vortex-shedding phenomena, we have thought that the trapping vortex technology can be employed in order to avoid or at least reduce them. By means of properly designed cavities able to trap a vortex stabilizing the external flow, the turbine performance can be improved. The flow structure with trapped vortices being preserved during the entire working cycle, also at stall conditions, the erratic unsteadiness of the separation points will be avoided. Moreover, when

the incidence experienced by the blades is not zero, the vortices trapped in the cavities symmetrical with respect to the profile chord have not the same strength, but they change it in order to adapt the camber of the airfoils in favour of the incoming flow, acting as adaptive passive devices.

Here the goal is to show that what is said above is confirmed by the capacity of the cavity-provided blades to trap vortices, with the consequent certainty that this could be a useful technology to be deepened. We have to keep in mind that the considered model is inviscid, so all the secondary separations along the blades and into their cavities are not considered; in this way one of the main causes of the detachment is not taken into account. However the results can be considered of good relevance in the case in which the rise of the instabilities are characterized by large relaxation times, which means that the time the detachment takes to grow up is relatively short in respect to the time the turbine takes to make a working cycle. So, the present study would be only a preliminary analysis of the applicability of this technology; but, even if results are obtained by means of an inviscid model, for a first approximation they can be considered significant.

In the framework of the model developed in the previous chapter, the proposed configuration is studied designing a new conformal mapping and taking into account a greater number of points on the profile where the flow is forced to separate, that is, apart from the trailing edges, the sharp edges ahead of the cavities. Good confirmations of what is presupposed above are obtained.

4.1 Conformal Mapping

In the same spirit of the study previously carried out for a classical Darrieus turbine, the mapping problem is simplified in order to speed up the flow computation with the minimal purpose of illustrating the vortex trapping mechanism. As in Section (3.1), a closed form mapping is devised that generates a couple of Kármán-Trefftz-like airfoils from a circular ring.

The mapping sequence is shown in Figure (4.2). Comparing it with the mapping chain defined in Section (3.1), the new λ -plane is introduced to generate the two cavities in each blade profile. The following function is used to map the two circles of the ν -plane onto the two figures of the λ -plane:

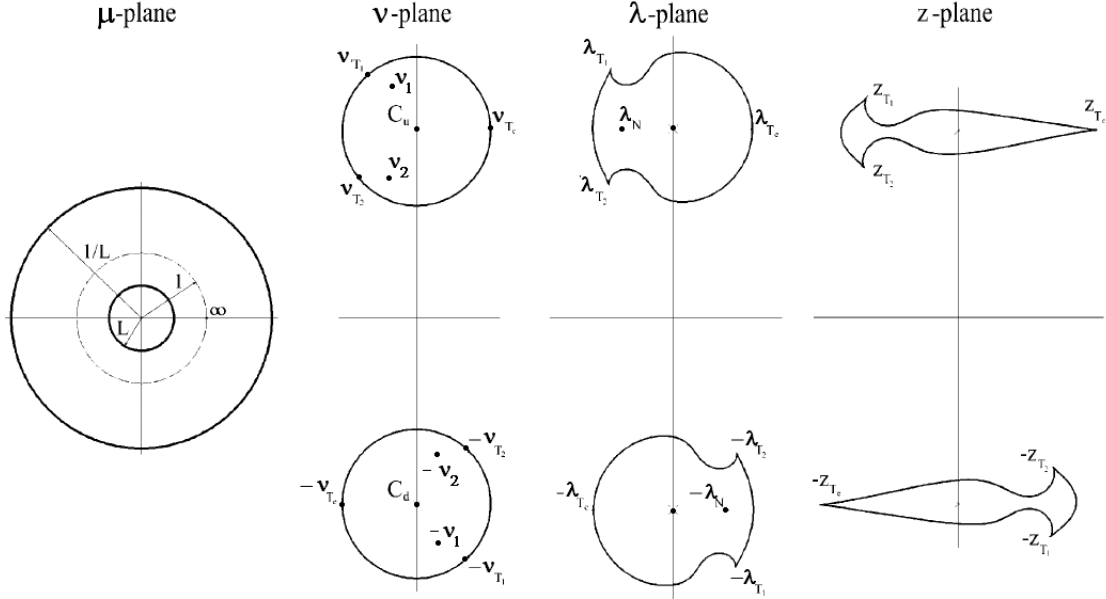


Figure 4.2. Mapping sequence: from μ -plane to the physical z -plane.

$$\lambda = \left[\nu^2 + \frac{a}{\nu^2 - \nu_1^2} + \frac{b}{\nu^2 - \nu_2^2} + \lambda_0 \right]^{\frac{1}{2}}. \quad (4.1)$$

We consider only the upper circle C_u in the ν -plane (the corresponding points can be immediately obtained for the lower circle C_d): ν_{T_1} , ν_{T_2} are the images on the circle of the cusped edges of the cavities; ν_1 , ν_2 are points inside the circle located in the same quadrant of ν_{T_1} and ν_{T_2} , respectively; ν_{T_e} is the image of the airfoil trailing edge.

The term λ_0 is defined superpositioning the origins of the λ - and ν -planes:

$$\lambda_0 = \frac{a}{\nu_1^2} + \frac{b}{\nu_2^2}.$$

For the unknowns a , b parameters, the points ν_{T_1} and ν_{T_2} on the circle contour are imposed to be singular, the following system being defined:

$$\begin{cases} \left(\frac{d\lambda}{d\nu} \right)_{\nu_{T_1}} = 0 \\ \left(\frac{d\lambda}{d\nu} \right)_{\nu_{T_2}} = 0 \end{cases}$$

The resulting profiles in the λ -plane can be superimposed over one another by a π rotation.

The mapping functions from μ - and λ -planes to ν - and z -planes, respectively, not changing with respect to the ones above built, the whole transformation depends on the choice of the parameters $\eta_0, \nu_1, \nu_2, \nu_{T_1}, \nu_{T_2}, \lambda_N$ and ε , that is, it depends on twelve real parameters. It is not possible to obtain blades which are symmetrical to their axis, but the choice of the above parameters has been made in order to obtain the most symmetry as possible.

4.2 The complex potential and its evolution in time

As for the case without cavities, the complex potential w is defined as the sum of two terms, w_1 and w_2 : the former is built in the χ -plane considering the turbine at rest, and the latter is built in the μ -plane considering the motion of the turbine. The resulting expressions are Equations (3.10) for the complex velocity and (3.11) for the complex potential, the only difference being the number of vortex singularities in the flow fields, which is three times that for blades without cavities. Their intensities and the function $K(t)$ are computed imposing the Kutta condition at the six cusped edges $\chi_{T_{eu}}, \chi_{T_{1u}}, \chi_{T_{2u}}$ for the upper blade, and $\chi_{T_{ed}}, \chi_{T_{1d}}, \chi_{T_{2d}}$ for the lower blade, and, according to the Kelvin Theorem, imposing that the circulation along a closed curve around the upper blade remain constant. So the system to be solved is the following:

$$\left\{ \begin{array}{l} \left(\frac{dw}{d\chi} \right)_{\chi_{T_{eu}}} = 0, \quad \left(\frac{dw}{d\chi} \right)_{\chi_{T_{ed}}} = 0 \\ \left(\frac{dw}{d\chi} \right)_{\chi_{T_{1u}}} = 0, \quad \left(\frac{dw}{d\chi} \right)_{\chi_{T_{1d}}} = 0 \\ \left(\frac{dw}{d\chi} \right)_{\chi_{T_{2u}}} = 0, \quad \left(\frac{dw}{d\chi} \right)_{\chi_{T_{2d}}} = 0 \\ \oint_{\partial P} \vec{u} d\vec{l} = -(\sum \gamma_{T_{eu}} + \sum \gamma_{T_{1u}} + \sum \gamma_{T_{2u}}) \end{array} \right.$$

where $\gamma_{T_{eu}}, \gamma_{T_{1u}}, \gamma_{T_{2u}}$ are the intensities of the vortex singularities shed by the trailing edge and by the cavity cusped edges, respectively, and the closed integral is computed along the closed line ∂P surrounding the upper blade.

The evolution in time of the flow field is described in the same way as for blades without cavities, by means of the same algorithm (see Section (3.3))

4.3 Numerical example

As numerical confirmation of what has been said above about the vortex trapping technology applied to a VAWT, the flow field is considered past a turbine with a blade-chord / turbine-radius ratio $c/R = 1/2$ and with a wind-speed / turbine-speed ratio $q_\infty/\Omega R = 1/10$. The blade geometry is built using the following values: $\eta_0 = 2.1$, $\nu_{T_1} = \nu_c + \rho_c e^{i2.22}$, $\nu_{T_2} = \nu_c + \rho_c e^{i4.05}$, $\nu_1 = \nu_c + 0.937\rho_c e^{i2.1}$, $\nu_2 = \nu_c + 0.937\rho_c e^{i4.18}$, $\nu_N = \nu_c + 0.65\rho_c e^{i\pi}$, $\varepsilon = 5deg$.

The motion of the blades starts impulsively; in Figure (4.3) some snapshots of the initial flow fields are shown. By means of the streamline evolution, the generation is described of the trapped vortex structures inside the cavities of the upper blades (a similar development is observable for the lower blade). The flow is forced to separate at the edge of the cavities; then a vortical structure grows-up and develops filling-up the cavities; in the end the flow reattaches to the profile on the smooth end of the cavities. From this moment, there will be always a vortical structure in the cavities, which, energizing the external flow, will stabilize its behavior.

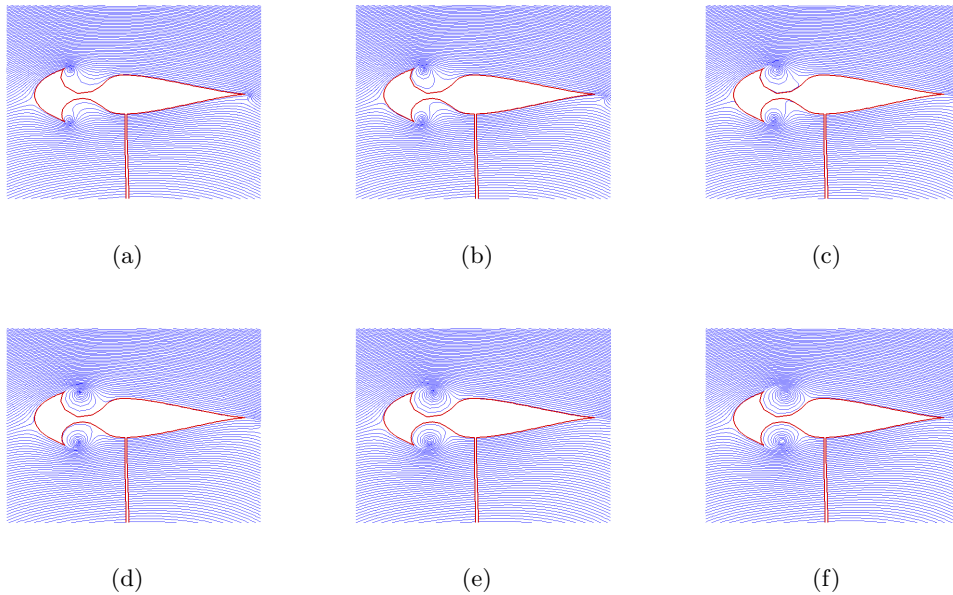


Figure 4.3. Generation of the trapped vortex structures: visualization of the streamline flow field behavior up to $t=0.4$

To show this, a simulation is performed of the turbine behavior during the first 250 deg of the cycle after being impulsively started. $\Delta t = 0.0005$ with a generation step $\beta = 4$ are the time integration parameters. In Figure (4.4) snapshots are shown of the flow field, that is, of the locations of the vortex singularities at different times; those having a counter-clockwise circulation are depicted in red, the others in blue.

Let us consider these results. The vortical structures inside the cavities remain trapped at all the angles of attack experienced by the blades. They vary their strength, and then their shape with respect to the incidence, so they act as passive control devices which change the camber of the airfoils in order to stabilize as much as possible the flow around them. Another feature to be considered for the design of a VAWT is the interaction of the flow field around the blades with the wake previously shed. As it can be seen in Figure (4.4)(e), when the blades pass through the wakes the vortex structures continue to remain trapped in the cavities, without being too perturbed.

In conclusion it is possible to say that the cavities in the profiles work well, being able to maintain the vortices trapped at all the azimuthal positions during the working cycle. This is obtained in the limit of an inviscid model, so neglecting the secondary separations and the arising instability phenomena both on the blades contours and into the cavities, which are fundamental to study the detachment phenomena, being one of their main causes. However in a first approximation like the one performed here, considering their growing time scale larger than the time scale of a turbine working-cycle, the obtained results become of a certain interest, and we can consider them as a first proof that this technology could be a promising technique to pursue in the future. This is the task we wanted to verify, all the good features of this technology depending on it. However to obtain more significant results viscous models need to be used in the future in order to give a complete description of all the aspects characterizing this kind of flow field.

To evaluate the applicability of such a technology to a VAWT a performance analysis should be done too. As said in [19], until now it is possible to suppose that, compared to the classical one, the innovative shape here presented can enhance the performance, but not so much, its goal being to control the stall rather than to produce more energy. Another task which could be great to achieve in the future is the reduction of the computational time: the model here implemented, whose computational cost increases at the range $O(N^2)$,

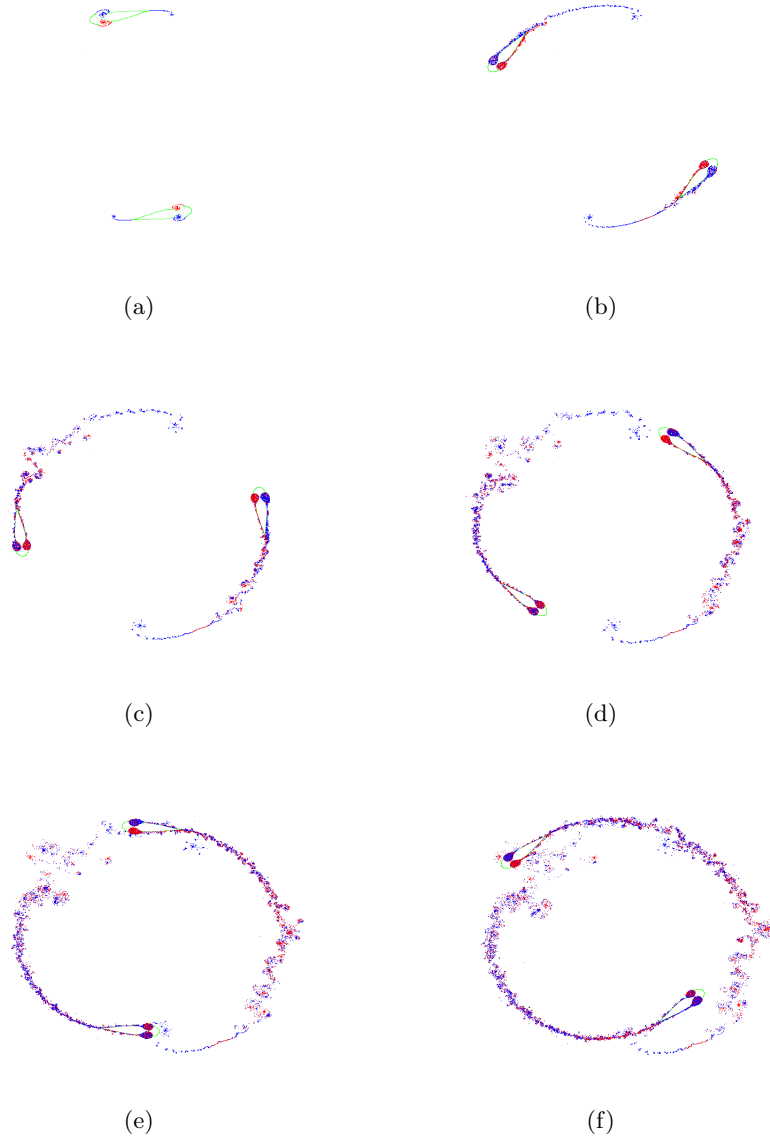


Figure 4.4. Development in time of the flow field past a two-blade turbine with vortex trapping cavities; snapshots at: ($t = 0.4, N = 1186$) (a), ($t = 1.818, N = 5392$) (b), ($t = 3.37, N = 9904$) (c), ($t = 4.89, N = 14311$) (d), ($t = 6.14, N = 17914$) (e), ($t = 7.71, N = 22424$) (f)

N being the number of shed vortices, doesn't enable great simulations in term of time efficiency, so it would be good to substitute it by faster methods ([14]).

Part II

Setting-up of a penalized fully Navier-Stokes equations solver

Chapter 5

Fully Navier-Stokes equations solver

The second part of the present work focuses on the development of a numerical solver able to treat the complete penalized Navier-Stokes equations for compressible flows. The penalization technique is the innovative feature here implemented. Nowadays some of the industrial research interests is oriented to the study of flows around bodies with complex geometries. The classical approach consists in building an unstructured conformal-to-the-body mesh, on which to perform the computation with one of the many appropriate numerical methods, resulting in a certain amount of time only devoted to the set-up of the analysis. The idea of the newly arisen techniques is to avoid this waste of time, allowing the use of a simple cartesian grid over which bodies of any shape are placed.

But, how does one impose the correct boundary conditions on the body contours? As previously said, a lot of techniques exist which can be adopted. For example the immersed boundary methods, such as the ghost-cell type or the cut-cell type, which allow to impose directly the conditions on the body contours by means of opportune interpolation schemes. Another group of such methods is represented by the penalization techniques, which are based on the assumption that the bodies into the domain are porous media of a porosity tending to zero in comparison to that of the external flow field, which on the contrary tends to infinity. Until now, this latter kind of method has been mostly developed for incompressible flows (see, for instance, [1] and [31]). Nowadays some techniques are also

beginning to be developed for compressible flows, such as [40]. A recent technique which seems to be very promising, requiring a simple solver code and a short time for setting-up a computational analysis of the aerodynamic flow field around bodies of any geometry is the one presented in [6] and [10], which we will use in this work. Firstly, the body geometry must be identified pointing out which of the grid cells are inside it; the Heaviside function H can be adopted, which takes a value of 0 in the fluid and of 1 in the body. The body contours are then defined by the sides of the quadrilateral grid cells, obviously with a better precision if the grid is fine. For the incompressible flows, the no-slip condition being the only one to be applied, the penalization of the momentum equations is performed: the idea is to consider all the domain covered by the fluid, with the regions outside the bodies solved by means of the fully Navier-Stokes equations, and the region inside with the penalized equations. The same idea is here developed for compressible flows, the natural extension being to impose the temperature on the bodies penalizing also the energy equation. In this way the flow is defined onto an obstacle-free computational domain, allowing the use of simple cartesian meshes, which, in turn, allow a fast and simple implementation of discrete numerical schemes.

The work is organized as follows: firstly, the fully Navier-Stokes governing equations are presented; they are solved by means of a classical finite volume method, that is, solving the Riemann problem at the interfaces between every cell for the convective part (Osher solver is used [48], [47]), and computing the gradients for the diffusive part with a finite difference scheme. After the validation, the penalization terms are introduced, developing a semi-implicit scheme in order not to be limited by untractable stability conditions imposed by the penalization terms, as done in [6], where the technique is tested only on supersonic high-Reynolds number flows. In the present work the solver code is validated on two test cases used also by Boiron, that is the detached shock in front of a cylinder which is moving at supersonic speed, and the interaction between a circular cylinder at rest and a translating shock. The validation of the same code is also performed on a subsonic low Reynolds number flow case, that is, the von Kármán street past a confined square cylinder: this is done in order to make a probing test on the capability of the penalization technique here adopted to simulate also flow governed by complicated unsteady phenomena; the comparison is made with the results of the INRIA code AERO,

which is an unstructured body-fitted solver, and a good agreement is obtained. The same agreement that is obtained making the validation of the fully implicit version of the same penalized code: the semi-implicit scheme has the drawback that the CFL number is limited by the stability conditions imposed by both the convective and the diffusive parts of the Navier-Stokes equations, resulting in not so good computational time efficiency. So we decided to implement the penalized code previously developed into a fully implicit version: the results obtained in terms of CFL numbers are good, increasing them by a factor of at least 10. In the end, an example of an application is shown, where the bodies are moving: in this case the advantages of the penalization technique are even more evident, because the grid never changes, with the code remaining almost the same used for bodies at rest, except for the definition of the Heaviside function which determines the body contours, and with the consequent better time efficiency.

A final clarification about the numerical technique adopted for the fully implicit scheme is needed. The GMRES is employed to solve the resulting linearized equations, and this is done by means of the conjugation of a preconditioner based on the incomplete LU factorization and the explicit computation of the Jacobian matrix based on a finite-difference scheme. This is not the most efficient available technique, but however the computational efficiency is out of the purposes of the present work. In fact, the original spirit was to build a Jacobian-free scheme for the penalized equations: the first step was to demonstrate and verify the capabilities of the penalization techniques, obtaining also an improvement in term of CFL number with respect to the semi-implicit method. In the next future, the attention will be focused on the efficiency of the numerical method, which, in the spirit of a Jacobian-free scheme, will imply the conjugation of a new preconditioner, different from the one here adopted, and the consequent possibility to not compute the Jacobian matrix. Among the drawbacks relative to the employment of a preconditioner based on the incomplete LU factorization, as the one here adopted, there is also the not good efficiency in term of occupied CPU memory; this is why the grid resolution used for the test case analysis will be sometimes not so fine as for the semi-implicit version. The future change of the preconditioner will also have to take into account this feature.

5.1 Governing equations

The penalization technique here described is applied to 2D compressible and viscous flows, so the Navier-Stokes equations are considered. The finite volume method being used, the equations are expressed in the conservative form over the control volume V and its surface Σ :

$$\begin{aligned} \frac{d}{dt} \int_V \rho dV + \int_{\Sigma} \rho \vec{q} \cdot \vec{n} d\sigma &= 0 \\ \frac{d}{dt} \int_V \rho \vec{q} dV + \int_{\Sigma} (\rho \vec{q}) \vec{q} \cdot \vec{n} d\sigma + \int_{\Sigma} p \vec{n} d\sigma &= \int_{\Sigma} \bar{\bar{\tau}} \cdot \vec{n} d\sigma \\ \frac{d}{dt} \int_V \rho e dV + \int_{\Sigma} \rho \left(e + \frac{p}{\rho} \right) \vec{q} \cdot \vec{n} d\sigma &= \int_{\Sigma} (\bar{\bar{\tau}} \cdot \vec{n}) \cdot \vec{q} d\sigma + \int_{\Sigma} k \nabla T \cdot \vec{n} d\sigma \end{aligned} \quad (5.1)$$

where ρ is the density, p the pressure, \vec{q} the velocity vector (u,v) , T the temperature, $e = c_V T + \frac{1}{2}(u^2 + v^2)$ the total energy per unit mass, k the thermal conductivity, \vec{n} the outward normal to the surface of the control volume V , and $\bar{\bar{\tau}}$ is the stress viscosity tensor expressed, by means of the Einstein notation, in the following way:

$$\bar{\bar{\tau}} = \mu \left(\frac{\partial u_i}{\partial x_j} + \frac{\partial u_j}{\partial x_i} - \frac{2}{3} \delta_{ij} \frac{\partial u_k}{\partial x_k} \right)$$

μ being the dynamic viscosity. The primitive variable $U = (u,v,p,a)^T$ and the conservative variable $W = (\rho, \rho u, \rho v, \rho e)^T$ vectors are also introduced, with a denoting the speed of sound.

An adimensionalization is performed taking as reference variables the quantities U_{∞} , ρ_{∞} and μ_{∞} of the undisturbed flow at infinity, and the characteristic length L_R of the problem:

$$\begin{aligned} L' &= \frac{L}{L_R}; & \rho' &= \frac{\rho}{\rho_{\infty}}; & \vec{q}' &= \frac{\vec{q}}{U_{\infty}}; & \mu' &= \frac{\mu}{\mu_{\infty}}; \\ p' &= \frac{p}{\rho_{\infty} U_{\infty}^2}; & T' &= \frac{T}{U_{\infty}^2/R}; & e' &= \frac{e}{U_{\infty}^2}; & k' &= \frac{k}{k_{\infty}}; \end{aligned} \quad (5.2)$$

R being the specific gas constant.

The resulting equations are the (5.3), where the dimensionless variables are written without the apex as in the subsequent expressions:

$$\begin{aligned} \frac{d}{dt} \int_V \rho dV + \int_{\Sigma} \rho \vec{q} \cdot \vec{n} d\sigma &= 0 \\ \frac{d}{dt} \int_V \rho \vec{q} dV + \int_{\Sigma} (\rho \vec{q}) \vec{q} \cdot \vec{n} d\sigma + \int_{\Sigma} p \vec{n} d\sigma &= \frac{1}{Re} \int_{\Sigma} \bar{\tau} \cdot \vec{n} d\sigma \\ \frac{d}{dt} \int_V \rho e dV + \int_{\Sigma} \rho \left(e + \frac{p}{\rho} \right) \vec{q} \cdot \vec{n} d\sigma &= \frac{1}{Re} \int_{\Sigma} (\bar{\tau} \cdot \vec{n}) \cdot \vec{q} d\sigma + \frac{\gamma}{\gamma - 1} \frac{1}{Pr} \frac{1}{Re} \int_{\Sigma} k \nabla T \cdot \vec{n} d\sigma \end{aligned} \quad (5.3)$$

where:

$$Re = \frac{\rho_{\infty} U_{\infty} L_R}{\mu_{\infty}}; \quad Pr = \frac{\mu_{\infty} c_P}{k_{\infty}} \quad (5.4)$$

γ being the specific heat ratio c_p/c_v (assumed constant and equal to 1.4).

The dynamic viscosity μ , depending on the analysed case, will be considered constant (for low Mach number flows), or a function of the temperature (for high Mach number flows) according to the following relation:

$$\frac{\mu}{\mu_{\infty}} = \left(\frac{T}{T_{\infty}} \right)^n, \quad 0.5 < n < 1. \quad (5.5)$$

The thermal conduction and the viscous friction being governed by the same diffusive mechanism at ordinary temperatures, the thermal conductivity varies with T in the same way as μ , so the Prandtl number can be considered constant, and equal to 0.72, the value for the air.

5.2 Discretization technique

In the first part of the work a numerical code is built which solves the Navier-Stokes equations (5.3). The convective part is discretized and solved computing the fluxes \vec{F}_C at the interfaces between cells by means of the Osher solver for the Riemann problem [48], [47]; a first order and then a second order techniques are implemented. The second step is the treatment of the viscous and thermal fluxes \vec{F}_D , which are discretized directly by a second order scheme. The governing equations (5.3) can then be written as:

$$\frac{d}{dt} \int_V W dV + \int_{\Sigma} \vec{F}_C \cdot \vec{n} d\sigma = \int_{\Sigma} \vec{F}_D \cdot \vec{n} d\sigma \quad (5.6)$$

where \vec{n} is the outward normal to the sides of each single grid cell.

For the integration in time, both first- and second-order explicit and implicit techniques are coded. A description of the boundary conditions is also given which will be adopted next. In the end, to validate the resulting code, a test for the Euler part and another one for the complete Navier-Stokes equations are performed.

5.2.1 Convective fluxes

Neglecting the viscosity and the thermal conductivity in (5.3), the Euler equations are obtained. In the first order approximation the initial conditions are discretized on the grid taking a constant value into each cell; discontinuity propagation problems are then defined at each cell interface, the so called Riemann problems (see [21]). To describe the evolution of the disturbance, the flux-difference splitting (FDS) technique (see [49]) is applied, where the flux vector is:

$$\vec{F}_C = \begin{pmatrix} \rho u_n \\ \rho u u_n + p n_x \\ \rho v u_n + p n_y \\ \rho \left(e + \frac{p}{\rho} \right) u_n \end{pmatrix} \quad (5.7)$$

\vec{n} being always the outward normal to the considered side of the cell. The computation of the fluxes is performed by means of the approximate Osher solver (see [47]): the acoustic waves are considered as isentropic, so the variables in regions c , d (see Fig.(5.1)) are derived from those of initial regions a , b using the simple expressions which connect the Riemann invariants:

$$R_1 = u - \frac{2}{\gamma - 1} a; \quad R_2 = \text{entropy}; \quad R_3 = u + \frac{2}{\gamma - 1} a;$$

R_1 remaining constant along the characteristic $u - a$, R_2 along u and R_3 along $u + a$.

2D domains being studied, the approximation method just introduced is extended along both the directions \vec{x} and \vec{y} independently one from another. But, according to the theory, a 2D wave propagation can't be broken down into two 1D propagation problems:

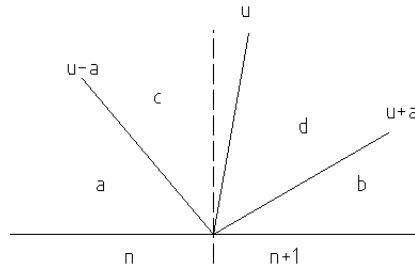


Figure 5.1. Riemann problem at the interface between the n -th and $(n + 1)$ -th cells

for example, an oblique shock can't be considered as the sum of two normal shocks, the error being bigger when the shock is weak because the two resulting 1D problems could start from subsonic initial conditions. However the 2D governing equations guarantee the bidimensionality of the problem, the error being confined to local area, resulting in a little less precision: an example is the diffusion of the oblique shocks.

A second order scheme is also implemented: the conservative variables $w_{m,n}^k$ on the (m -th, n -th) cell at the time step k are not taken constant, but having a linear distribution on both the directions. Taking into account only one direction (the extension to the other is trivial), let consider Fig.(5.2). The slope of the distribution on the cell n is computed from those between the n -th cell and the previous $(n - 1)$ -th and successive $(n + 1)$ -th ones:

$$\sigma_n^- = \frac{w_n^k - w_{n-1}^k}{\Delta x}; \quad \sigma_n^+ = \frac{w_{n+1}^k - w_n^k}{\Delta x}$$

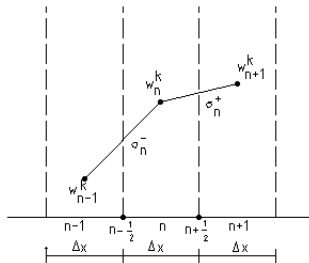


Figure 5.2. Determination of the slope for the linear distribution of the conservative variables into the n -th cell

For problems without discontinuities the average value is used, that is:

$$\sigma_n^k = \frac{\sigma_n^- + \sigma_n^+}{2}.$$

While, in presence of shocks the classical *MINMOD* slope limiter is implemented:

$$\begin{aligned} \sigma_n^k &= \text{MINMOD}(\sigma_n^-, \sigma_n^+) \\ &= \begin{cases} \text{sign}(\sigma_n^-) \cdot \text{MIN}(|\sigma_n^-|, |\sigma_n^+|) & \Leftrightarrow (\sigma_n^- \cdot \sigma_n^+) > 0 \\ 0 & \Leftrightarrow (\sigma_n^- \cdot \sigma_n^+) < 0 \end{cases} \end{aligned}$$

With this technique the method comes back to the first order across discontinuities. But, for reasons that will become clear later, with an implicit scheme when strong discontinuities are present the *MINMOD* doesn't lead to convergence, not being differentiable. In these cases the slope limiter of [73] will be used.

For a second order scheme the Riemann problem *RP* at the interface $n + \frac{1}{2}$ between the n -th and $(n + 1)$ -th cells is then defined in the following way:

$$RP_{n+\frac{1}{2}} : \begin{cases} w_{n+\frac{1}{2}}^L = w_n^k + \sigma_n^k \frac{\Delta x}{2} \\ w_{n+\frac{1}{2}}^R = w_{n+1}^k - \sigma_{n+1}^k \frac{\Delta x}{2} \end{cases} \quad (5.8)$$

L and R representing the value at the left and at the right of the interface, respectively.

5.2.2 Diffusive fluxes

The diffusive flux vector \vec{F}_D can be considered as the sum of the viscous \vec{F}_V and the thermal \vec{F}_T ones:

$$\vec{F}_V = \begin{pmatrix} 0 \\ n_x \left(\frac{4}{3} \frac{\partial u}{\partial x} - \frac{2}{3} \frac{\partial v}{\partial y} \right) + n_y \left(\frac{\partial u}{\partial y} + \frac{\partial v}{\partial x} \right) \\ n_x \left(\frac{\partial u}{\partial y} + \frac{\partial v}{\partial x} \right) + n_y \left(\frac{4}{3} \frac{\partial v}{\partial y} - \frac{2}{3} \frac{\partial u}{\partial x} \right) \\ \left[n_x \left(\frac{4}{3} \frac{\partial u}{\partial x} - \frac{2}{3} \frac{\partial v}{\partial y} \right) + n_y \left(\frac{\partial u}{\partial y} + \frac{\partial v}{\partial x} \right) \right] u + \left[n_x \left(\frac{\partial u}{\partial y} + \frac{\partial v}{\partial x} \right) + n_y \left(\frac{4}{3} \frac{\partial v}{\partial y} - \frac{2}{3} \frac{\partial u}{\partial x} \right) \right] v \end{pmatrix} \cdot \frac{\mu}{Re} \quad (5.9)$$

$$\vec{F}_T = \begin{pmatrix} 0 \\ 0 \\ 0 \\ n_x \frac{\partial T}{\partial x} + n_y \frac{\partial T}{\partial y} \end{pmatrix} \cdot \frac{\gamma}{\gamma - 1} \frac{k}{Pr} \frac{1}{Re} \quad (5.10)$$

The grid being Cartesian, the computational domain is subdivided into quadrangular cells of volume $\Omega_{m,n}$, $m = 1, \dots, M$, $n = 1, \dots, N$. Across each of their sides the gradients ∇u , ∇v and ∇T are needed. We consider the (m -th, n -th) cell, for which the horizontal velocity gradient has to be computed (see Fig.(5.3)).

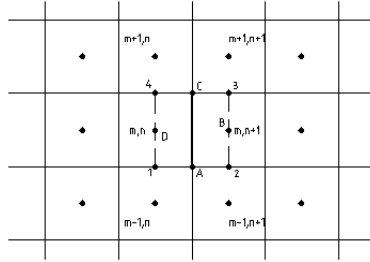


Figure 5.3. Gradient computation on the displaced cells

The Gauss theorem states that:

$$\int_{\Sigma} u \vec{n} d\sigma = \int_V \nabla u dV$$

According to it, the following discrete expression is derived:

$$\nabla u_{AC} = \frac{1}{\Omega_{ABCD}} \cdot \int_{S_{ABCD}} u \vec{n} d\sigma$$

where:

- ∇u_{AC} = horizontal velocity gradient at the interface with the extreme points in A and C;
- Ω_{ABCD} = volume of the cell with edges:

$$z_1 = \left(x_{m,n}, \frac{y_{m,n} + y_{m-1,n}}{2} \right); \quad z_2 = \left(x_{m,n+1}, \frac{y_{m,n+1} + y_{m-1,n+1}}{2} \right);$$

$$z_3 = \left(x_{m,n+1}, \frac{y_{m,n+1} + y_{m+1,n+1}}{2} \right); \quad z_4 = \left(x_{m,n}, \frac{y_{m,n} + y_{m+1,n}}{2} \right);$$

- S_{ABCD} = area of the interface surrounding the volume Ω_{ABCD} ;
- \vec{n} = outward normal to each side of the cell Ω_{ABCD} .

On each side of the cell Ω_{ABCD} u is assumed to take a constant value, then its gradient is discretized as:

$$\nabla u = \left(\frac{u_B - u_D}{\Delta x}, \frac{u_C - u_A}{\Delta y} \right), \quad (5.11)$$

u_B, u_D being the values of u in the center of the cells $(m,n), (m,n+1)$, and u_A, u_C being the interpolated values from the cells $(m,n), (m,n+1), (m+1,n+1), (m+1,n)$ and $(m,n), (m,n+1), (m-1,n+1), (m-1,n)$, respectively.

The expressions for ∇v and ∇T are obtained in the same way. The resulting fluxes are second order accurate.

5.2.3 Boundary conditions

In all the examples and the cases here studied, also when the penalization technique will be introduced, qualitatively similar boundary conditions are applied which will now be described. The imposed values of the variables will be specified after in each single case.

Domains with wall conditions are present in a lot of cases: the grid being cartesian, the wall results overlapped to the sides of cells. In this way the computation of fluxes is simplified. For the convective fluxes, the normal to the wall velocity being zero, only the pressure term has to be computed. Solving a half-Riemann problem, the convective flux vector $(0, pn_x, pn_y, 0)^T$ is then completely known. For the diffusive fluxes, a half-volume cell is built, as shown in Figure (5.4).

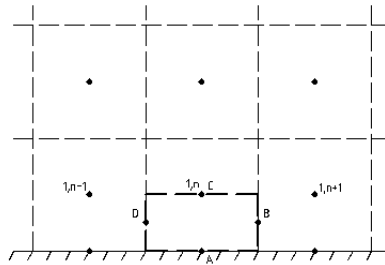


Figure 5.4. Gradient computation on the wall cells; a half-volume cell is considered.

Applying the gradient theorem as above described, the expression for the gradient at the wall surface follows:

$$\nabla T = \left(\frac{T_B - T_D}{\Delta x}, \frac{T_C - T_A}{\Delta y/2} \right), \quad (5.12)$$

where T_A is the temperature at the wall, and T_B, T_D are computed interpolating the values at the wall and in the cells $(1, n), (1, n + 1)$ and $(1, n), (1, n - 1)$, respectively. The same procedure is applied for the velocity gradients $\nabla u, \nabla v$, imposing $u = v = 0$ at the wall.

In addition to the wall boundary conditions, on the exterior contour of the domain the variables are imposed in two different ways. That is, defining them either on the interfaces of the first cells into the domain or into the first cells outside the domain. In the former case, the fluxes are usually directly defined, in the latter one the free-stream variables.

5.2.4 Time integration schemes

Two different time integration schemes are implemented, an explicit one and an implicit one. Later, a semi-implicit scheme will also be introduced, but it will be described when the penalization technique is used.

We consider the equation (5.6); it can be discretized as:

$$\frac{(\Delta w_j)_{m,n}}{\Delta t} \Omega_{m,n} = -R(w_j)_{m,n} \quad (5.13)$$

where:

- $(\Delta w_j)_{m,n} = (w_j)_{m,n}^{k+1} - (w_j)_{m,n}^k$ represents the difference between the j -th conservative variable evaluated at two successive time steps k and $k + 1$ for the $(m$ -th, n -th) cell;
- $R(w_j)_{m,n}$ is the sum of convective and diffusive fluxes, that is, the residual, for the j -th conservative variable $(w_j)_{m,n}$ related to the $(m$ -th, n -th) cell;
- $\Omega_{m,n}$ is the area of the $(m$ -th, n -th) cell.

The explicit scheme is built taking the right hand side of the equation (5.13) at the old time step k ; so the implemented expression is:

$$(w_j)_{m,n}^{k+1} = (w_j)_{m,n}^k - \frac{\Delta t}{\Omega_{m,n}} \cdot R(w_j)_{m,n}^k. \quad (5.14)$$

The time interval Δt has an upper stability limit Δt_{max} due both to the convective and to the diffusive parts of the Navier-Stokes equations; relative to the convective restriction, the influence domain of the initial conditions into the Riemann problem has to be respected, so the maximum time step Δt_C is defined as:

$$\Delta t_C = CFL_1 \cdot \frac{\min(\Delta x, \Delta y)}{A_k}, \quad (5.15)$$

where A_k is the maximum wave speed into the domain at the k -th time step. About the diffusive restriction, according to [25], the maximum time step Δt_D results in the following expression:

$$\Delta t_D = CFL_2 \cdot [\min(\Delta x, \Delta y)]^2 \cdot Re \cdot \left[\max \left(1, \frac{Pr \cdot (\gamma - 1)}{\gamma} \right) \right]. \quad (5.16)$$

The total upper stability limit Δt_{max} is then the minimum value between Δt_C and Δt_D . In the next analysed cases, CFL_1 and CFL_2 are assumed equal, and their value will be specified later for each numerical computation.

The scheme in equation (5.14) is of first order; to achieve the second order the classical Runge-Kutta method is adopted:

$$\begin{cases} (w_j)_{m,n}^* = (w_j)_{m,n}^k - \frac{\Delta t}{\Omega_{m,n}} \cdot R(w_j)_{m,n}^k \\ (w_j)_{m,n}^{k+1} = \frac{1}{2} \cdot \left[(w_j)_{m,n}^k + (w_j)_{m,n}^* - \frac{\Delta t}{\Omega_{m,n}} R(w_j)_{m,n}^* \right] \end{cases}, \quad (5.17)$$

where $(w_j)_{m,n}^*$ is the intermediate conservative variable computed at each iteration in time.

On the other hand, the implicit scheme is obtained taking the residual in equation (5.13) at the successive time step, that is, at the $(k+1)$ -th one; $R(w_j)_{m,n}^{k+1}$ being expressed by means of a Taylor series around the value at k , the following expression is obtained:

$$\left(\frac{\Omega}{\Delta t} I + J^k \right) \Delta W = -R(W^k), \quad (5.18)$$

where I is the identity matrix. The Jacobian matrix J^k is computed deriving the residual of the i -th conservative variable of the l -th cell, $l = 1, \dots, L$, L being the total number of cells into which the domain is discretized, in the j -th conservative variable of the t -th cell, $t = 1, \dots, T$, $T = L$, all done at the old k -th time step, that is:

$$\left[(J_{i,l})_{j,t} \right]^k = \left(\frac{\partial R(w_i)_l}{\partial (w_j)_t} \right)^k \simeq \left(\frac{R_i^l(w_j^t + \varepsilon) - R_i^l(w_j^t)}{\varepsilon} \right)^k. \quad (5.19)$$

The resulting linearized system of equations (5.18), after being preconditioned by means of the incomplete LU factorization, is solved using the *GMRES* iterative method (see Saad [61]). In this scheme there isn't any constraint on the time step, resulting in a faster convergence for steady problems and in larger Δt for the unsteady ones. The unique restriction is about the condition number of the matrix at the left side in equation (5.18): in fact, it increases as well as the CFL number increases, the GMRES needing more iterations to converge. However a compromise can be found at high CFL numbers. On the contrary, the major drawback of the implicit scheme is the large amount of required memory; for very fine grids the semi-implicit scheme will then be used, which will be described later. However, performing an opportune well defined preconditioning, this problem could be avoided, but this is beyond the aim of the present work.

The second order in time implicit scheme is quickly derived substituting in equation (5.18) the residual $R(W^k)$ with that computed at the intermediate time step $\frac{\Delta t}{2}$, that is, $R\left(\frac{W^{k+1} + W^k}{2}\right)$; performing, as above, a Taylor series expansion near the k -th step value, the resulting scheme is:

$$\left(\frac{\Omega}{\Delta t} I + \frac{1}{2} J^k \right) \Delta W = -R(W^k). \quad (5.20)$$

A clarification has to be done about the way the Jacobian matrix is computed. If we compute explicitly each term of this matrix, that is, we compute also the terms we can *a priori* say that are zero, then the computation cost grows-up quadratically with the number of grid cells, becoming too much expensive. So we have adopted a technique which already takes into account the stencil of the employed numerical scheme, reducing the computation only to the terms we already know can be different from zero. The adopted stencil is represented in Figure (5.5): the white cell indicates where the conservative variables are

perturbed; the blue cells indicate where the residual is perturbed both by the convective and the diffusive terms; the green cells indicate where the residual is perturbed only by the convective terms; and finally the yellow cells indicate where the residual results perturbed only by the diffusive terms. In this way the resulting computational cost is of order $O(N)$, N being the number of grid cells discretizing the domain.

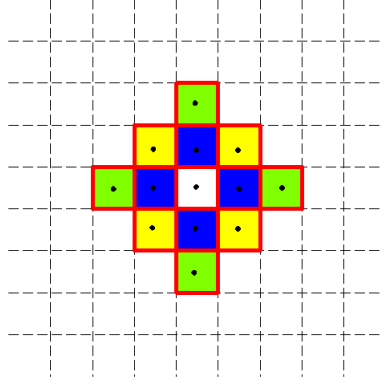


Figure 5.5. Stencil for the computation of the Jacobian matrix terms.

5.3 Validation

The code is validated step by step, verifying firstly the Euler inviscid part, and then the diffusive one. The grid is always Cartesian, as it will be with the penalization technique. Tests are performed evaluating the grid convergence, that is, verifying that the slope of the curve in the $\text{Log}(\text{error}) - \text{Log}(\text{gridpoints})$ graph is close to the theoretical one. The error is a percentage error computed by means of the 1 – norm in this way:

$$ERR_1 = \frac{\int_V |Sol_{exact} - Sol_{num}| dV}{\int_V |Sol_{exact}| dV}.$$

Euler test case

To validate the Euler part of the code the analytic steady solution shown in Figure (5.6) is taken as reference, according to [53].

The flow enters from the left and lower sides with supersonic horizontal velocity; a shock separates these two different flow regions, (1) and (2), and, reflecting on the upper

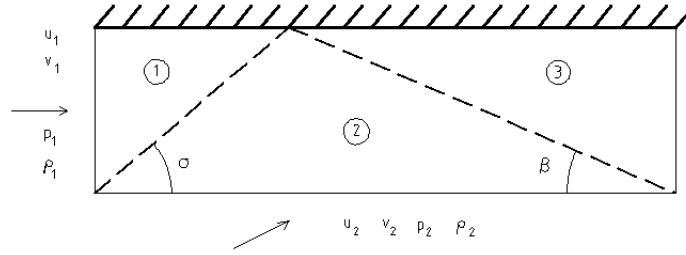


Figure 5.6. Euler test case: reflecting shock

side where a wall is supposed to be, the new region (3) is defined. The values of the variables which allow to achieve this stationary solution are:

$$Region\ 1 \equiv \left\{ \begin{array}{l} u_1 = 2.9 \\ v_1 = 0 \\ p_1 = 1.0 \\ \rho_1 = 1.4 \end{array} \right\}; \quad Region\ 2 \equiv \left\{ \begin{array}{l} u_2 = 2.5876 \\ v_2 = 0.5438 \\ p_2 = 2.2685 \\ \rho_2 = 2.4739 \end{array} \right\}.$$

Performing the analytical computation, the resulting values for the shock slopes and for the Mach number in region 3 are:

$$\sigma = 29.8817deg$$

$$\beta = 23.8711deg$$

$$M_3 = 1.8676$$

$$v_3 = 0.$$

With the numerical schemes built above the same results must be obtained. The computation is performed into the rectangular domain $\Omega = [0,4] \times [0,1]$ with five different uniform grids: $G_1 = 10 \times 40$, $G_2 = 20 \times 80$, $G_3 = 40 \times 160$, $G_4 = 80 \times 320$ and $G_5 = 160 \times 640$. The boundary conditions are:

- on the left side: $\rho = \rho_1$, $u = u_1$, $v = v_1$, $p = p_1$;
- on the lower side: $\rho = \rho_2$, $u = u_2$, $v = v_2$, $p = p_2$;
- on the right side: supersonic conditions;
- on the upper side: reflecting conditions.

As initial conditions, the inlet conditions are imposed all over the domain.

This problem has been solved both with the first and second order explicit and implicit schemes; the slopes of the conservative variables into each cells are evaluated by means of the minmod slope limiter for the explicit scheme, and of the [73] differentiable slope limiter for the implicit one in order to achieve the convergence.

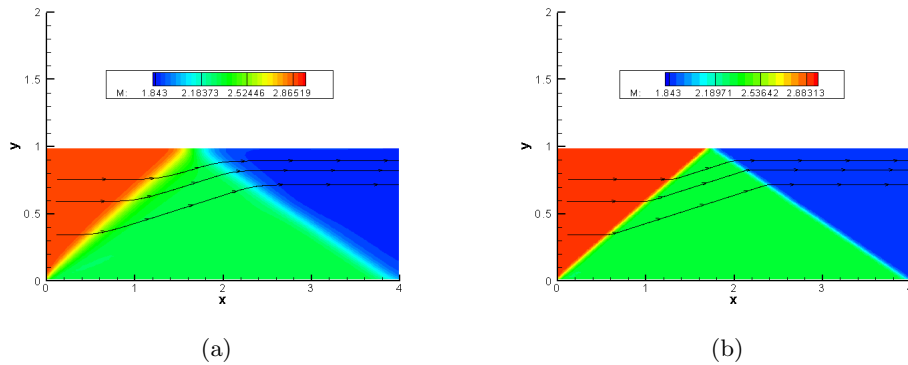


Figure 5.7. Mach number flow field: in (a) the first order scheme results, in (b) those of the second order scheme; three streamlines are shown for each snapshot.

In Figure (5.7) the steady solutions for the Mach number, which have been obtained by means of the first and second order schemes over the G_3 grid, are shown; the iterations are stopped when the sum of the fluxes averaged over the all cells is less than 10^{-7} .

In Figure (5.8) the 1 – norm error computed on the Mach value on the entire domain is plotted in logarithmic scale as a function of the number of grid cells along \vec{x} : the red curve is relative to the first order and the blue one to the second order scheme. According to [37], the slopes of both the curves are in good agreement with the theoretical values; in fact, the rate of convergence for the first order is 0.47, and for the second order is 0.655, what is expected for a flow field where discontinuities are present.

Navier-Stokes test case

The compressible flow over a flat plate is considered. As reference case, that described in [66] is taken into account. To analytically solve the problem, assumptions are made which simplify the Navier-Stokes equations: in particular, considering a region sufficiently far from the leading edge, the velocity normal to the plate can be neglected and the boundary

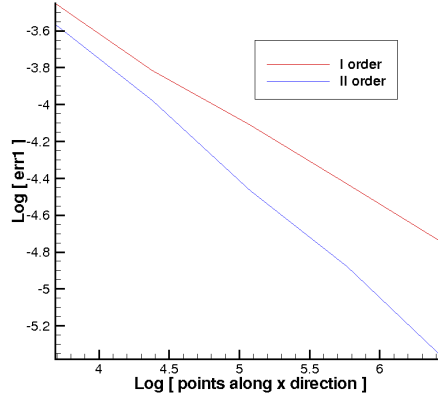


Figure 5.8. Rate of convergence for the first and second order schemes

layer can be thought as parallel to it; the pressure gradient is imposed to be null, and the wall temperature T_w is taken constant along the plate. In this way, the gradients along the wall being zero, similarity is expected in the flow patterns at all values of x .

The self-similar solutions for velocity and temperature are obtained solving this equation:

$$-\frac{\zeta}{2} \frac{du'}{d\zeta} = \frac{d}{d\zeta} \left(u' T'^{m-1} \frac{du'}{d\zeta} \right), \quad \zeta = \frac{\psi'}{\sqrt{x'}} = \frac{\psi}{\sqrt{\mu_\infty U_\infty x / \rho_\infty}}, \quad \mu' = \frac{\mu}{\mu_\infty} = \left(\frac{T}{T_\infty} \right)^n \quad (5.21)$$

where the apex is applied to dimensionless variables, ψ represents the stream function, and T' is related to u' by means of the following expression:

$$T'(\zeta) = T'_w + (T'_{0\infty} - T'_w) u'(\zeta) + \frac{\gamma - 1}{2} M_\infty^2 u'(\zeta)^2,$$

$T'_{0\infty}$ being the total temperature at infinity. The resulting velocity and temperature profiles are then plotted (Figures (5.9)) with respect to the self-similar variable:

$$\frac{y}{x} \sqrt{Re_x} = \int_0^\zeta \frac{T'(\zeta)}{u'(\zeta)} d\zeta.$$

Once the analytical problem has been solved, we can treat the numerical one. The reference solution is defined for $M_\infty = 0.8$, $T_w/T_\infty = 1/4$, $Re_\infty = 500$, $Pr = 1$ and

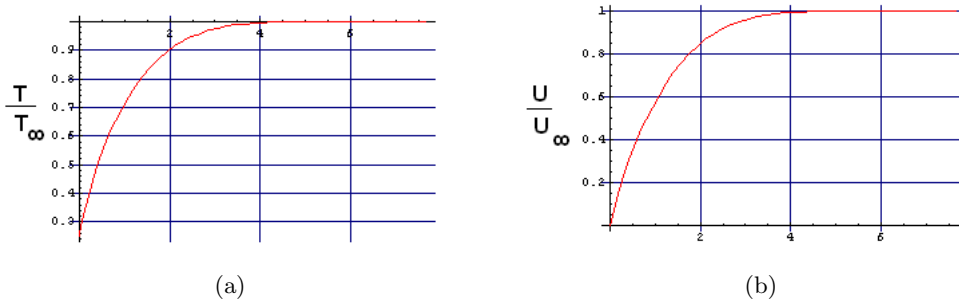


Figure 5.9. The temperature (a) and velocity (b) self-similar profiles.

$n = 0.76$. The computational domain Ω is $[0.5,1] \times [0,2]$; on the lower side wall boundary conditions are imposed; on the upper side free-stream boundary conditions are defined; on the left and right sides the self-similar profiles for velocity and temperature are adapted to the specific abscissa where they are placed and to the grid. The computations are performed on three different grids having, along the flat plate normal direction, G_1 20, G_2 40 and G_3 80 cells, respectively. About the viscosity behavior, the expression (5.5) is used. In Figure (5.10) the resulting horizontal velocity and temperature distributions are shown all over the domain for the grid G_3 .

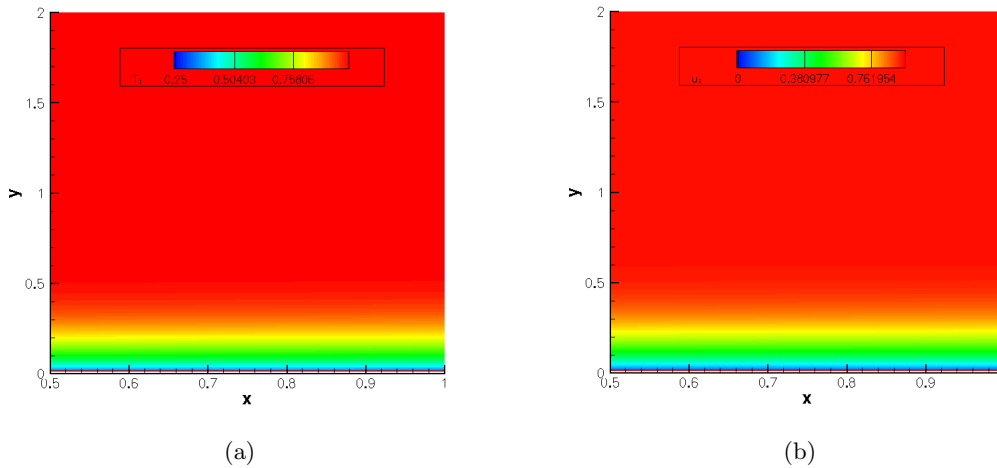


Figure 5.10. Numerical solutions for T and u over the G_3 grid.

It has to be noticed that the numerical code solves the Navier-Stokes equations, but the analytical model presented by Shapiro is not an exact solution to them. This results in

an error which rises from the right and left sides when the grid is refined, because, in fact, on these boundary contours the imposed conditions are not exactly in agreement with the Navier-Stokes equations. Then, to verify the accuracy and the grid convergence of the code, the numerical solution is considered at the abscissa 0.75, sufficiently far from the right and left sides in order not to be influenced by them. Moreover, since the accuracy level can't be greater than a certain limit value, the grid convergence is tested in the following way: a numerical solution obtained for a very fine grid G_4 (320 cells along the normal to the plate direction) is taken as the reference solution. The 1 – norm error is then evaluated between this solution and those computed for the coarser grids. The results are shown in Figure (5.11): the red curve being relative to the first order scheme and the blue one to the second order one, they are almost parallel with a slope of $\simeq 2$; this is in agreement with the fact that the boundary layer is dominated by diffusive effects, and in both the schemes the diffusive part of the governing equations is discretized with a second order technique.

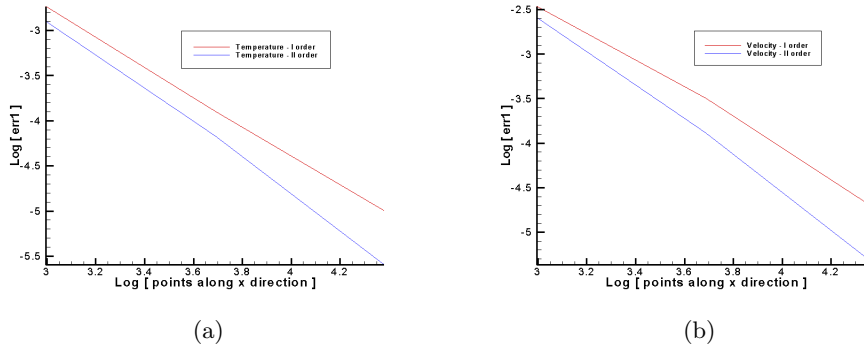


Figure 5.11. Temperature (a) and velocity (b) rate of convergence to the solution obtained by means of the G_4 grid.

Chapter 6

The Penalization Method

The present work is devoted to the implementation of a code solving compressible Navier-Stokes equations with the penalization technique. This is a method to solve flow fields outside bodies without taking into account their shape. In other words, it is introduced to impose the correct boundary conditions on the body contours without having conformal-to-the-body grids. The use of very simple cartesian grids is then allowed, reducing a lot the time of mesh generation and all the problems related to it.

Compressible flows being treated, the boundary conditions to be imposed on the body contours are on the velocity (no-slip condition), and on the temperature. Then the penalized equations are those of conservation of momentum and energy, resulting in the following new dimensionless system to be solved:

$$\frac{d}{dt} \int_V W dV + \int_{\Sigma} \vec{F}_C \cdot \vec{n} d\sigma = \int_{\Sigma} \vec{F}_D \cdot \vec{n} d\sigma - \frac{H}{\phi} S, \quad (6.1)$$

where:

$$S(w_{m,n}) = \left\{ \begin{array}{c} 0 \\ \rho_{m,n} (u_{m,n} - u_0) \\ \rho_{m,n} (v_{m,n} - v_0) \\ \frac{1}{\gamma-1} \rho_{m,n} (T_{m,n} - T_0) \end{array} \right\} \Omega_{m,n}. \quad (6.2)$$

(u_0, v_0, T_0) are the body velocities and temperature; with a conformal-to-the-body grid, they would be imposed exactly on the body contours. $\Omega_{m,n}$, $\rho_{m,n}$, $u_{m,n}$, $v_{m,n}$, $T_{m,n}$ are

the volume area, the density, the velocities and the temperature of the flow, respectively, for the (m -th, n -th) cell over which the body is superimposed. H is the Heaviside function: it assumes the value 1 inside the body, and 0 outside, the penalized term modifying the Navier-Stokes equations only inside it; in this way the body contours are represented by a series of straight segments coinciding with the sides of the grid cells. ϕ represents the so-called penalization parameter: as shown in [6], the smaller the ϕ value is, the better the boundary conditions are respected on the body contours, the error being $O(\phi)$.

It has to be noticed that the penalization terms in the above conservative equations act as sources placed in the cells where the solid bodies are also placed. In fact, the bodies are treated as porous media, with ϕ representing their porosity. The same penalization terms can also be considered as body forces acting on the cells immersed in the bodies themselves.

6.1 Time integration schemes

Starting from the integration schemes described in Section (5.2.4) for the classical Navier-Stokes equations, similar schemes could be obtained also for the penalized equations. But there's a problem to be faced: in the explicit scheme the stability condition which limits the time interval would be too restrictive, because Δt should be of the same order of magnitude as ϕ . ϕ being $O(10^{-12})$, the simulations would be untractable because of the too large computational time. In order to avoid this restriction, a semi-implicit scheme can be implemented. On the other hand, an implicit scheme is developed in order to use greater CFL numbers, obtaining a faster integration in time. Both first and second order are implemented.

6.1.1 Semi-implicit model

To avoid the limitation due to ϕ , the penalized terms are treated implicitly, but both the convective and diffusive ones are explicitly integrated. The resulting first order expression is then:

$$\left(\frac{I}{\Delta t} + \frac{H}{\phi}\right) \cdot \Omega \cdot \Delta W = -R(W^k) + \frac{H}{\phi} \cdot S(W^k) \quad (6.3)$$

For the second order scheme, a classical Runge-Kutta method is used as described in Section (5.2.4).

As it can be noticed, the penalization terms result in a diagonal additive term in the matrix at the left, so in practice the computational work remains the same compared to that needed for the fully explicit scheme. On the other hand, always in comparison with the fully explicit scheme, the stability restrictions due to the convective and diffusive parts also remain the same, resulting in a not so performing technique.

6.1.2 Fully implicit model

The fully implicit scheme enables avoiding the limitation on Δt due both to the penalization parameter ϕ and to the convective and diffusive parts of the Navier-Stokes equations. Starting from the equation (5.18), the first order in time scheme results in the following expression:

$$\left(\frac{\Omega}{\Delta t} I + J^k + \frac{H}{\phi} \Omega \right) \cdot \Delta W = -R(W^k) - \frac{H}{\phi} \cdot S(W^k) \cdot \Omega \quad (6.4)$$

In comparison with the non-penalized scheme, a very large term is added to the diagonal of the matrix at the left, in fact reducing its condition number. So there's a benefit for solving the linear system.

To extend this model to the second order, attention must be paid to the time step at which the residual R and the penalization term S are evaluated. As said above (see Section (5.2.4)), the residual is taken at the intermediate time step $k + \frac{1}{2}$. But S has to be computed always at the $(k + 1)$ -th time step. If it was evaluated at $k + \frac{1}{2}$, the solution inside the bodies would have the correct time averaged value, but at the punctual time $n\Delta t$ inside the bodies the equations reduce to $w^{k+1} = -w^k$. So finally the second order implicit scheme results in the following expression:

$$\left(\frac{\Omega}{\Delta t} I + \frac{1}{2} J^k + \frac{H}{\phi} \Omega \right) \cdot \Delta W = -R(W^k) + \frac{H}{\phi} \cdot S(W^k) \quad (6.5)$$

6.2 Validation

To validate the implemented code, three numerical experiments were performed and compared to results obtained with conformal-to-the-body unstructured grids, and with a similar penalization technique. The considered flows are very different one from another: both steady and unsteady, both subsonic and supersonic examples have been taken into account. All cases are studied with a Cartesian grid.

6.2.1 Unsteady subsonic case: flow past a confined square cylinder

The flow past a confined square cylinder is investigated. The computational domain is shown in Figure (6.1). A configuration is considered with the following parameter values: $L = 1$, $L/H = 1/8$, $L_{in} = 12$, $L_{out} = 20$. On the left side the Poiseuille velocity profile is imposed, with the maximum value U_{max} being 1; the density ρ_{in} is set unitary; the temperature is assumed to be constant, and having the value T_{in} which allows the Mach number to be 0.1 where the horizontal velocity is maximum; the vertical velocity is zero. On the right side, outflow boundary conditions are imposed, that is, velocity horizontal gradients are set to zero, the temperature profile value is taken constant and equal to T_{in} , and the pressure is imposed to have the value which determines a unitary density. On the upper and lower sides wall boundary conditions are considered, that is, no-slip condition for the velocity, and constant temperature always equal to T_{in} .

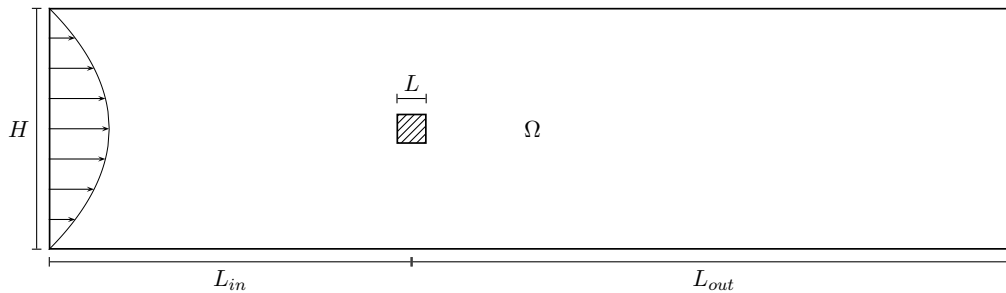


Figure 6.1. Computadional domain: confined square cylinder; low Reynolds number unsteady subsonic flow; Poiseuille velocity profile at the inlet

For the internal boundary conditions, the cylinder is fixed, and the temperature value is set equal to T_{in} ; this assumption for T is allowed by the low Mach number. $Re = 150$

is assumed from the values U_{max} and ρ_{in} at the inlet, and from the length L of the edges of the cylinder; the viscosity is taken constant.

Three different grids are used: two uniform with 640×160 (G_1) and 1280×320 (G_2) cells, respectively; one stretched (G_{1s}) with 640×160 cells. For this latter grid, the stretching is performed along both the horizontal and vertical directions, independently one from the other, taking the cylinder edges as references. The cell distribution along \vec{x} is made by means of the following power law expressions:

$$\left\{ \begin{array}{l} \Delta x_k = \left[(x_{ref1} - x_{min}) / \left(\frac{\alpha_L^{N_L-1} - 1}{\alpha_L - 1} \right) \right] \cdot \alpha_L^{N_L-1-k}, \quad k = 0, \dots, N_L - 1 \\ \Delta x_k = \frac{1}{N_{in}}, \quad k = N_L, \dots, N_L + N_{in} \\ \Delta x_k = \left[(x_{max} - x_{ref2}) / \left(\frac{\alpha_R^{N_R-1} - 1}{\alpha_R - 1} \right) \right] \cdot \alpha_R^{k-N_L-N_{in}}, \quad k = N_L + N_{in} + 1, \dots, N_L + N_{in} + N_R - 1 \end{array} \right.$$

where $N_L = 220$, $N_{in} = 40$, $N_R = 380$ are the numbers of cells at the left, on the side and at the right of the cylinder, respectively; x_{ref1} , x_{ref2} are the abscissa of the left and right, respectively, vertical sides of the cylinder; x_{min} , x_{max} are the abscissa of the inlet/outlet, respectively, of the domain. The parameter α_L is set to 1.006 and α_R to 1.0036. The same law is used for the vertical distribution, setting both α_L and α_R to 1.021. Computations on the grids G_1 and G_{1s} are both made with first and second order schemes, and both with implicit and semi-implicit schemes; the fully implicit scheme results able to use $CFL = 30$ compared to the $CFL = 0.5$ of the latter technique. On the grid G_2 only the semi-implicit scheme is used because of the large amount of required memory to treat the matrix in Equations (6.4) and (6.5).

In the Figures (6.2) and (6.3) the horizontal and vertical velocities, the pressure and the temperature fields obtained on the grid G_2 are shown. The cylinder being substituted by the flow, black dashed lines define its edges. As it can be qualitatively seen, a von Kármán wake develops past the cylinder, and a region with high pressure and temperature is present in front of it, according to what is expected.

We now make a more precise analysis of the results. First of all, we verify that the boundary conditions are satisfied on the cylinder. We look the Figure (6.4), where the

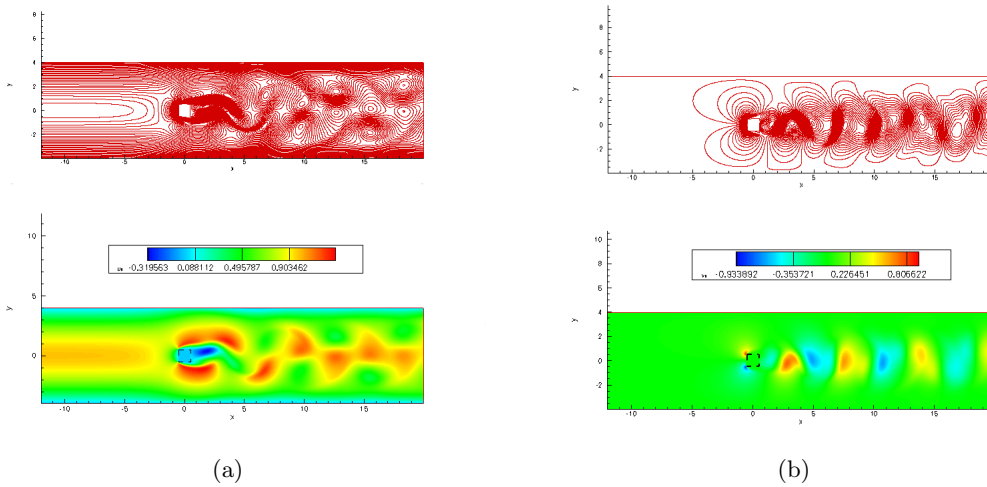


Figure 6.2. Horizontal (a) and vertical (b) velocity flow fields: the coherent structures into the von Kármán wake are visible.

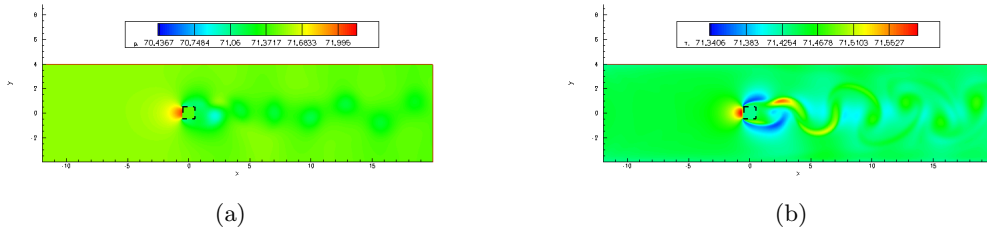


Figure 6.3. Pressure (a) and temperature (b) flow fields.

velocity module and the temperature are plotted along a straight vertical line at $x = 0$, the dashed lines representing the upper and lower horizontal sides of the cylinder. The cinematic and thermal boundary layers are well defined, both the quantities achieving the correct imposed values on the contours.

To analyse the behavior of the wake, a comparison is made between the results of the numerical code here built and those [7] and [18] for the Strouhal-Reynolds relationship: the first ones are obtained by means of a finite volume method (*FVM*) and of a lattice-Boltzmann method (*LBA*), the second ones by means of a finite-difference scheme. In Figure (6.5) three points are plotted which represent the second order code results for all the three grids. The evaluated variable is the vertical velocity and the observation point is ($x = 3, y = 0$); the Strouhal is computed using U_{max} and the length L of the cylinder

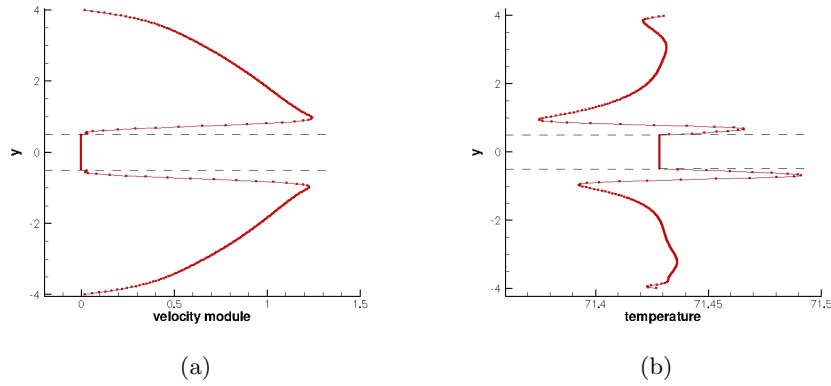


Figure 6.4. Velocity module (a) and temperature (b) profile along the vertical line at $x = 0$.

side. As it can be seen, the results are in agreement with those in the literature.

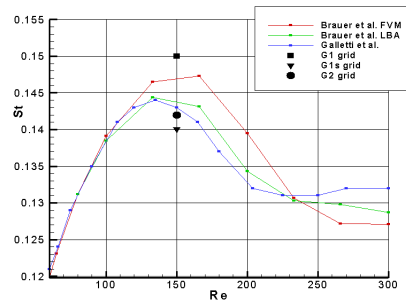


Figure 6.5. Strouhal-Reynolds number for $L/H = 0.125$

The last comparison concerns the amplitude of the oscillations of the vertical velocity in the wake. The results of the present code for the finest grid and those of the *AERO* code (an implicit code, edited by *INRIA*, which solves the Navier-Stokes equations by means of unstructured conformal-to-the-body grids) are compared in (6.6). A convergence on the order of the method is found going from the first to the second one. Moreover, the differences on the amplitudes are acceptable taking into account the different numerical techniques of the codes.

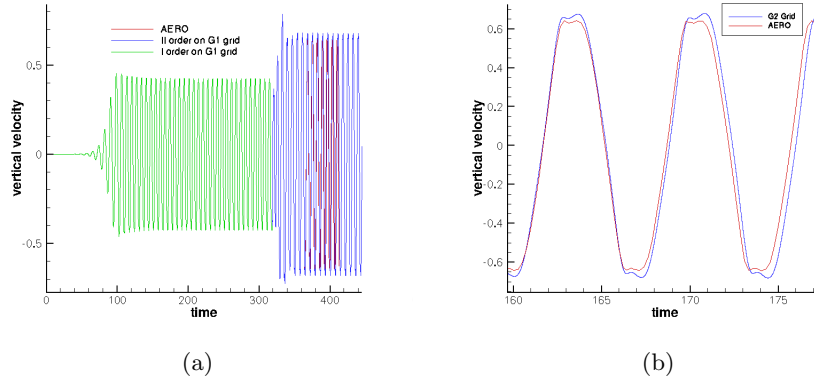


Figure 6.6. Comparison with the results of the code *AERO*: in (a) convergence on the order of the method; in (b) comparison with the oscillation amplitude of the flow field over the G_2 grid.

6.2.2 Steady supersonic case: bow shock

A case where a circular cylinder is moving at a supersonic speed is studied. Following the theory, a bow shock is expected placed at a certain distance behind the cylinder. The results are compared to those of [6]. The Re value is set to 50000, sufficiently large to also enable a comparison with the analytical solution in [5], obtained in the case of inviscid flow.

The domain Ω is $[0,2] \times [-1,3]$, sufficiently large for imposing free-stream conditions on the upper and lower sides. These boundary conditions are also put at the inlet $x = 0$, and are: $M = 2$, $v = 0$, $p = 1$, and $\rho = 1$. At the outlet, non-reflecting boundary conditions are imposed. The penalized region, that is, the cylinder, is centered in $(x = 1, y = 1)$, with radius $r = 0.2$, and on its boundaries the no-slip condition and $T = 3$ are imposed. As usual in this work, the penalization parameter ϕ is set to 10^{-12} .

The computations are made on two different grids, one of 512^2 grid cells (G_1), which both the semi-implicit and the implicit schemes are applied to, and one of 1024^2 cells (G_2), where only the semi-implicit code is performed. As in the previous example, implicit code is not applied to too fine grids because of the large required memory for the stockage and solution of the resulting system. This restriction could be avoided by implementing an appropriate preconditioner, but this is out of the purposes of the present work, as above explained. However it has to be noticed that on the coarser grid G_1 the semi-implicit code

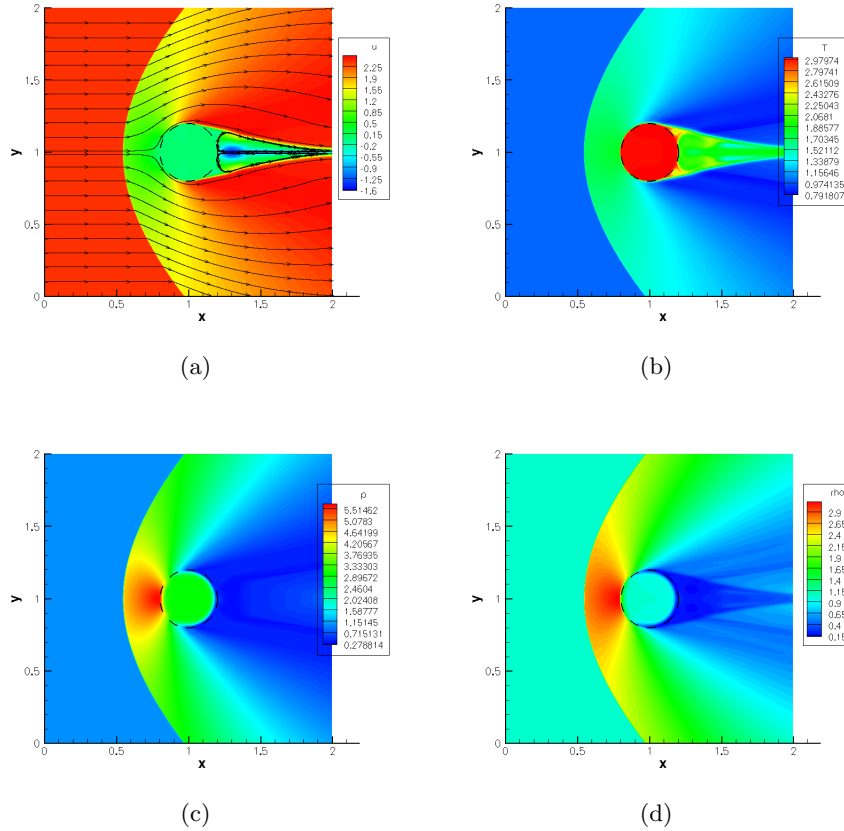


Figure 6.7. Horizontal velocity (a), temperature (b), pressure (c) and density (d) fields around a cylinder moving at $M = 2$.

was run with $CFL = 0.2$, and the fully implicit one with $CFL = 2$, reducing a lot the computational time.

The results for the grid G_2 are shown in Figure (6.7); to better visualize the flow field, the restricted area $[0,2] \times [0,2]$ is considered. The bow shock is defined; inside the cylinder it can be noticed that, while velocity and temperature have exactly the imposed constant values, pressure and density experienced little variations. A not yet verified hypothesis about this behavior is the following: the penalization is made only on velocity and temperature, then pressure and density don't have to respect any kind of restriction. Inside the body there is the typical environment of the acoustic wave propagation; then, when a little perturbation of velocity takes place on the body contours, a pressure wave starts to propagate inside the body, with the consequent perturbation also of the density,

the temperature being constant. However any specific study has not been performed yet, and this remains only a possible explanation.

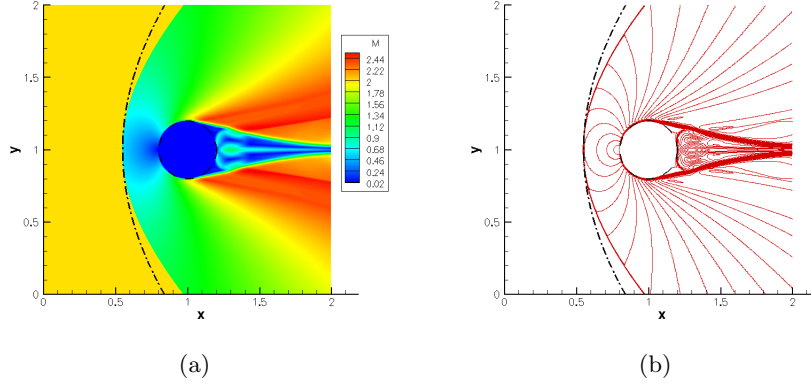


Figure 6.8. Mach number field (a) and isocontours (b) for a cylinder moving at $M = 2$.

We come back to the analysis of the results. In Figure (6.8) the analytic hyperbola of Billig [5] is superimposed to the Mach number field; it is obtained by the following expression:

$$x = R + \Delta - R_C \cot^2 \theta \left[\left(1 + \frac{y^2 \tan^2 \theta}{R_C^2} \right)^{\frac{1}{2}} - 1 \right] \quad (6.6)$$

where:

- R = cylinder radius;
- Δ = standoff distance of the shock from the cylinder; it is obtained experimentally by means of the following equation:

$$\frac{\Delta}{R} = 0.386 \cdot \exp \left(\frac{4.67}{M^2} \right);$$

- R_C = vertex radius of curvature of the hyperbola; also this quantity is evaluated experimentally using the following expression:

$$\frac{R_C}{R} = 1.386 \cdot \exp \left(\frac{1.8}{(M - 1)^{0.75}} \right);$$

- θ = Mach angle relative to the free-stream flow.

As it can be seen, the numerical results are in good agreement with the analytical ones near the stagnation line, where the shock is stronger. Far from this region, there are little differences, which are ascribable to two different causes. The numerical solution is obtained by means of a fully Navier-Stokes solving code, while the Billig solution is relative to an inviscid flow. At the outside, the imposed conditions are not the correct ones: supersonic and subsonic regions would have to be marked in order to give the correct pressure at the subsonic exit; however this is out of the present purposes.

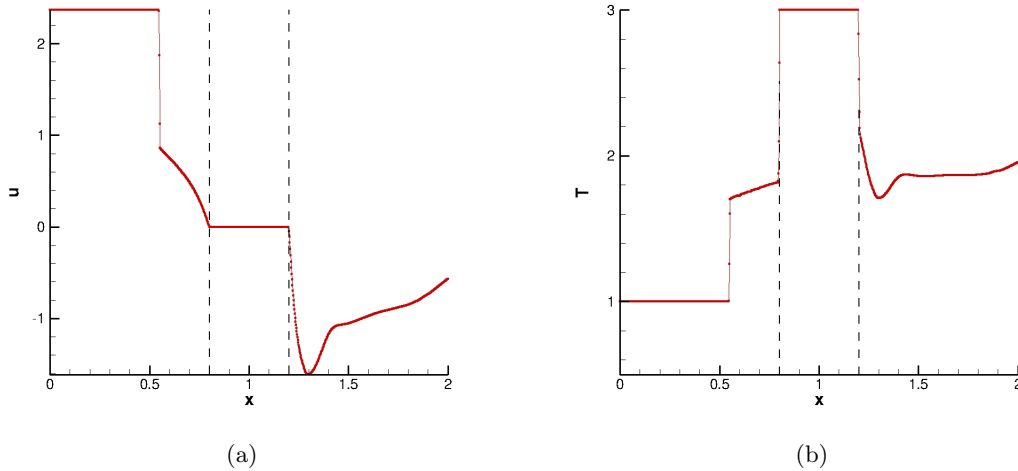


Figure 6.9. Horizontal velocity (a) and temperature (b) distribution along the line at $y = 1$.

We now make some numerical comparisons. Firstly, the respect of the boundary conditions on the cylinder is verified taking the velocity module and the temperature along the line at $y = 1$, as shown in Figure (6.9); as expected, these quantities assume the imposed values of 0 and 3, respectively.

Considering also the Mach number and the pressure behaviors on the same line at $y = 1$ (Figure (6.10)), the position of the shock can be focused on. Making a comparison with the standoff distance of Billig [5] and [6], as shown in Table(6.1), a good agreement is found. The same comparison can be made about the pressure value at the stagnation point; according to the compressible flow theory, there's the following expression to be considered:

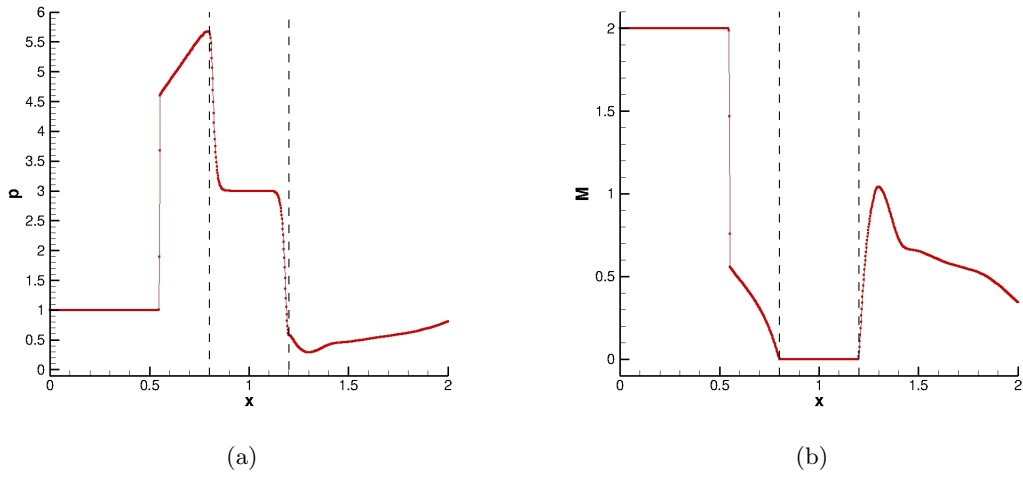


Figure 6.10. Pressure (a) and Mach number (b) distribution along the line at $y = 1$.

$$p_s = p_v \cdot \left(1 + \frac{\gamma - 1}{2} M_v^2 \right)^{\frac{\gamma}{\gamma - 1}}$$

Also in this comparison, the agreement is good.

	Billig	Boiron	Actual
Δ/R	1.24	1.33 / 1.23	1.375 / 1.25
p_s	5.69	5.65 / 5.68	5.67 / 5.7

Table 6.1. Numerical comparison between the present results and those of [5] and [6]

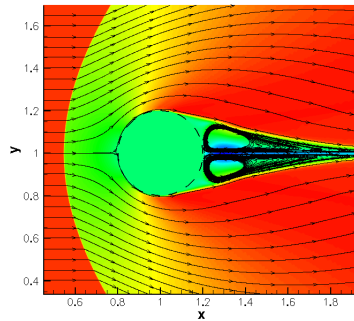


Figure 6.11. Streamlines in the recirculation region past the cylinder.

In figure (6.11) the streamline structure in the recirculation region past the cylinder is represented in order to qualitatively visualize how much the penalization technique allows to obtain good simulations of flows past bluff bodies.

In conclusion it can be said that the proposed method, both in the semi-implicit and implicit form, is also able to well describe the phenomena occurring in steady supersonic flow fields.

6.2.3 Unsteady supersonic flow: transmission and reflection of a shock

The last case is useful to appreciate the power of the implemented technique in describing also complicated unsteady supersonic flow fields like that of a shock which interacts with a cylinder, resulting in a shock which advances besides and in another which is reflected behind. These results are compared with [6] taking into account in particular the position of the two shocks at a certain time, and also visualizing the flow field along lines passing through the body.

The domain $\Omega = [0,2] \times [0,2]$ is used, in which a cylinder of radius $R = 0.2$ is placed at $(x = 0.5, y = 1)$. A vertical shock moving from left to right at $M = 3$ is located in $x = 0.1$; behind it, the following values are set: $\rho_1 = 1$, $p_1 = 1$, $u_1 = 0$ and $v_1 = 0$; the values at the left of the shock are computed according to the theory, so assuming that the reference system is located on the shock and moves with it, and they are then imposed at $x = 0$; on the other three boundaries non-reflecting conditions are imposed.

The results are analyzed at the instant $t = 0.4$. They are obtained on a grid of 512^2 cells with both the semi-implicit and the implicit code. As in the previous case, the implicit code allows using CFLs up to 2, while the semi-implicit one has to run with CFLs up to 0.15, resulting in a very large computational time.

In Figure (6.12) the resulting flow fields for different variables are shown. The detached shock in front of the body, and the shock beside it which separates the wake at the left from the stagnant region at the right are clearly observable. To make a numerical comparison we consider their positions: in the current results, the abscissa of the detached shock on the stagnation line is $x_1 = 0.08$, and that of the other shock on the lower boundary is $x_2 = 1.46$. These values are in perfect agreement with the results shown in [6], where $x_1 \approx 0.1$ and $x_2 \approx 1.45$.

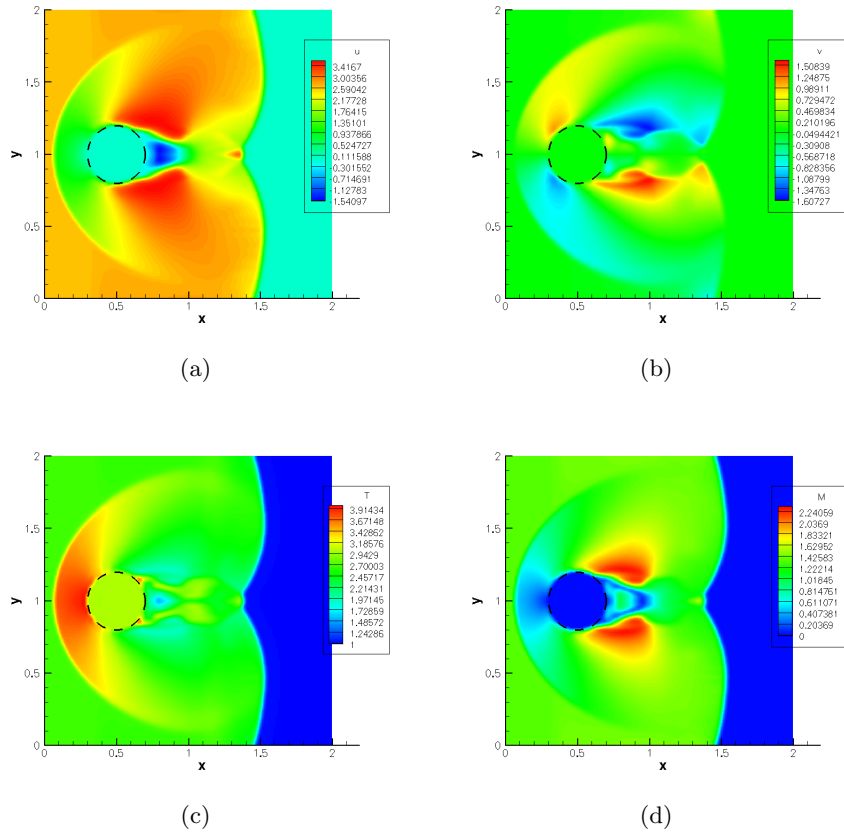


Figure 6.12. Horizontal (a) and vertical (b) velocities, temperature (c) and Mach number (d) fields at $t = 0.4$.

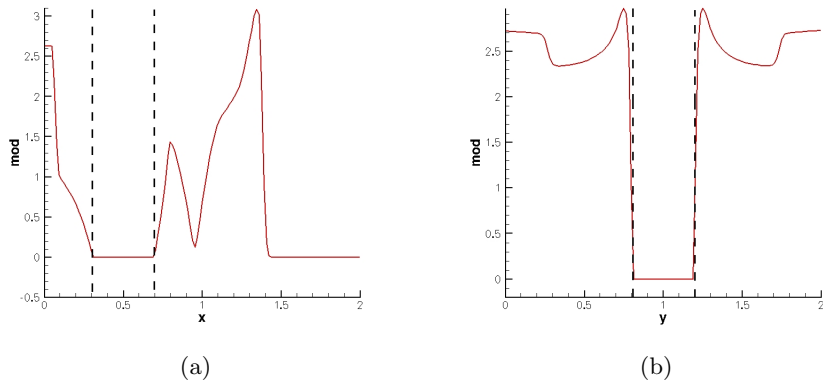


Figure 6.13. Velocity module distribution along the lines $y = 1$ (a) and $x = 0.5$ (b).

In Figure (6.13) the velocity module along the lines $y = 1$ and $x = 0.5$ is plotted; in (6.13)(a) the two shocks are well distinguishable; in (6.13)(b) the symmetry of the flow field with respect to the $y = 1$ line can be seen. In both the cases the boundary conditions are verified.

6.3 Application to moving boundaries

An illustrative example of the application of the penalization technique to the study of flow fields around moving bodies is described. The analysed case is shown in (6.14).

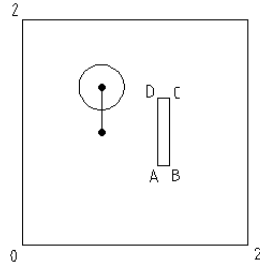


Figure 6.14. Domain geometrical features.

In a square domain $\Omega = [0,2] \times [0,2]$ a rectangular cylinder of sides $AB = 0.1$ and $BC = 0.6$ is placed in a way such that $A \equiv (1.2,0.7)$, and a circular cylinder of radius $R = 0.2$ has the center in $(0.7,1.4)$ at the initial time. On all the four boundaries freestream conditions are considered imposing these values: $u_\infty = 0$, $v_\infty = 0$, $p_\infty = 1$, $\rho_\infty = 1$. The initial conditions into the flow field are set equal to the freestream ones. The flow field is simulated which is produced by an oscillatory vertical movement of the cylinder around the point $(x = 0.7, y = 1.2)$; the law defining the position of the cylinder center $Y_C(t)$ is determined by the following expression:

$$Y_C(t) = Y_0 + A \cdot \sin(\omega \cdot t) \quad (6.7)$$

with Y_0 being the initial position of the center, $A = 0.4$ being the amplitude of the oscillations, and $\omega = 0.78 \text{ Hz}$ being the pulsatory variable of the oscillations. $Re = 1000$ is taken considering ρ_∞ , R and the maximum velocity experienced by the cylinder. A constant viscosity is assumed.

The computation is made on a 512^2 cells grid. In Figure (6.15) the resulting Mach and pressure fields are shown at different times. The dashed lines represent the sides of the rectangular and of the circular cylinders. As it can be seen, the flow field is characterized by complex structures and discontinuities reflection and interaction phenomena which the penalization technique seems to well describe. In particular, zones of compression and expansion can be noted to alternate in front and at the rear of the circular cylinder, depending on the direction of its motion; the rising discontinuities then interact with the rectangular cylinder at rest, and move far away going out of the computational domain.

This would be only an example to demonstrate the power of the penalization technique: in fact, the entire evolution in time of the flow field is computed on the same simple Cartesian grid, which doesn't change in time to become conformal to the new positions of the moving body. The only thing that changes into the code in comparison with the static cases previously described is the determination of the fluid and solid region by means of the Heaviside function: in fact, now it is not constant, but it has to be updated at each time step in order to take into account the motion of the circular cylinder.

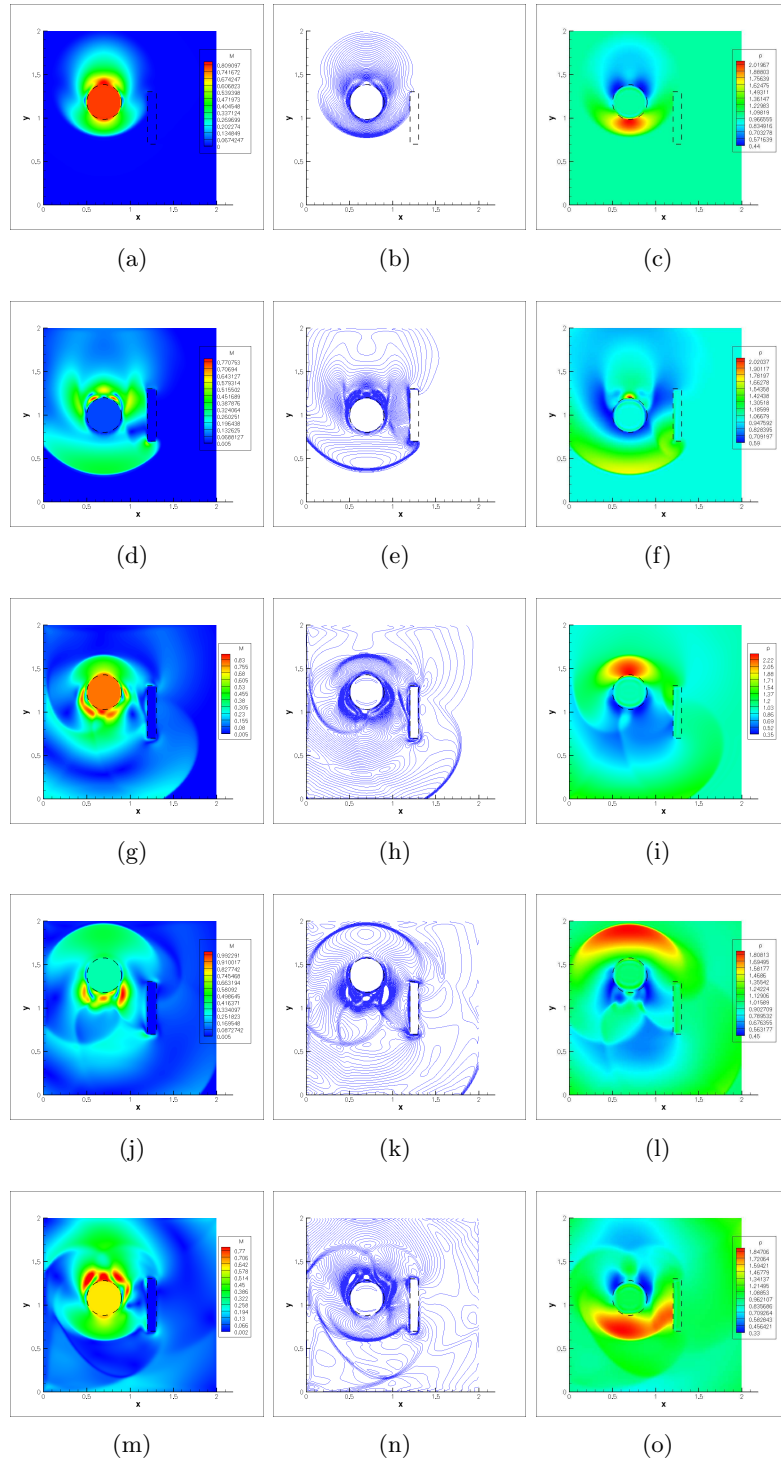


Figure 6.15. Snapshots for Mach (left and central columns) and pressure (right column) fields at different time instants: at $t = 0.352$ (a),(b),(c), at $t = 0.682$ (d),(e),(f), at $t = 1.03$ (g),(h),(i), at $t = 1.239$ (j),(k),(l), at $t = 1.81$ (m),(n),(o).

Chapter 7

Conclusions

The work here presented has treated the problem of flow separation in two different ways.

In the first part a 2D incompressible and inviscid model was built to describe the dynamics of an unsteady flow field. In particular we have focused the attention on the study of a doubly-connected domain like that of a flow field past a 2-blade Darrieus turbine. It is characterized by a deep unsteadiness, which results both from the structures arising into the flow field and from the motion of the blades. A non usual approach is adopted, which derives from the conjugation of two different techniques: an analytical one, based on the use of conformal mapping, which enables the transformation of the physical domain into a computational one, where the solution of the flow is more simple to be found; and a numerical one, based on the use of point vortex singularities to describe the vorticity shed from the blades. In the computational domain the complex velocity and potential were determined by means of two tools: considering the blades at rest, by means of elliptic functions, exploiting the double-periodicity of the transformed plane; while, considering the motion of the blades, by means of the power series in order to impose the impermeability condition. A problem we encountered relative to the determination of the elliptic functions above: by only imposing the two Kutta conditions at the trailing edges, the flow field was not completely defined, the circulations being able to assume any arbitrary initial value. This case has never been taken into account in the literature, where the study of vortex motion in multi-connected domains have been considered only in the case where the initial circulation around the bodies is assumed to be null and constant in

time. But here, due to the unsteadiness, the circulations vary in time. So a third condition had to be found in order to guarantee the respect of the Kelvin theorem, that is, that the shed vorticity be equal to the opposite value of the circulations around the corresponding bodies.

The model having been defined, a solution is proposed in order to reduce the separation phenomena occurring from the blades of a VAWT which reduce its performances and are deleterious for its structure. It consists in designing the blades provided with cavities. This is a technology that is being already studied for aeronautical applications, that enables control of the stall at high angles of incidence. So, in the present case the blades experiencing opposite angles of attack during a working-cycle, the trapping cavities have the aim of reducing the unsteady rise of complex vortex shedding phenomena. Our results show that these cavities are able to maintain the vortical structures trapped in themselves. But an observation has to be made: these results are obtained in the limit of an inviscid flow, that is, the main causes of separation cannot be handled both on the blade contours and in the cavities. However they describe a situation that is not completely different from the reality because of the following reason: the unsteadiness rising into the boundary layer has a relaxation time that is sufficiently long with respect to the time the turbine employs to make a cycle. In other words the unsteadiness phenomena cannot grow enough to generate the separation. So with this assumption the results above can be considered true in a first rough approximation, allowing one to think positively about a future application of this technology: a lot of features have yet to be investigated, starting from the use of a viscous model.

In the second part a penalized fully Navier-Stokes equations solver code is implemented: the aim is to develop a code which is able to describe the aerodynamics past bodies of any shape by means of a simple structured Cartesian mesh. A penalization technique is adopted which has already been used in literature. The fundamental idea is to consider the bodies in the domain as porous media, with a porosity tending to zero in comparison to that of the external flow, which tends to infinity. This results in the penalization of the momentum and energy equations in order to impose the correct boundary conditions on the body contours. A semi-implicit method is built reproducing the model already described in the literature, and then a fully implicit scheme is also implemented, allowing

the use of greater CFL numbers. A validation of the two developed schemes is performed on both supersonic and subsonic cases, verifying their extended applicability from high Mach number flows, such as the study of a detached shock in front of a cylinder moving at a supersonic speed, to low Mach number flows, such as the study of the wake past a confined square cylinder. In the end, a qualitative example is reported where the implemented technique is applied to a domain where the bodies are moving. Here the advantages are even more evident than above: in fact, even if a body is in motion, the grid never changes. In comparison with the case where the bodies are at rest, the code remains the same, except for the definition of the mask function, which has to track the motion of the internal contours. All these considerations allow considering the implemented method promising for future possible applications, also because on simple meshes, like the Cartesian ones used here, very simple numerical schemes could be applied, resulting in very efficient codes, an aspect which hasn't been taken into account here yet.

Bibliography

- [1] P. Angot, C.H. Bruneau, and P. Fabrie. A Penalization Method to take into account Obstacles in Viscous Flows. *Numerische Mathematik*, 81:497–520, 1999.
- [2] E. Arquis and J.P. Caltagirone. Sur les Conditions Hydrodynamiques au Voisinage d’une Interface Milieu-Fluide - Milieu Poreux: Application à la Convection Naturelle. *C.R. Acad. Sci. Paris II*, 299:1–4, 1984.
- [3] P.R. Ashill, J.L. Fulker, and K.C. Hackett. A Review of Recent Developments in Flow Control. *Aeronaut. J.*, 109:205–232, 2005.
- [4] P.W. Bearman. Investigation of Flow behind Two Dimensional Model with Blunt Trailing Edge and Fitted with Splitter Plates. *J. Fluid Mech.*, 21:241–255, 1965.
- [5] F.S. Billig. Shock-Wave Shapes around Spherical- and Cylindrical- Nosed Bodies. *J. Spacecraft*, 4(6).
- [6] O. Boiron, G. Chiavassa, and R. Donat. A High-Resolution Penalization Method for Large mach Number Flows in the Presence of Obstacles. *Computers and Fluids*, doi: 101016/j.compfluid.2008.07.003.
- [7] M. Breuer, J. Bernsdorf, T. Zeiser, and F. Durst. Accurate Computations of the Laminar Flow past a Square Cylinder based on Two Different Methods: Lattice-Boltzmann and Finite Volume. *Int. J. Heat Fluid Flow*, 21:186–196, 2000.
- [8] P.K. Chang. *Control of Flow Separation*. Hemisphere, 1976.
- [9] S.I. Chernyshenko, B. Galletti, A. Iollo, and L. Zannetti. Trapped Vortices and a Favourable Pressure Gradient. *J. Fluid Mech.*, 482:235–255, 2003.
- [10] G. Chiavassa and R. Donat. A Penalization Technique for the Efficient Computation of Compressible Fluid Flow with Obstacles. *Proceedings of the XI Intl. Conf. on Hyperbolic Problems: Theory, Numerics, Applications*.

- [11] R.R. Clements. An Inviscid Model of Two-dimensional Vortex Shedding. *J. Fluid Mech.*, 57:321–336, 1973.
- [12] D.G. Crowdy and J.S. Marshall. The Motion of a Point Vortex around Multiple Circular Islands. *Phys. Fluids*, 17:56602–13, 2005.
- [13] P. Deglaire, O. Agren, H. Bernhoff, and M. Leijon. Conformal Mapping and Efficient Boundary Element Method without Boundary Elements for Fast Vortex Particle Simulations. *European Journal of Mechanics-B, Fluids*, 27:150–176, 2008.
- [14] M. Ferlauto. Studio e Controllo di Strutture Vorticose di Parete. *Ph.D. Thesis: Politecnico di Milano*.
- [15] C. Ferrari. Sulla Trasformazione Conforme di Due Cerchi in Due Profili Alari. *Mem. R. Acc. Sci. Torino*, 68:1–15, 1930.
- [16] M. Gad-el Hak. Modern Developments in Flow Control. *Appl. Mech. Rev.*, 48:365–379, 1996.
- [17] M. Gad-el Hak and D.M. Bushnell. Separation Control: Review. *J. Fluids Eng.*, 113:5–30, 1991.
- [18] B. Galletti, C.H. Bruneau, L. Zannetti, and A. Iollo. Low-Order Modelling of Laminar Flow Regimes past a Confined Square Cylinder. *J. Fluid Mech.*, 503:161–170, 2004.
- [19] F. Gallizio. Analytical and Numerical Vortex Methods to Model Separated Flows. *Ph.D. Thesis, Politecnico di Torino*.
- [20] R. Ghias, R. Mittal, and T.S. Lund. A Non-Body Conformal Grid Method for Simulation of Compressible Flows with Complex Immersed Boudaries. *AIAA Paper*, No. 2004-0080.
- [21] S.K. Godunov. A Difference Scheme for Numerical Computation of Discontinuous Solutions of Equations of Fluid Dynamics. *Math. Sb.*, 47(89):271–306, 1959.
- [22] D. Goldstein, R. Handler, and L. Sirovich. Modeling a No-Slip Flow Boundary with an External Flow Field. *J. Comp. Phys.*, 105:354–366, 1993.
- [23] A.S. Grinspan and U.K. Saha. Experimental Investigation of Twisted Bladed savonius Turbine Rotor. *International Energy Journal*, 5:No. 1, 2004.
- [24] N.D. Halsey. Potential Flow Analysis of Multielement Airfoils using Conformal Mapping. *AIAA Journal*, 17:1281–1288, 1979.
- [25] C. Hirsch. *Numerical Computation of Internal and External Flows*. Wiley Series,

- 2007.
- [26] G. Iaccarino and R. Verzicco. Immersed Boundary Technique for Turbulent Flow Simulations. *Appl. Mech. Rev.*, 56:331–347, 2003.
 - [27] A. Iollo and L. Zannetti. Trapped Vortex Optimal Control by Suction and Blowing at the Wall. *Eur. J. Mech./Fluid*, 20:7–24, 2001.
 - [28] D.C. Ives. A Modern Look at Conformal Mapping, Including Multiply Connected Regions. *AIAA Journal*, 14:1006–1011, 1976.
 - [29] E.R. Johnson and N.R. McDonald. The Motion of a Vortex near Two Circular Cylinders. *Proc. R. Soc. Lond. A*, 460:939–954, 2004.
 - [30] E.R. Johnson and N.R. McDonald. Vortices near Barriers with Multiple Gaps. *J. Fluid Mech.*, 531:335–358, 2005.
 - [31] N.K.R. Kevlahan and O.V. Vasilyev. An Adaptive Wavelet Collocation Method for the Solution of the Partial Differential Equations. *SIAM J. Sci. Comput.*, 26(6):1894–1915, 2005.
 - [32] M. Kiya, M. and Arie. A Contribution to an Inviscid Vortex-Shedding Model for an Inclined Flat Plate in Uniform Flow. *J. Fluid Mech.*, 82:223–243, 1977.
 - [33] A.M. Kuethe and E-CY. Chow. *Foundations of Aerodynamics*. Wiley, 1986.
 - [34] G.V. Lachmann. *Boundary-Layer and Flow Control*. Pergamon, 1961.
 - [35] M. Lagally. Die Reibungslose Stromung im Aussengbiet Zweier Kreise. *Z. Angew. Math. Mech.*, 9:299–305, 1929.
 - [36] A. Leonard. Vortex Methods for Flow Simulation. *J. Comp. Phys.*, 37:289–335, 1980.
 - [37] R.J. LeVeque. *Numerical Methods for Conservation Laws*. Birkhauser, 1992.
 - [38] J. Lighthill. *An Informal Introduction to Theoretical Fluid Mechanics*. Oxford University Press, 1986.
 - [39] C.C. Lin. On the Motion of Vortices in Two Dimensions. *Proc. Nat. Acad. Sci. USA*, 27:570–577, 1941.
 - [40] Q. Liu and O.V. Vasilyev. A Brinkman Penalization Method for the Compressible Flows in Complex Geometries. *J. Comp. Phys.*, 227:946–966, 2007.
 - [41] S. Majumdar, G. Iaccarino, and P.A. Durbin. Rans Solver with Adaptive Structured Boundary Non-Conforming Grids. *Annu. Res. Briefs, Cent. Turbul. Res.*
 - [42] S. Mertens and E. de Vries. Small Wind Turbines: Driving Performance. *Renewable*

- Energy World*, 11:Issue 3, 2008.
- [43] S. Mertens, G. van Kuik, and G. van Bussel. Performance of a H-Darrieus in the Skewed Flow on a Roof. *Journal of solar energy engineering*, 125:433–440, 2003.
- [44] L.M. Milne-Thomson. *Theoretical Hydrodynamics*. Dover, 1968.
- [45] R. Mittal and G. Iaccarino. Immersed Boundary Methods. *Annu. Rev. Fluid Mech.*, 37:239–261, 2005.
- [46] J. Mohd-Yosuf. Combined Immersed Boundary/b-spline Methods for Simulation of Flows in Complex Geometries. *Annu. Res. Briefs, Cent. Turbul. Res.*
- [47] S.J. Osher and S. Chakravarthy. Upwind Schemes and Boundary Conditions with Applications to Euler Equations in General Geometries. *J. Comp. Phys.*, 50:447–481, 1983.
- [48] S.J. Osher and F. Solomon. Upwind Difference Schemes for Hyperbolic Systems of Conservation Laws. *Math. Comp.*, 38:339–374, 1982.
- [49] M. Pandolfi. On the Flux-Difference-Splitting formulation. *Notes on Numerical Fluid Mechanics*, 26.
- [50] C.S. Peskin. Flow Patterns around Heart Valves: a Digital Computer Method for Solving the Equations of Motion. *Ph.D. Thesis, Albert Einstein College of Medicine*.
- [51] C.S. Peskin. The Fluid Dynamics of Heart Valves: Experimental, Theoretical and Computational Methods. *Annu. Rev. Fluid Mech.*, 14:235–259, 1981.
- [52] M.C.A.M. Peters. Aeroacoustics Sources in Internal Flows. *Ph.D. Thesis, Eindhoven University of Technology*.
- [53] B. Pollul. Preconditioners for Linearized Discrete Compressible Euler Equations. *ECCOMAS CFD 2006*.
- [54] L. Prandtl. *Essentials of Fluid Dynamics*. Blackie & Son, 1952.
- [55] D.I. Pullin. The Large-Scale Structure of Unsteady Self-Similar Rolled-Up Vortex-Sheets. *J. Fluid Mech.*, 88:401–430, 1978.
- [56] K. Rajan and P.R. Viswanath. Passive Control of Surface Pressure Fluctuations in Reattaching Flows. *Aeronaut. J.*, 106:669–674, 2002.
- [57] F.O. Ringleb. Separation Control by Trapped Vortices. *Boundary Layer and Flow Control*.
- [58] L. Rosenhead. The Formation of Vortices from a Surface of Discontinuity. *Proc. Roy.*

- Soc. Lond. A*, 134:170, 1931.
- [59] A. Roshko. On the Drag and Shedding Frequency of Two-Dimensional Bluff Bodies. *NACA*, TN:3169, 1954.
- [60] E.J. Routh. Some Application of Conjugate Functions. *Proc. Lond. Math. Soc.*, 12:73–89, 1881.
- [61] Y. Saad and M.H. Schultz. Gmres: a Generalized Minimal Residual Algorithm for Solving Nonsymmetric Linear Systems. *Journal on Scientific and Statistical Computing*, 7:856–869, 1986.
- [62] P.G. Saffman. *Vortex Dynamics*. Cambridge University Press, 1992.
- [63] T. Sarpkaya. An Inviscid Model of Two-Dimensional Vortex Shedding for Transient and Asymptotically Steady Separated Flow over an Inclined Flat Plate. *J. Fluid Mech.*, 68:109–129, 1975.
- [64] T. Sarpkaya. Computational Methods with Vortices. *J. Fluids Eng.*, 111:5–52, 1989.
- [65] P.N. Shankar. Developments of Vertical Axis Wind Turbines. *Proc. Indian Acad. Sci.*, 2, No.1:49–66, 1979.
- [66] A.H. Shapiro. *The Dynamics and Thermodynamics of Compressible Fluid Flow - Volume II*. The Ronald Press Company, 1953.
- [67] C.J. Simão Ferreira, H. Bijl, G. van Bussel, and G. van Kuik. Simulating Dynamic Stall in a 2D VAWT: Modeling Strategy, Verification and Validation with Particle Image Velocimetry Data. *Journal of Physics: Conference Series*, 75 012023, doi: 10.1088/1742-6596/75/1/012023.
- [68] E. Stanewski. Adaptive Wing and Flow Control Technology. *Prog. Aerosp. Sci.*, 37:583–667, 2001.
- [69] T. Theodorsen and I.E. Garrick. General Potential Theory of Arbitrary Wing Sections. *NACA TR*, No. 452, 1933.
- [70] F. Tricomi. *Funzioni Ellittiche*. Zanichelli, 1951.
- [71] F. Tricomi. *Funzioni Analitiche*. Zanichelli, 1961.
- [72] Y.H. Tseng and J.H. Ferziger. A Ghost-Cell Immersed Boundary Method for Flow in Complex Geometry. *J. Comp. Phys.*, 192:593–623, 2003.
- [73] V. Venkatakrishnan. Convergence to the Steady State Solutions of the Euler Equations on Unstructured Grids with Limiters. *J. Comp. Phys.*, 118(1):120–130, 1995.

- [74] P.R. Viswanath, G. Ramesh, and K.T. Madhavan. Separation Control by Tangential Blowing inside the Bubble. *Exp. Fluids*, 29:96–102, 2000.
- [75] VortexCell2050. <http://www.vortexcell2050.org/>.
- [76] T. Ye, R. Mittal, H.S. Udaykumar, and W. Shyy. An Accurate Cartesian Grid Method for Viscous Incompressible Flows with Complex Immersed Boundaries. *J. Comp. Phys.*, 156:209–240, 1999.
- [77] L. Zannetti. Vortex Equilibrium in Flows past Bluff Bodies. *J. Fluid Mech.*, 562:151–171, 2006.
- [78] L. Zannetti and S.I. Chernyshenko. Vortex Pair and Chaplygin Cusps. *Eur. J. Mech./Fluid*, 24:328–337, 2005.
- [79] L. Zannetti, F. Gallizio, and G. Ottino. Vortex Capturing Vertical Axis Wind Turbine. *Journal of Physics: Conference Series*, 75:doi:10.1088/1742-6596/75/1/012029, 2007.
- [80] L. Zannetti, F. Gallizio, and G.M. Ottino. Vortex Motion in Doubly Connected Domain. *J. Fluid Mech.*, 612:143–152, 2008.
- [81] L. Zannetti and A. Iollo. Passive Control of the Vortex Wake Past a Flat Plate at Incidence. *Theor. Comp. Fluid Dyn.*, 16:211–230, 2003.